EXPLORING AND EXPLOITING RESONANCE IN COUPLED AND/OR NONLINEAR MICROELECTROMECHANICAL OSCILLATORS

By

Jeffrey F. Rhoads

A DISSERTATION

Submitted to
Michigan State University
in partial fulfillment of the requirements
for the degree of

DOCTOR OF PHILOSOPHY

Department of Mechanical Engineering

2007

ABSTRACT

EXPLORING AND EXPLOITING RESONANCE IN COUPLED AND/OR NONLINEAR MICROELECTROMECHANICAL OSCILLATORS

By

Jeffrey F. Rhoads

Mass sensors utilizing resonant microelectromechanical systems (MEMS) have recently garnered significant interest from the engineering research community. While motivations vary, this interest is generally attributed to the fact that resonant microsensors offer the potential for increased mass sensitivity, in addition to all of the benefits typically attendant to microelectromechanical devices, namely, minimal power consumption, small size, seamless integration with existing integrated circuit technologies, and comparatively low cost. Pertinent to the present study is the fact that the majority of resonant microsensors utilize linear resonance structures. While this approach offers unquestionable utility, because most uncoupled, linear microsensors feature a single dominant degree-of-freedom and a single functionalized surface, these devices are generally capable of detecting only a single analyte. Likewise, since Lorentzian resonance structures are employed, sensor metrics are often constrained by the devices' scale and difficult to control independently.

The present study seeks to overcome the aforementioned limitations by examining the use of non-traditional microresonator architectures in resonant mass sensing applications. Specifically, the work considers the design, modeling, analysis, and implementation of (i) single input - single output (SISO), multi-analyte sensors based on arrays of coupled microbeam oscillators, (ii) electrostatically-actuated microbeams utilizing purely-parametric excitations, and (iii) resonant microcantilevers utilizing magnetomotive transduction. Each of these systems is believed to be capable of

rendering simpler mass sensing systems and/or sensors with improved metrics.

The first portion of the present study considers the design and development of a SISO, resonant mass sensor capable of detecting multiple target analytes. This device, much like its traditional counterparts, employs linear resonance shifts to indicate a detection event. Here, however, a coupled resonator architecture is used, in conjunction with mode localization, to yield a comparatively-simpler, multi-analyte sensor. While the present work details the sensor's development from conception to testing, particular emphasis is place on system modeling, analysis, and design.

The second portion of the work examines the use of electrostatically-actuated microbeam systems with purely-parametric excitations. These devices, which utilize symmetric electrostatic actuation, are of direct interest here, because they, unlike their traditional variable-gap counterparts, feature a number of desirable frequency response characteristics, including nearly-ideal stopband rejection, in addition to high noise robustness and high mass sensitivity. In this investigation, particular emphasis is placed on system modeling, nonlinear analysis, and device design.

The final portion of this dissertation focuses on resonant microcantilevers that utilize electromagnetic actuation and sensing, or so-called magnetomotive transduction. These devices have recently garnered increasing interest due to their scalability and 'self-sensing' capabilities, both of which are highly desirable in resonant mass sensing applications. The first part of this investigation details the modeling, analysis, and predictive design of a representative nonlinear device. This effort is intended to serve as a precursor to the development of self-sensing, nonlinear resonant mass sensors. The latter portion of the investigation examines (analytically and experimentally) the implementation of parametric amplification in a linear, electromagnetically-actuated microbeam system. This low-noise resonance amplification technique should facilitate the development of self-sensing, linear mass sensors.

To my parents and countless others
who in their own way
supported this endeavor.

ACKNOWLEDGMENTS

Though this work formally acknowledges only a single author, it is truly the product of a six-year, group effort. In light of this, I would like to take the present opportunity to acknowledge the many individuals who have helped shape this work and, perhaps more importantly, have made an indelible impression on my personal and professional life in the process.

First and foremost, my regards go to my mentor and advisor, Steve Shaw. This work would not have been possible without your patience, guidance, and support. You are a first-rate researcher and a true professional.

I also extend my gratitude to Kim Turner, Barry DeMartini, Kari Lukes, and the other members of the Mechanics of Microscale Systems Laboratory at the University of California, Santa Barbara for their willingness to commit time and effort to our unconventional research ventures.

I would also like to thank my graduate committee, Alan Haddow, Ranjan Mukherjee, and Dean Aslam, as well as past and present colleagues, Brian Olson, Umar Farooq, and Nick Miller. Collectively, you represent my research 'sounding board'. I am indebted to each of you for your technical insight. Particular thanks also go to Brian Feeny and Craig Somerton for their continual support of my professional goals.

Finally, my gratitude goes to my parents and extended family. You are the rock I stand on.

TABLE OF CONTENTS

LIST OF TABLES

LIST OF FIGURES

CHAPTER 1

Introduction

Since the advent of the first electromechanical resonant gate transistor in mid-1965, interest in resonant microelectromechanical systems (MEMS) has steadily increased [1–3]. Though the devices still have not fully met early industrial expectations, research advances over the past twenty years have allowed resonant microsystems to emerge as viable alternatives to conventional electrical and mechanical resonators, such as those based on integrated RLC circuits or vibrating quartz crystals, and, ultimately, to become integral components in a number of emergent technologies, including high-frequency signal filters [4–8], highly-sensitive chemical and biological sensors [9–32], tactical-grade inertial sensors [33–39], and atomic force microscopes (AFMs) [40–43]. While this wide applicability has undoubtedly generated some technical interest, the principal appeal of microresonators stems from the numerous advantages inherent to MEMS, namely, in comparison to their macroscale counterparts they consume minimal power, occupy minimal space, are highly integrable with existing integrated circuit (IC) technologies, and, when bulk fabricated, can be realized at comparatively low cost. Furthermore, these systems can be designed to feature inherent nonlinearities and be widely tunable, both of which are highly desirable in the context of the present study.

To date, the vast majority of research related to microresonators has focused on isolated, single-degree-of-freedom (SDOF) oscillators that utilize a linear frequency

response structure. While these oscillators (described in greater detail in Section 1.1) are well suited for applications such as radio-frequency (RF) signal filtering and mass detection, they offer comparatively little flexibility (in both design and operation) and are generally well understood by the MEMS research community. Accordingly, the present work focuses on less traditional resonator implementations, namely those based on coupled oscillators, oscillators with nonlinear frequency response structures, and/or oscillators that are parametrically excited. These systems, with careful design, are believed to be capable of yielding performance metrics superior to their more traditional counterparts, and could potentially supplant their directly-excited, linear brethren in the near future. It is important to note that while the systems described herein are believed to be novel, the present investigation of coupled and/or nonlinear microelectromechanical (MEM) devices is by no means singular in nature. Accordingly, Sections 1.2-1.4 briefly outline prior research in each of the aforementioned areas (nonlinear microresonators, coupled microresonators, etc.). Following this review, Section 1.5 presents information specific to resonant mass sensing, the proposed application for the systems detailed herein. The chapter concludes in Section 1.6 with a brief preview of the work's subsequent chapters.

1.1 Linear Microresonators

Though, as noted above, investigations of microelectromechanical resonators began as early as the mid-1960s, research in the area remained largely stagnant until the late-1980s when electrostatically-actuated resonant microbridges and comb-driven microresonators [44–48], as well as dynamic-mode AFMs [40], first emerged. These systems triggered a bevy of research on resonant microsystems with linear and nonlinear frequency response structures, respectively, that continues to this day.

Early investigations of linear microresonators primarily focused on electrostatically actuated and sensed devices, specifically those utilizing interdigitated comb

drives or parallel-plate capacitive structures [38, 44–49]. As microfabrication technologies matured, however, a multitude of linear devices based on alternative transduction mechanisms emerged, including systems utilizing piezoelectric [4, 50, 51], piezoresistive [38, 39, 52], electromagnetic [6, 53, 54], thermal [55–57], and optical [58, 59] actuation and/or sensing elements. Concurrent with this technological maturation was a growth in application. Most notably, systems originally proposed for RF signal filtering and resonant mass sensing applications were adapted for use in inertial sensing, pressure sensing, radiation sensing, magnetic field sensing, cooling (microfans), resonant pumping (diaphragm pumps), and optical scanning systems (see References [38, 39, 49, 60–63] for a general overview of these systems).

The majority of modern microresonators, much like their earlier counterparts, utilize harmonically-forced, linear resonators, which exhibit a Lorentzian frequency response structure (see, for example, Figure 1.1). These devices are highly valued by the MEMS community because they can be realized at small scales (resonators with feature sizes on the order of a few nanometers have been produced – see, for example, References [53, 64–66]) using comparatively simple geometries (typically prismatic beams or thin plates) and have a frequency response structure which is dependent on only three distinct parameters: the resonator's natural frequency (ω_n), quality factor (Q), and normalized excitation amplitude. Though this simplistic approach possesses unquestionable utility (the design, fabrication, and integration of linear microresonators is projected to become a multi-billion dollar industry by the end of the decade), the lack of flexibility attendant to these systems (due to the small number of free design parameters and rigid Lorentzian frequency response structure) constrains their ultimate potential.

1.2 Nonlinear Microresonators

Nonlinearities in resonant microsystems generally arise from three distinct sources: large structural deformations, displacement-dependent excitations, and tip/sample interaction potentials, such as the Lennard-Jones potential, which arise in atomic force microscopy [43]. As tip/sample interactions have received an abundance of attention in both the physics and engineering communities, other sources of nonlinearity are emphasized here.

Despite the fact that many MEMS devices feature inherent nonlinearities, nonlinear frequency response structures traditionally have been avoided within the MEMS research community. In fact, nonlinear microresonators have received meaningful attention only within the past five to ten years. Early on, investigations of nonlinear microresonators emphasized forced harmonic oscillators, typically planar comb-driven devices, with nonlinearities arising from large elastic deformations. These devices exhibited classical Duffing frequency response structures, which offered a number of attendant benefits (e.g., lower sensitivity to damping), but were deemed to be inferior to their Lorentzian counterparts for most applications [67]. Nonlinear, electrostatically-actuated, variable-gap structures drew slightly more attention from the MEMS community, due to their highly tunable nature [68–73]; but, only recently, with the release of a multitude of studies focusing on the nonlinear response of microsystems undergoing large elastic deformations in the presence of multi-physics excitations, have nonlinear microresonators garnered serious attention (see, for example, References [74–77]). While motivations vary, this increase in attention is generally attributed to the broad conclusion that while microresonators based on nonlinear frequency response structures are more difficult to design and analyze than their linear counterparts, they offer a degree of tunability unattainable with a linear device and have the potential to exhibit superior performance metrics. Furthermore, an appreciable understanding of nonlinearity is essential to the future development of functional nanoresonators, as

these devices operate in the presence of an elevated noise floor and lowered nonlinear 'ceiling' (i.e. they have a severely limited linear dynamic range) [70, 78].

1.3 Coupled Microresonators

Coupled microresonators have received significant attention in the MEMS community since the early-1990s, but primarily within the context of RF signal filtering. Nguyen, for example, showed as early as the mid-1990s that microelectromechanical (MEM) analogs of RLC ladder filters could be constructed using finite-length chains of microresonators mechanically coupled in a nearest-neighbor configuration [5, 8, 79–82]. These systems were found to exhibit high-frequency, multi-resonance passbands with effective quality factors orders-of-magnitude larger than those of their purely-electrical or mechanical predecessors. Subsequent studies have expanded upon Nguyen's work by incorporating alternative coupling architectures, such as cyclic chains [83], as well as alternative coupling mechanisms, including gap-dependent electrostatic coupling [84–87].

In 2003, the effects of frequency mistuning and nonlinearity in coupled resonator systems were systematically analyzed for the first time at the microscale. These studies revealed that mistuning and/or nonlinear coupling could lead to the spatial localization of energy (mechanical manifestations of Anderson localization) or so-called localized modes [88–96]. Though these early investigations largely ignored practical application, in late 2005, Speltzer, *et al.* demonstrated that spatially localized modes can be advantageous in resonant mass sensing [97, 98]. The first portion of the present work, namely Chapter 2, focuses on a related investigation, which was completed concurrent with this study.

Before proceeding, it is prudent to note that other collective behaviors have recently been identified and/or investigated in coupled microelectromechanical systems. For example, Cross, *et al.* showed in 2004 that coupled, nonlinear microelectrome-

chanical oscillators, under certain conditions, can synchronize [99, 100]. This collective behavior, as the authors note, offers one potential method of overcoming process-induced variations in coupled oscillator systems. In other work, Hoppensteadt and Izhikevich noted that certain collective behaviors predicted to occur in coupled microresonator systems have the potential to serve as memory elements in next-generation computing systems [101]. Though neither of these research directions are directly considered herein, both should be considered plausible extensions of the present work.

1.4 Parametrically-Excited Microresonators and Parametric Amplification

Though they could be categorized with their time-invariant counterparts detailed above, parametrically-excited microresonators, or microresonators with periodic, time-varying coefficients, are reviewed independently here due to their prominence in the latter portions of the present work. Parametric resonance in MEMS was first reported by Turner, *et al.* in the late 1990s [102]. Since this initial investigation, parametric resonance has been identified and, ultimately, exploited in a wide variety of microelectromechanical (MEM) resonators, including electrostatically-actuated torsional, planar shuttle mass, and microbeam resonators [87, 103–118], optically-excited disk resonators [119, 120], and piezoelectrically-excited microbeams [121]. Likewise, such devices have been proposed for use in a wide variety of applications, including resonant mass sensing, RF signal filtering/frequency-selective switching, scanning probe microscopy, resonant microscanning, and inertial sensing (microgyroscopes).

Generally speaking, parametric resonance in MEMS is coveted due to the nearly-ideal stopband rejection (non-resonant, noise floor response) attendant to a parametrically-excited oscillator's frequency response (see Figure 1.2 for a represen-

tative nonlinear response). However, recent work has indicated that parametrically-excited systems are also less sensitive to damping and more robust to additive noise than their time-invariant counterparts [108, 111, 122], feature an extremely sharp response roll-off [106], and offer a degree of tunability that is unmatched in MEMS [106, 107, 116]. As each of these benefits, as well as the fundamentals of parametrically-excited systems, in general, are discussed at great length in prior work by the author, additional details are omitted here. Those seeking additional background are referred to References [107, 123–125].

While parametric excitation, in and of itself, is of interest in the present work, a related phenomenon of equal interest is mechanical-domain parametric amplification, or the process of amplifying mechanical vibration (namely, a given system's resonance) with a time-varying pump. While this nearly-noise-free amplification approach has been utilized for nearly a century in electrical and optical systems [126–128], the technique wasn't introduced into the mechanical domain until 1991, when Rugar and Grütter showed that significant resonance amplification could be realized in a piezoelectrically-base-excited cantilever by adding an electrostatic pump at twice the beam's natural frequency [129]. Though the study initially received little attention, the explosion of MEMS research in the 1990s resulted in a number of subsequent investigations, which showed that gains of more than 20 dB can be realized, via parametric amplification, in a wide variety of microelectromechanical systems, including torsional microresonators [103, 130], electric force microscopes [131], optically-excited micromechanical oscillators [132], micro ring gyroscopes [133], MEMS diaphragms [134], coupled microresonators [135], and microcantilevers [136–139]. Similar work has recently demonstrated that parametric amplification can be realized in macroscale mechanical systems, as well [140, 141]. As detailed below, Chapter 6 demonstrates the use of parametric amplification in an emerging class of microresonators, which utilize magnetomotive transduction principles.

1.5 Resonant Mass Sensing

While the microresonator systems described herein can be utilized in a wide range of applications, the emphasis in the present work is on resonant mass sensing. Though perspectives vary, the first application of microresonators in this context is generally credited to either Thundat, *et al.*, who in the early-1990s inadvertently discovered that the natural frequency of a microcantilever changes with varying humidity [17, 142, 143], or Howe and Muller, who reported an integrated microbridge vapor sensor in 1986. Since these initial reports, resonant microsensors have received an appreciable amount of attention in the chemistry, physics, and engineering communities and have been proposed for use in a wide variety of chemical and biological sensing applications, including those relating to public health and safety (e.g., in chemical detectors capable of monitoring the environment for compounds such as mercury), medical research and diagnostics (e.g., in detectors capable of identifying the presence of a certain protein or strand of DNA), and national security and defense (e.g., in sensors capable of detecting the presence of chemical and biological agents or explosive compounds) [11–15, 18, 20–27, 29–32, 144–152]. While resonant microsensors offer all of the inherent advantages of MEMS, they also offer the potential for higher mass sensitivity (a quantification of the smallest change in mass that can be measured with a given sensor) [11, 17, 20]. Of particular note is recent work by Yang, *et al*, which reported the detection of zeptogram-scale mass particles with nanoscale beam resonators [152]. This performance dwarfs that of most, if not all, conventional competitors.

Pertinent to the present work is the fact that the vast majority of modern resonant microsensors operate on a resonance tracking principle (the term is used loosely here to describe the subsequently-explained phenomenon). That is, the resonant frequency of the sensor, typically comprised of an isolated, single-degree-of-freedom (SDOF) oscillator, is determined prior to implementation, and then during the course of operation the location of this resonance is tracked (see Figure 1.1). As shifts in

the resonant frequency are attributable to mass or stiffness changes in the oscillator, caused by absorption, desorption, local stress stiffening, or a similar chemomechanical process, these shifts can, in turn, be used to identify the presence of a target analyte [11, 153, 154]. Unfortunately, since existing microsensors typically feature a single dominant degree-of-freedom and a very limited number of analytes can be uniquely detected with a single functionalized surface, sensors utilizing this approach are generally capable of detecting only a lone analyte or a class of closely related analytes. Arrays of uncoupled linear oscillators, each individually functionalized for the detection of a specific analyte, have been implemented to overcome this limitation, but the greater hardware and signal processing requirements associated with such sensors lead to added expense and complexity [11]. As detailed below, Chapter 2 of this work introduces a new single input - single output, coupled-array architecture, which facilitates multi-analyte detection, while avoiding most, if not all, of the aforementioned limitations.

While the majority of research related to resonant mass sensors has focused on linear resonator implementations, recent work has indicated that mass sensors based on nonlinear frequency response structures may be capable of exhibiting higher sensitivities [111, 155–157]. These nonlinear devices operate much like their linear counterparts in that they utilize resonance shifts induced by a chemomechanical process (itself initiated by the presence of a target analyte). Here, however, the system's bifurcation structure is actively exploited (see schematic in Figure 1.2). Specifically, a given device is first driven slightly below an identified subcritical bifurcation point. When a small amount of mass interacts with the resonator, the system transitions across the subcritical instability, moving from a stable no-motion state to an unstable no-motion state (in the case of a nonlinear parametrically-excited resonator). This transition results in a larger response amplitude (a by-product of a jump bifurcation), which can be directly correlated to an analyte detection event. While this approach

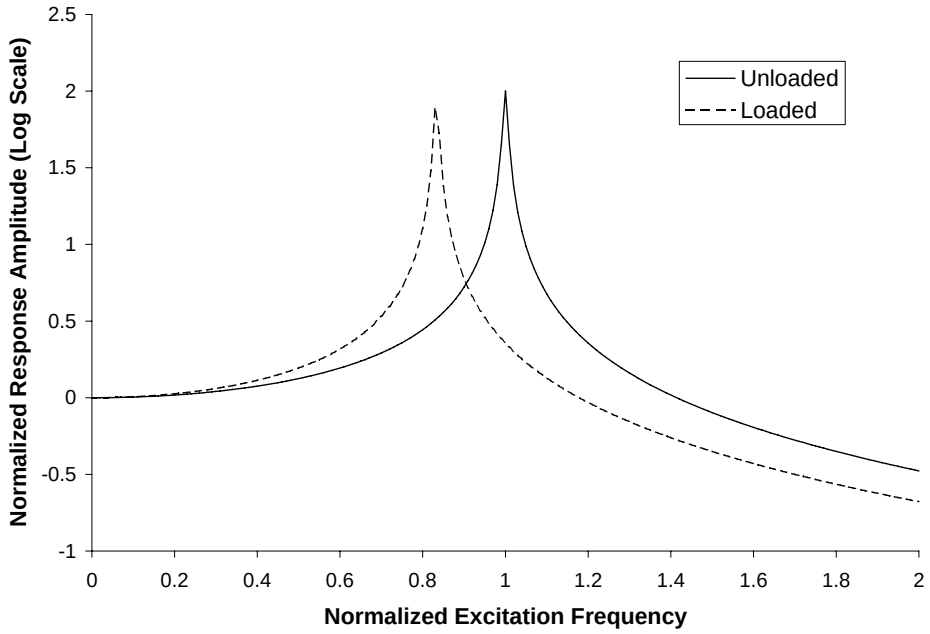

(a)

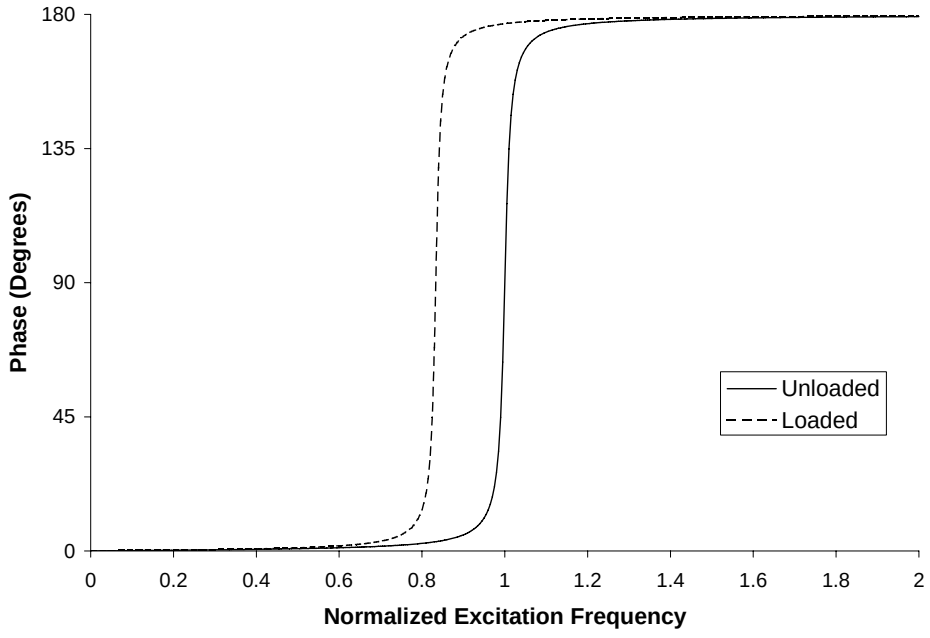

(b)

Figure 1.1. Frequency response plots, (a) amplitude and (b) phase, for a linear resonant mass sensor. Note that the induced resonance shift (approximately 20%) has been exaggerated for illustrative purposes.

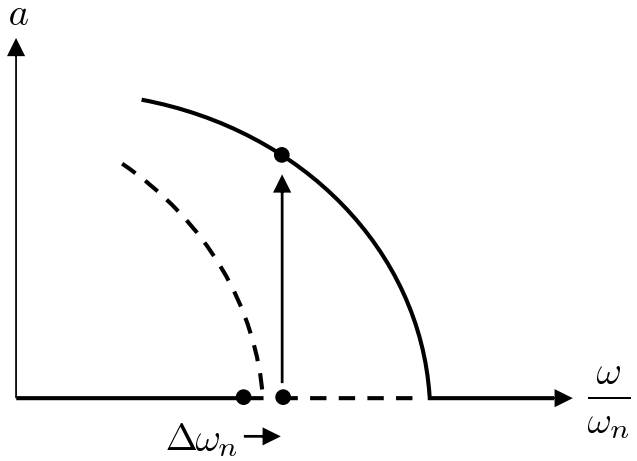

Figure 1.2. A representative frequency response plot (resonator amplitude versus normalized excitation frequency) for a nonlinear mass sensor based on parametric resonance (solid lines indicate a stable steady-state response, dashed lines an unstable response). Note that a small shift in the system's natural frequency drives the system across the subcritical pitchfork bifurcation causing a dramatic increase in the device's response amplitude. This increase can be directly correlated to an analyte detection event.

still utilizes resonance shifts in the course of sensing, because the detection event is directly correlated to a jump in response amplitude, in addition to a frequency shift, the need for attendant frequency tracking/identification hardware, such as phase locked loops, can be (at least partially) negated. As such, the approach potentially allows for smaller, reduced power, chemical and biological detectors with higher sensitivities. As detailed below, Chapters 3 and 5 of the current work examine the behavior of two distinct classes of microresonators that are believed to have promise as nonlinear resonant mass sensors.

1.6 Dissertation Overview

As detailed above, the present work focuses on non-traditional microresonator implementations, specifically those based on nonlinear, coupled, and/or parametrically-excited oscillators, which are believed to have practical utility in resonant mass sensing applications. Given the breadth of this research topic, particular emphasis is placed on three distinct systems: (i) novel, single input - single output, multi-analyte

sensors based on arrays of linear oscillators coupled in 'master-slave' configurations, (ii) electrostatically-actuated microbeams utilizing purely-parametric excitations, and (iii) resonant microcantilevers utilizing magnetomotive transduction. Completed research related to each of these respective systems is briefly previewed below.

1.6.1 A Single Input - Single Output, Multi-Analyte Sensor

As stated in Section 1.5, the majority of chemical and biological sensors based on resonant microstructures utilize isolated microresonators (capable of detecting a single analyte) or dynamically-uncoupled resonator arrays. While the latter systems facilitate the detection of multiple analytes with a single sensor, they are typically multiple input - multiple output (MIMO) devices, and, thus, poorly suited for system integration and, ultimately, analyte assessment. Chapter 2 of the present work introduces a new class of single input - single output (SISO) resonant mass sensor that is capable of simultaneously detecting multiple analytes. These sensors utilize a coupled-resonator architecture, namely a 'master-slave' resonator configuration, in conjunction with mode localization and resonance tracking (detailed above) to facilitate detection.

Chapter 2 of the present work outlines the results of a joint analytical and experimental investigation of the aforementioned sensor. Following a brief introduction, the work details the development of a simple, linear system model that is capable of capturing the behavior of a representative device, and then proceeds with the analysis of a desirable form of the system's frequency response. The chapter then takes an experimental turn with the examination of a series of experimental results obtained from a first-generation sensor design. Pertinent system metrics, as well as relevant design and integration issues, are subsequently discussed, and the chapter concludes with an outline of ongoing research.

1.6.2 Electrostatically-Actuated Microbeam Resonators with Purely-Parametric Excitations

Though, as detailed above, the majority of electrostatically-actuated resonant microbeam systems reported to date have been based on linear resonance structures, a number of recent studies have indicated that the performance metrics associated with such devices can be dramatically improved by exploiting inherent system nonlinearities [68, 71, 104, 118, 158–160]. While a number of distinct mechanisms in these systems can lead to nonlinearity, some of the most interesting nonlinear effects are those generated by variable-gap electrostatic forces, which, due to their position-dependent nature, generally lead to some combination of direct and/or nonlinear parametric excitation [104, 160]. In a typical microbeam design these excitations arise simultaneously, which renders a predictable response, but eliminates (or reduces) the inherent benefits associated with purely-parametric excitations. In particular, known benefits, such as nearly-ideal stopband attenuation, comparatively higher sensitivity, and high noise robustness, are believed to be deteriorated (see, for example, References [106, 161]). Chapter 3 investigates a modified microbeam resonator design that is intended to recover the aforementioned benefits through the implementation of a novel electrode configuration. In particular, the chapter shows that through the use of symmetric electrostatic actuation (as realized through the exploitation of a three plate capacitor design) direct excitation (and certain parametric excitation) effects which hinder device performance can be eliminated or at least reduced to largely insignificant levels. This results in nonlinear microbeam systems that are well suited for mass sensing.

Chapter 3 of the present work details the modeling and analysis of a representative nonlinear microbeam system with symmetric electrostatic actuation. The chapter begins with the development of a distributed-parameter system model that is capable of adequately capturing the microsystem's dynamics. This model is reduced to a

comparatively-simpler, lumped-mass model using modal projection, and subsequently analyzed using standard perturbation techniques. The chapter proceeds with a discussion of various design and implementation issues, and concludes with a brief look at resonant mass sensing.

1.6.3 Electromagnetically-Actuated Microbeam Resonators

While the first two chapters of the present work focus on electrostatically-actuated microsystems, Chapters 4-6 focus on microresonators that utilize electromagnetic actuation and sensing, or so-called magnetomotive transduction. Though these microscale devices were reported in literature as early as 1994 [162, 163], electromagnetically-actuated and sensed devices have garnered increasing interest in recent years, due to their scalability (magnetomotive transduction is easily realized at the nanoscale) and 'self-sensing' capabilities. Collectively, these traits have spurred the rapid implementation of electromagnetically-actuated and sensed resonators in a number of engineering applications [6, 53, 54, 164–170].

The present work focuses on electromagnetically-actuated (EMA) microresonators that are implementable as linear or nonlinear resonant mass sensors, in isolated or coupled-array device configurations. Specifically, the work emphasizes resonators similar to those previously introduced in References [157, 171] and shown in Figure 1.3, which consist of a silicon microcantilever actuated electromagnetically using a Lorenz force (which is generated by the interaction between an external, chip-scale permanent magnet and an integrated current loop) and sensed using an induced electromotive force (emf) (which results from the movement of the integrated current loop through the magnetic field). Particular architectures of interest include isolated, EMA microcantilevers undergoing large deflections (Chapter 5) and isolated, parametrically-amplified, EMA microcantilevers (Chapter 6).

Chapter 4, the first chapter in the work concerned solely with electromagnetically-

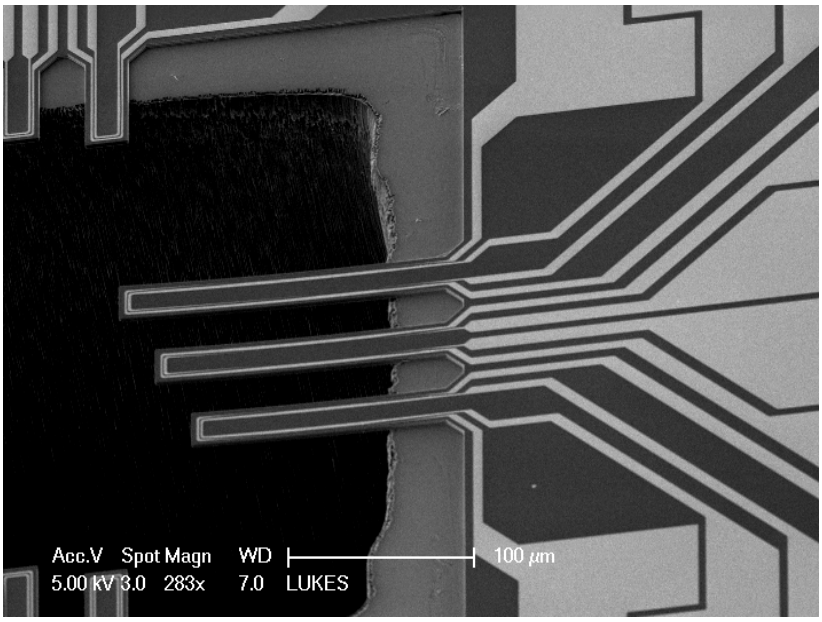

(a)

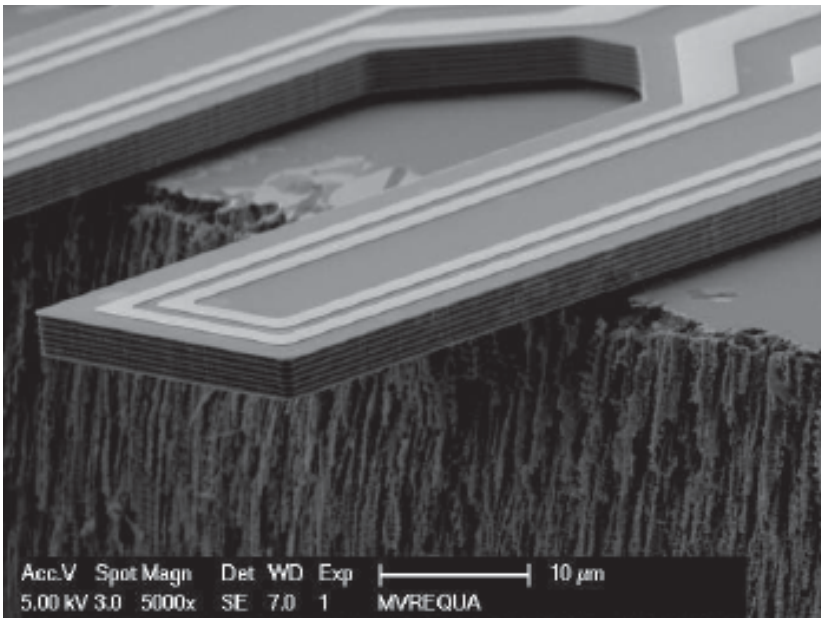

(b)

Figure 1.3. Representative electromagnetically-actuated microcantilevers. Note that the microbeams incorporate two independent current loops – one for sensing and another for actuation (Note that Figure 1.3b is from Reference [171]).

actuated microbeams, focuses on system modeling. A spatiotemporal nonlinear system model capable of accounting for large elastic deformations in the presence of multi-directional Lorentz force excitations is derived, reduced to a comparatively-simpler lumped-mass model through modal projection, and, ultimately, scaled and nondimensionalized for analytical purposes. Using the results of Chapter 4, the work continues in Chapter 5 with an examination of a representative microbeam system's nonlinear behavior. Given that previously-obtained experimental data indicated the need for a higher-order nonlinear model than that previously described by the author in References [106, 107, 124], a fifth-order nonlinear model is used as the basis of study. This model is systematically analyzed using the method of averaging, and various frequency response structures, which are pertinent to the stated application, are examined. Chapter 6 deviates from nonlinear analysis with an investigation of parametric amplification. Though this amplification technique, as detailed above, was previously implemented in a number of resonant microsystems, it proves to be of particular use in electromagnetically-actuated systems, due to the inherent limitations on drive current that exist in such systems, due to material breakdown and device burnout thresholds.

CHAPTER 2

A Single Input - Single Output, Multi-Analyte Sensor

As noted in the introduction, this chapter of the work details a novel chemical and/or biological sensor design that allows for the detection of multiple analytes using a single sensor input and a single sensor output. Unlike their more conventional, isolated counterparts, these devices utilize a coupled-system architecture in which a number of frequency-mistuned microbeam resonators, each individually functionalized for the detection of a specific analyte, are attached to a common shuttle mass (see Figure 2.1), which, in turn, is used for both actuation and sensing (measurement readout) purposes. Providing sufficient vibration localization in the set of mistuned oscillators, this innovative architecture allows for frequency shifts in any, or all, of the individual microbeams to be measured using solely the response of the common shuttle mass. Accordingly, a single, single input - single output (SISO) device proves sufficient for the detection of multiple target analytes.

This chapter specifically details an analytical and experimental investigation of the SISO microsensor design described above (Note that the investigation was previously reported in References [172–174]). The chapter begins with a brief overview of the device's topology, and then proceeds with the derivation of a representative lumped-mass system model and an analysis of a desirable form of the sensor's fre-

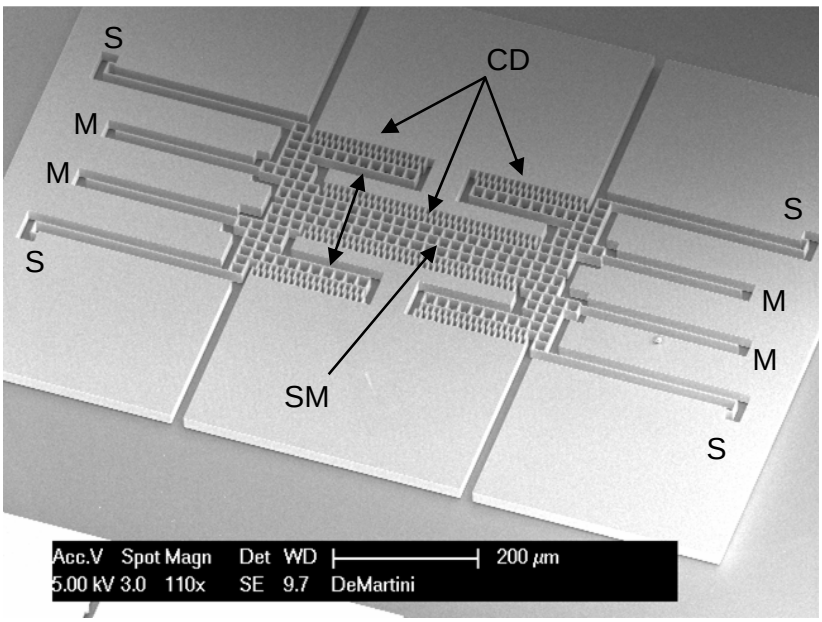

Figure 2.1. A scanning electron micrograph of a translational, SISO, multi-analyte sensor. Key device features have been labeled for reference purposes as follows: the device's shuttle mass is labeled SM; the four individual microbeam oscillators are each labeled M; the electrostatic comb drives are labeled CD; and each of the four folded beam flexures are denoted with an S. Also note that the principal direction of motion is designated by the included double-pointed arrow (From Reference [172]).

quency response. Experimental results, including those acquired from a simulated mass detection event, are subsequently detailed, and the chapter concludes with a brief examination of sensor metrics, a discussion of pertinent design and integration issues, and a brief overview of ongoing and future work.

2.1 System Modeling

Though a variety of geometries can be developed based on the sensor topology described herein, the translational design depicted in Figure 2.1 was selected for examination here due to its relative simplicity. As shown, this design consists of a single shuttle mass (SM), which is suspended above the substrate by four folded beam flexures in such a way that in-plane, unidirectional motion is dominant. Actuation is provided electrostatically through one bank of interdigitated comb drives (CD), the

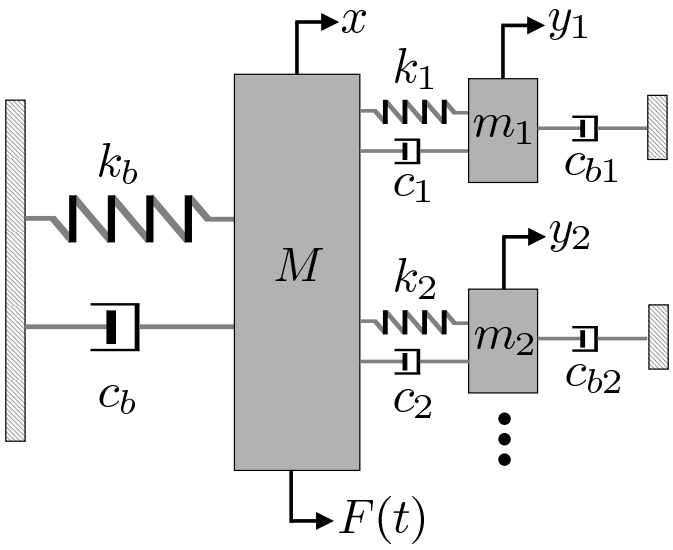

Figure 2.2. A mass-spring-dashpot analog of the sensor topology depicted in Figure 2.1 (From References [172–174]). Note that the larger mass M represents the sensor's shuttle mass and the comparatively smaller masses m_1, m_2, etc. represent the microbeam oscillators.

second bank, though not presently utilized, can be used for sensing (measurement readout). In final implementations, active sensing surfaces will be individually deposited on each of the four microbeam oscillators (M) (this number could easily be expanded to facilitate the detection of a larger number of analytes), which are attached to the common shuttle mass. It should be noted that each of these microbeams deviate slightly in length to ensure ample separation of the coupled system's resonant frequencies, which is necessary to ensure sufficient localization.

Given the geometric complexity of the sensor design depicted in Figure 2.1, it proves convenient for analysis to model the device using a simple lumped-mass analog, such as that shown in Figure 2.2. Here the shuttle mass is represented by the larger mass denoted M and the microbeams are represented by the comparatively smaller masses designated m_1, m_2, etc., elasticity is captured by the linear spring elements designated k_b (for the primary system) and k_1, k_2, etc. (for the microbeams), and intrinsic and extrinsic dissipation (arising primarily from aerodynamic effects, but also including material dissipation) are captured by the linear dashpot elements designated

c_b (for the primary system) and c_1, c_{b1}, c_2, c_{b2}, etc. (for the microbeams). The net electrostatic force, which is applied solely to the shuttle mass, is denoted by the forcing term $F(t)$. Though this topology is believed to be novel in the sensors community, it is important to note that topologies akin to that presented here have been studied in unrelated contexts, namely, broad-band noise control and vibration suppression [175–177].

Using the lumped-mass model depicted in Figure 2.2, it can be shown that the equations of motion governing the system depicted in Figure 2.1 are given by

$$M\ddot{x} + \sum_i m_i \left(\ddot{x} + \ddot{z}_i\right) + \sum_i c_{bi} \left(\dot{x} + \dot{z}_i\right) + c_b\dot{x} + k_b x = F(t), \tag{2.1}$$

$$m_i \left(\ddot{x} + \ddot{z}_i\right) + c_{bi} \left(\dot{x} + \dot{z}_i\right) + c_i\dot{z}_i + k_i z_i = 0, \qquad i = 1, \ldots, N \tag{2.2}$$

where z_i is the relative displacement of the ith subsystem, given by

$$z_i = y_i - x, \qquad i = 1, \ldots, N, \tag{2.3}$$

N specifies the number of microbeam subsystems (active sensing elements) attached to the shuttle mass, and x and y_i represent the absolute displacements of the shuttle mass and ith subsystem, respectively. Providing ample device thickness (approximately 10 μm or larger) and minimal fringe field effects, the applied electrostatic force $F(t)$, which appears in Equation (2.1), can be approximated by

$$F(t) = \frac{\varepsilon_0 n h V^2(t)}{g}, \tag{2.4}$$

where ε_0 represents the free space permittivity, n the total number of comb fingers in the electrostatic comb banks, g the gap between adjacent comb fingers, and h the device thickness. Given a harmonic voltage excitation with amplitude V_A and frequency ω, the resulting net force features both AC and DC components and takes the form

$$F(t) = \frac{\varepsilon_0 n h V_A^2}{2g} \left(1 + \cos 2\omega t\right) = F_0 \left(1 + \cos 2\omega t\right). \tag{2.5}$$

The explicit appearance of the DC excitation can be resolved by redefining the dynamic variables x and z_i by translation according to

$$\hat{x} = x - \bar{x} = x - \frac{F_0}{k_b}, \qquad \hat{z_i} = z_i. \tag{2.6}$$

Nondimensionalizing the resulting displacements by a characteristic length of the system x_0 (e.g., the maximum allowable shuttle mass displacement, as limited by the interdigitated comb drives – note that the selection of the characteristic length is largely arbitrary due to the linear nature of the system) according to

$$u = \frac{\hat{x}}{x_0}, \qquad v_i = \frac{\hat{z_i}}{x_0} \tag{2.7}$$

and the system's excitation and natural frequencies by a characteristic frequency of the system ω_0 (chosen here to be the uncoupled natural frequency of the longest microbeam) yields dimensionless governing equations given by

$$\begin{aligned} u''&+2\zeta_b\Lambda u' + \Lambda^2 u \\ &= \Gamma\cos\Omega\tau - \sum_i \hat{m}_i\left(u'' + v_i''\right) - \sum_i 2\zeta_{bi}\Upsilon_i\hat{m}_i\left(u' + v_i'\right) \end{aligned} \tag{2.8}$$

$$\hat{m}_i\left(u'' + v_i''\right) + 2\hat{m}_i\zeta_i\Upsilon_i v_i' + \hat{m}_i\Upsilon_i^2 v_i = -2\hat{m}_i\zeta_{bi}\Upsilon_i\left(u' + v_i'\right) \qquad i = 1, \ldots, N \tag{2.9}$$

with system parameters defined as in Table 2.1. This system of $N+1$ equations can be compiled into a standard matrix form given by

$$MX'' + CX' + KX = \Phi(\tau) \tag{2.10}$$

for further analysis. Note that here X represents a compiled state vector incorporating the displacements of both the shuttle mass and the microbeam oscillators, M an effective mass matrix incorporating inertial coupling terms, C an effective damping matrix incorporating dissipative coupling terms, K an effective stiffness matrix, and $\Phi(\tau)$ an effective forcing vector, which is sparse except for the first element.

Table 2.1. Nondimensional parameter definitions.

Parameter	Description
$\tau = \omega_0 t$	Nondimensional Time
$\Omega = \dfrac{2\omega}{\omega_0}$	Nondimensional Excitation Frequency
$(\bullet)' = \dfrac{d(\bullet)}{d\tau}$	New Derivative Operator
$u = \dfrac{\hat{x}}{x_0},\ v_i = \dfrac{\hat{z}_i}{x_0}$	Nondimensional Displacements
$\hat{m_i} = \dfrac{m_i}{M}$	Inertia Ratio: ith Microbeam to Shuttle Mass
$\Lambda = \dfrac{\omega_b}{\omega_0} = \dfrac{1}{\omega_0}\sqrt{\dfrac{k_b}{M}}$	Frequency Ratio: Isolated Shuttle Mass to Characteristic Value
$\Upsilon_i = \dfrac{\omega_i}{\omega_0} = \dfrac{1}{\omega_0}\sqrt{\dfrac{k_i}{m_i}}$	Frequency Ratio: ith Isolated Microbeam to Characteristic Value
$\zeta_b = \dfrac{c_b}{2\sqrt{k_b M}}$	Damping Ratio: Isolated Shuttle Mass
$\zeta_i = \dfrac{c_i}{2\sqrt{k_i m_i}}$	Damping Ratio: ith Microbeam (Isolated from Ground)
$\zeta_{bi} = \dfrac{c_{bi}}{2\sqrt{k_i m_i}}$	Pseudo-Damping Ratio: ith Microbeam (Partially Isolated from Shuttle)
$\Gamma = \dfrac{F_0}{M x_0 \omega_0^2}$	Nondimensional Excitation Amplitude

2.2 Frequency Response Characteristics

Using the matrix equation developed in the preceding section, Equation (2.10), the response of the sensor can be easily recovered using any one of the many techniques common to linear systems theory (the impedance approach detailed in Reference [178] was used in the preparation of this work). However, due to the large number of free parameters present in this equation $(4N + 4)$, a number of qualitatively distinct responses, most of which are poorly suited for sensing, are readily obtainable. Accordingly, the present work emphasizes *one* particular form of the system's frequency response that is amenable to sensing. A qualitative representation of this response is shown in Figure 2.3. Though a limited number of alternative responses will facilitate sensing, they are presently believed to be inferior to that detailed here. Accordingly, investigation of these alternatives is left for subsequent works.

Examination of the analytical frequency response plot shown in Figure 2.3 reveals several features of note. First, the response includes a dominant low-frequency resonance (1) which occurs (approximately) at the resonant frequency

$$\Omega_0 \approx \frac{1}{\omega_0}\sqrt{\frac{k_b}{M + \sum_i^N m_i}}. \tag{2.11}$$

As modal analysis confirms, this resonance corresponds to a bulk, in-plane mode of the system where both the shuttle mass and the attached microbeam oscillators move essentially together as a lumped mass. Figure 2.4a, recovered from a finite element analysis of the device verifies this modal behavior. The response also displays four additional, higher-frequency resonances, which are labeled (A), (B), (C), and (D). These resonances each occur at a frequency slightly greater than Υ_i, the rescaled, isolated, microbeam natural frequencies, and correspond to in-plane localized modes where appreciable displacements occur in only a single microbeam. This is confirmed not only by the comparatively-larger resonant amplitudes shown in Figure 2.3a, but also by the finite element results shown in Figure 2.4b. It is important to note that

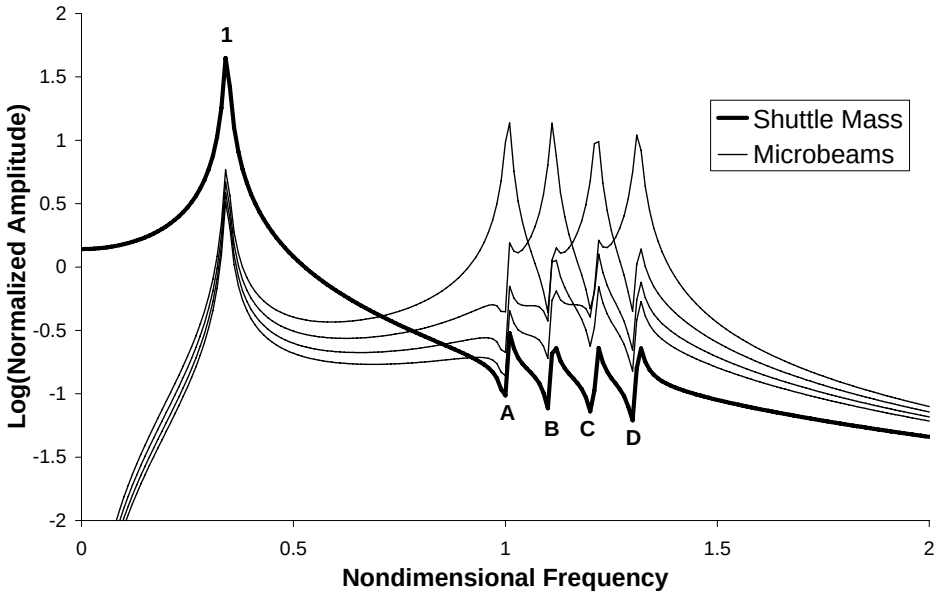

(a)

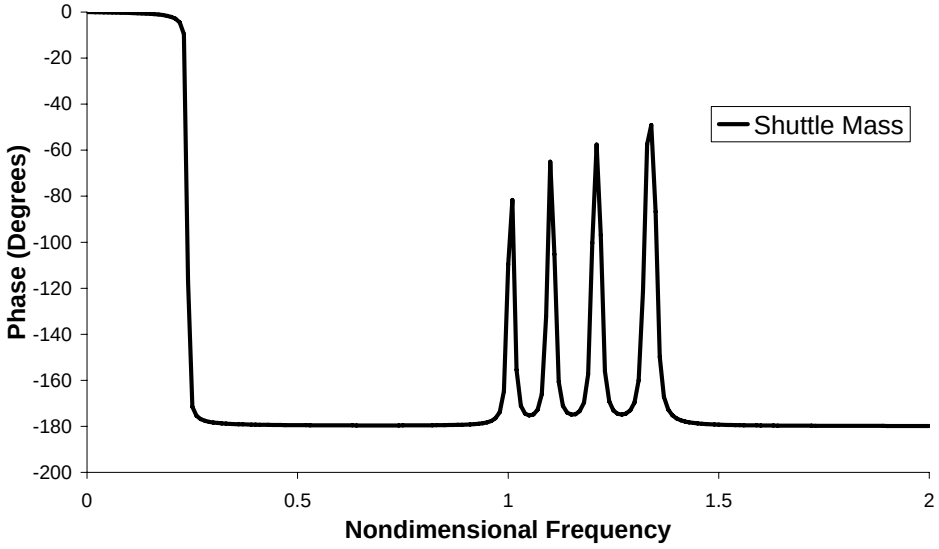

(b)

Figure 2.3. A desirable form of the frequency response, (a) amplitude and (b) phase, for a representative sensor design (From Reference [172]). Note that the labeled resonances correspond to the following modes: (1) A translational in-plane mode, (A, B, C, and D) modes where energy is localized in one of the sensor's microbeams. Also note that for clarity only the phase of the shuttle mass response is shown.

since these higher frequency microbeam resonances (corresponding to modes where energy is largely confined in a single microbeam) induce a measurable resonance in the shuttle mass' response, resonance shifts induced by chemomechanical processes on any, or all, of the microbeams are detectable using only the shuttle mass' response. Accordingly, sweeping the excitation frequency of the system Ω through a frequency range that includes Υ_1, ..., Υ_N allows for the detection of up to N distinct analytes, providing that each microbeam oscillator is properly functionalized.

In order to achieve the desired features in the shuttle mass' frequency response (depicted in Figure 2.3), the system's parameters must be systematically chosen. To this end, details on the selection of inertia ratios ($\hat{m}_i$) and frequency ratios (Υ_i/Λ), as well as the amplitude of the AC voltage excitation applied to the electrostatic comb drives (V_A), which is incorporated into the nondimensional parameter Γ, are detailed here.

Careful selection of the system's frequency ratios (Υ_i/Λ) is required to ensure ample separation between all of the microsensor's resonances, including those associated with out-of-plane modes, which are not captured by the lumped-mass model used in this work. To this end, the following guidelines must be observed throughout the course of design: (i) To avoid interactions between the system's low frequency resonance [labeled (1)] and the resonances associated with the localized modes [labeled (A)-(D)], the system's frequency ratios (Υ_i/Λ) must be specified to be greater than, and well separated from, unity. Failing to meet this criterion results in a contamination of the resonance peaks associated with the localized modes in the proximity of resonance (1), which can negate the successful detection of analytes using the corresponding microbeams, especially in the presence of additive noise. (ii) To avoid the potential formation of a multi-resonance passband, each Υ_i/Λ value must be distinct and well separated from all other frequency ratios. Failing to meet this criterion can result in a number of indistinct resonances, which hinders the detection of individual

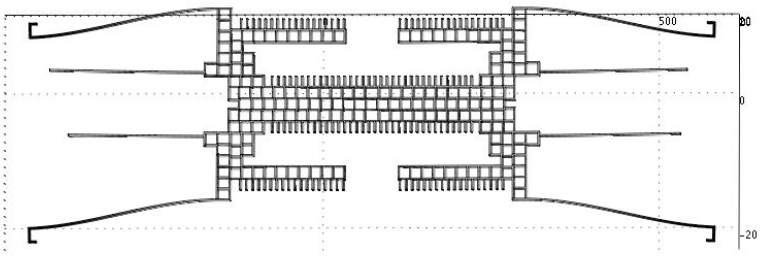

(a)

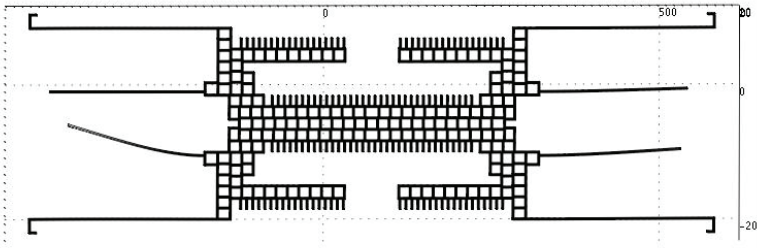

(b)

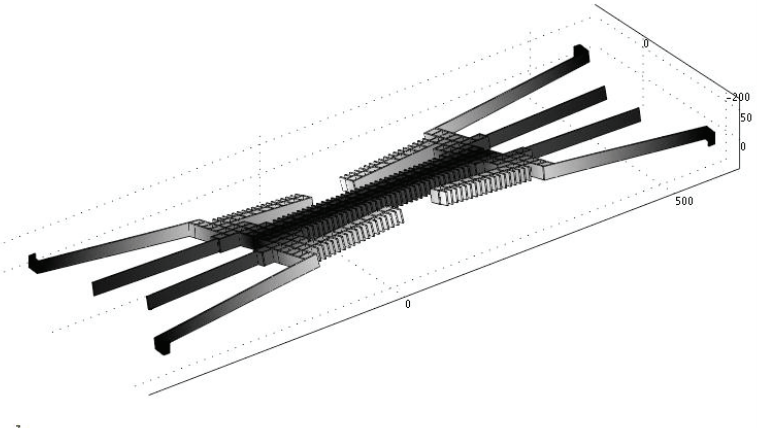

(c)

Figure 2.4. Mode shapes of the sensor as recovered using computer-based finite element methods (From Reference [172]). (a) The first mode of the sensor: a bulk in-plane mode where the shuttle mass and microbeam oscillators move nearly in unison, essentially as a lumped mass. (b) The seventh mode of the sensor: an in-plane, localized mode where movement, and thus energy, is largely confined in a single microbeam. (c) The third mode of the sensor: an out-of-plane torsional mode. Note that the resonant frequencies corresponding to each of these modes are detailed in Table 2.3.

resonance shifts, and ultimately negates multi-analyte detection. (iii) Each uncoupled microbeam frequency (Υ_i), must be well separated from the resonant frequencies associated with both out-of-plane modes and higher frequency, in-plane modes to avoid situations akin to those detailed above in case (i), where the resonances associated with the localized microbeam modes become contaminated by other system resonances. Note that since the lumped-mass model presented here captures only the first five in-plane modes of the system, finite element results similar to those shown in Figure 2.4 are requisite for design. Before proceeding, it should also be noted that the amount of damping present in the system greatly impacts each of the design criterion detailed above. Specifically, in low damping environments the system's resonance peaks can be placed in much closer proximity than they can be in low-Q (comparatively higher damping) environments. Accordingly, the amount of damping present in the system, not only constrains frequency ratio selection, but also limits the number of functionalized microbeams that can be integrated with the system and thus the number of distinct analytes that can be uniquely detected.

Selection of the system's inertia ratios ($\hat{m}_i$) is primarily used to control the relative coupling strength between the microbeam oscillators and the sensor's shuttle mass. Accordingly, these ratios, in conjunction with the system's frequency ratios, are used to control the extent of localization in the coupled system's response [179]. For the sensing principles discussed here, strong mode localization is necessary to ensure efficient mass sensing. This is attributable to the fact that while mass and/or stiffness changes in a single microbeam lead to shifts in all of the coupled system's resonances, in the presence of strong mode localization these mass and/or stiffness changes induce a markedly larger shift in the resonance associated with the altered oscillator. This, in turn, allows for the rapid identification of a given resonance shift's source (namely, the particular microbeam, which having undergone a chemomechanical process, has had its mass and/or stiffness altered) and may ultimately facilitate automated analyte

identification.

Given the linear nature of the sensor design detailed here, manipulation of the AC excitation voltage amplitude (V_A) is used primarily to control the relative magnitude of the shuttle mass' response. As it is desirable to operate in ambient pressure (low-Q) environments, harmonic signals with large excitation amplitude are generally desirable. Caution must be taken, however, to ensure that these amplitudes do not lead to nonlinear resonance structures or device burn-outs.

2.3 Experimental Results: First-Generation Sensors

For proof of concept, a translational device of the type outlined in Section 2.1 was designed, fabricated, and tested experimentally. A scanning electron micrograph of the resulting device is shown in Figure 2.1. The device was fabricated on a silicon-on-insulator (SOI) wafer with a ≈20 μm device layer. The process flow included a lithographic step for pattern definition, a deep silicon etch using a deep reactive ion etcher (DRIE), an O_2 reactive ion etch (RIE) for polymer removal, and finally a hydrofluoric acid wet etch to remove the silicon dioxide beneath the oscillator [180].

For this experiment one set of the interdigitated comb drives was used for electrostatic actuation and the response of the shuttle mass was measured using a single beam laser vibrometer (Polytec) [181]. Since the vibrations of interest occurred in-plane (perpendicular to the laser beam), a 45° mirror was cut into the silicon next to the shuttle mass using a focused ion beam. The output from the vibrometer, which is directly proportional to velocity, was sent to a vector signal analyzer (Hewlett Packard 89410A) to obtain the frequency response of the shuttle mass. By actuating the device with a 6.2 V AC signal in 275 mTorr vacuum and sweeping frequency, the response of the shuttle mass shown in Figure 2.5 was obtained. The experimental response contains the desired spectral features shown in Figure 2.3 [namely the resonances designated (1), (A), (B), (C), and (D)], as well as some that were not predicted

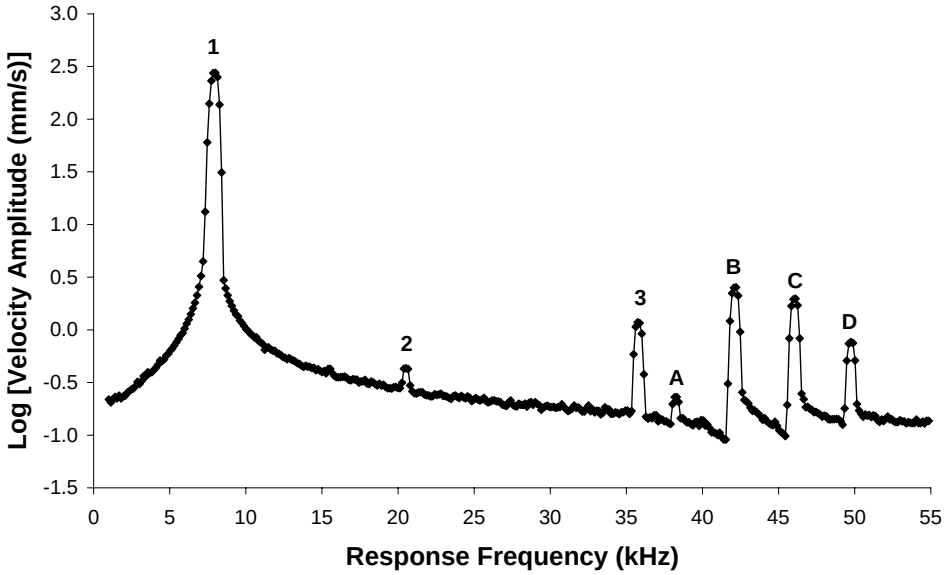

Figure 2.5. Experimentally-obtained frequency response for the sensor depicted in Figure 2.1 actuated with a 6.2 V AC signal in 275 mTorr pressure (From References [172–174]). Note that the labeled resonances correspond to the following modes: (1) Bulk in-plane mode, (2, 3) out-of-plane modes, (A, B, C, and D) modes where energy is localized in the sensor's microbeams. The resonant frequencies associated with each of these modes are tabulated in Table 2.2.

.

Table 2.2. A comparison between the system's experimental and theoretical (FEA) resonant frequencies. Note that the discrepancy shown below is believed to be caused by uncertainties in the device's material properties and thickness.

Mode	Experimental Value (Hz)	FEA Value (Hz)	Percent Error
Bulk Translational Mode	8002	8478	5.9%
First Out-of-Plane Mode	20660	22893	10.8%
Second Out-of-Plane Mode	35877	40335	12.4%
First Localized Mode	38301	41435	8.2%
Second Localized Mode	42206	45608	8.1%
Third Localized Mode	46112	49594	7.6%
Fourth Localized Mode	49882	53808	7.9%
Third Out-of-Plane Mode	—	59226	—

with the lumped-mass model. The desired spectral features in the experimental response are the low frequency resonance (1), which occurred at approximately 8 kHz, corresponding to the bulk in-plane mode, and the higher frequency responses (A)-(D), occurring between approximately 38 kHz and 50 kHz (with a spacing of about 4 kHz), corresponding to the localized microbeam modes (Figure 2.4b illustrates one localized microbeam mode). All in-plane modes of oscillation were verified using stroboscopic imagining equipment from Polytec. The modes that were not predicted by the lumped-mass model, (2) and (3), occurring at approximately 20 kHz and 36 kHz, were predicted by three-dimensional finite element simulations [Figure 2.4c shows the characteristic shape of mode (3)] and correspond to out-of-plane modes. Note that frequency data corresponding to all of the system's resonance is tabulated in Table 2.2. Also note that since resonance (3) occurred close to resonance (A), there was a reduction in the resonant amplitude of (A). Due to the inherently small nature of the localized mode amplitudes, any further reduction in amplitude could be detrimental to the signal to noise ratio and therefore the performance of the sensor in practical implementation. Future sensors should be (and indeed have been) carefully designed such that all unwanted modes are sufficiently separated from the modes of interest.

To simulate mass detection the frequency response of the shuttle mass was recorded before and after the deposition of a small patch of platinum onto the highest frequency microbeam. The platinum patch (shown in Figure 2.6), deposited using a focused ion beam, measured $1.57 \times 5.10 \times 0.22$ μm and had an approximate mass of 38 pg. (Note, this patch was added to the tip of the microbeam so that the effective stiffness was largely unaffected.) The responses of the shuttle mass measured before and after deposition (zoomed in on the four resonances corresponding to the localized microbeam modes) are shown in Figure 2.7. It is apparent that resonance (D), the localized mode of the highest frequency microbeam (the mass loaded microbeam),

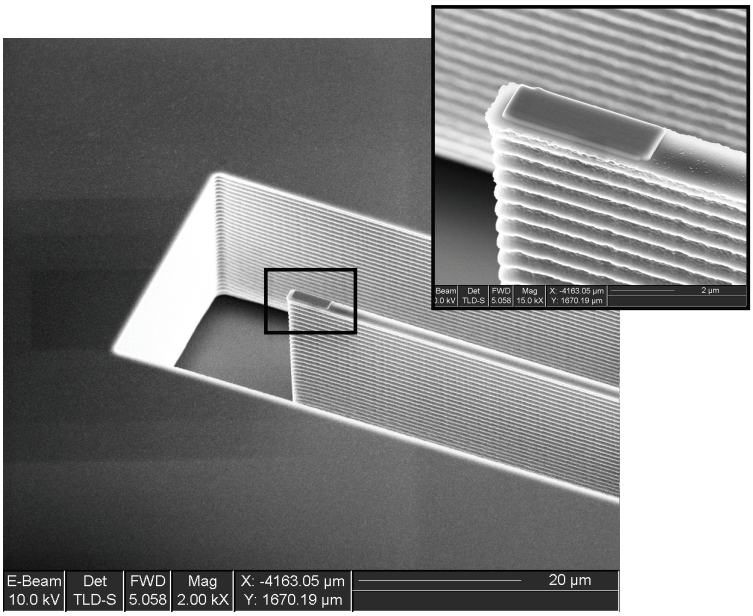

Figure 2.6. A scanning electron micrograph of the platinum patch added to the shortest microbeam (From References [172–174]). The inset, which was used for measurement purposes, shows a closer view. The patch measures approximately 1.57 x 5.10 x 0.22 μm in size and has a mass of approximately 38 pg, as computed volumetrically.

.

has been altered much more than resonances (A)-(C). The markedly larger shift in the mass loaded microbeam resonance as compared to the unloaded microbeam resonances is a direct result of vibration localization. A higher resolution sweep near resonance (D), shown in Figure 2.8, reveals a shift of 124 Hz. Performing the same high resolution sweep near resonance (C), shown in Figure 2.9, reveals a much smaller shift of 3 Hz, which is 40 times smaller than that of the loaded microbeam. Again, due to strong mode localization, the resonance shift associated with the loaded microbeam was significantly larger than that of the unloaded microbeams.

2.4 Sensor Metrics

In order to quantify the performance of the device presented here, and ultimately facilitate comparison between it and other resonant mass sensors, a few representative

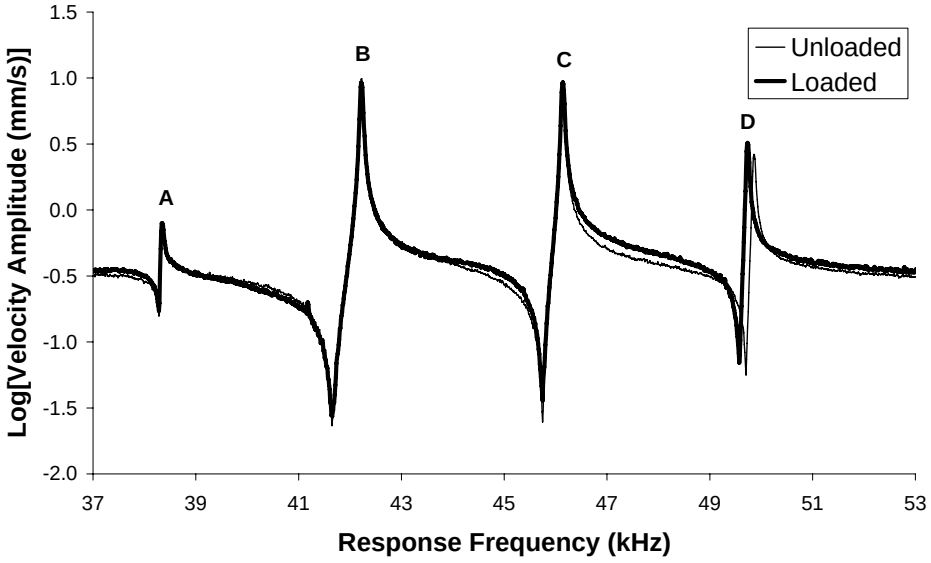

Figure 2.7. Experimentally-obtained frequency response for the sensor depicted in Figure 2.1 actuated with a 12.2 V AC signal in 275 mTorr pressure (From References [172–174]). Note that the added-mass loading introduces shifts in each of the system's resonances, the largest of which occurs in resonance (D), which corresponds to the localized mode of the corresponding beam. Here, and in Figures 2.8 and 2.9, individual data points have been removed for clarity.

.

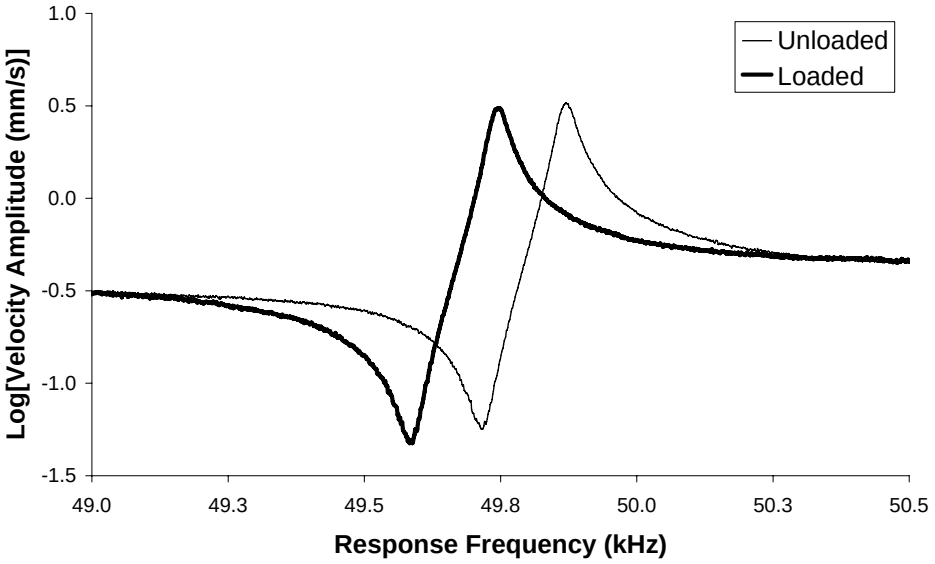

Figure 2.8. Experimentally-obtained frequency response near resonance (D) for the sensor depicted in Figure 2.1 actuated with a 12.2 V AC signal in 275 mTorr pressure (From References [172–174]). Note that the mass loading introduces a resonance shift of approximately 124 Hz.

.

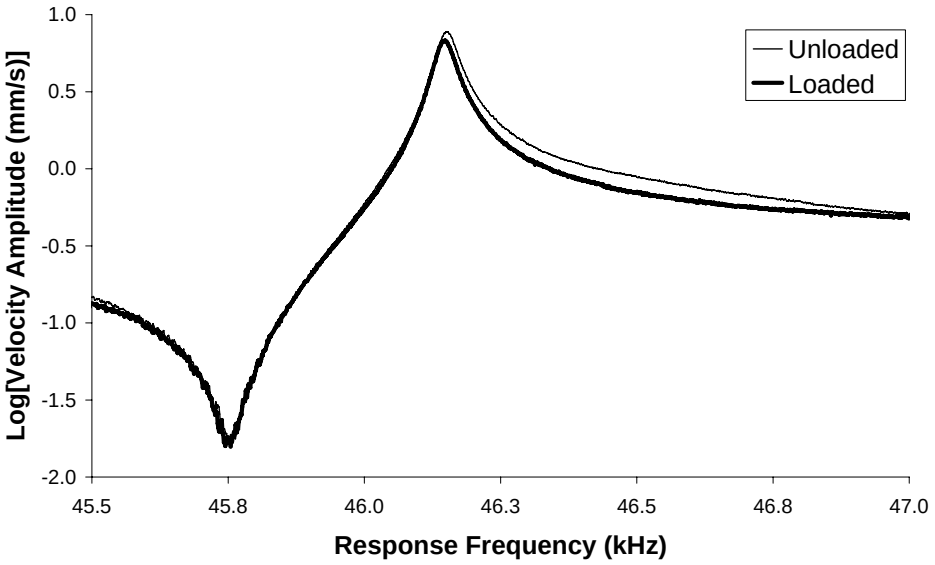

Figure 2.9. Experimentally-obtained frequency response near resonance (C) for the sensor depicted in Figure 2.1 actuated with a 12.2 V AC signal in 275 mTorr pressure (From References [172–174]). Note that the mass loading introduces a resonance shift of approximately 3 Hz.

.

metrics are considered. An approach akin to that presented in Reference [182] is adopted and extended to accommodate the system's multiple degrees of freedom.

For mass sensors, the most pertinent performance metric is a measure of the smallest added mass that can be accurately detected using the given device, or the sensor's so-called mass sensitivity. In the case of resonant devices, this measure can be represented as the product of two independent metrics: mass responsivity (actually its inverse), which quantifies the extent to which a system's resonant frequency will change with a small mass addition; and frequency resolution, which specifies the smallest frequency shift that can be accurately measured in the presence of noise and uncertainty. Assuming that sensor/analyte interactions result solely in mass addition (the subsequent discussion can be easily extended to account for stiffness changes in applications where stiffness contributions are non-negligible), the mass sensitivity of a SDOF mass sensor can be approximated by

$$\partial m \approx S^{-1} \partial \omega_0, \tag{2.12}$$

where S is the device's mass responsivity and $\partial\omega_0$ is the system's frequency resolution. For the multi-degree-of-freedom (MDOF) sensor detailed here this can be extended to account for N resonance shifts induced by up to N mass changes. This results in a mass sensitivity vector, Δm, given by

$$\Delta m \approx \mathbf{S}^{-1} \Delta \omega, \tag{2.13}$$

where $\mathbf{S}$ represents the square $(i \times j)$ mass responsivity matrix, which is composed of elements that quantify the shift in ith resonance of the system due to mass addition at the jth oscillator, and the vector $\Delta\omega$ dictates the frequency resolution associated with each of the system's resonances.

The mass responsivity matrix $\mathbf{S}$ associated with the device shown in Figure 2.1 can be partially compiled using the experimental results detailed in the previous section. For example, the (5,5) element of the matrix, corresponding to the mass responsivity

of resonance (D) with respect to a mass addition to the highest frequency microbeam, can be computed to be 3.3 Hz/pg. Similarly, the mass responsivity associated with resonance (C) computed with respect to a mass addition on the highest frequency microbeam, which corresponds to the matrix's (4,5) element, can be shown to be approximately 0.1 Hz/pg. Extending this procedure through further experimentation will reveal a diagonally-dominant mass responsivity matrix. This can be attributed to the localized nature of the response, which, as detailed in the previous section, leads to significantly larger shifts in the resonances associated with the localized modes of the mass loaded microbeams (as compared to those shifts induced solely through coupling).

It is important to note that though the experimentally-determined mass responsivity of the mass loaded microbeam is comparable to other reported values for resonant multi-analyte sensors, these values are significantly lower than those reported for sensors based on isolated microresonators [9, 11, 152]. Though much of this difference can be attributed to the larger scale of the devices considered here and can be rectified through device scaling, it is important to note that the mass responsivities of these devices (and microsensors based on coupled system architectures, in general) will always be slightly inferior to those of other microsensors (i.e. those based on isolated microresonators). This is due to the inter-oscillator coupling, which manifests itself in the off-diagonal terms of the responsivity matrix, which in the presence of added mass leads to small shifts in each of the system's resonances, not just that associated with the localized mode of the altered beam. Current design studies, the results of which will be (and are being) incorporated into second-generation devices, are aimed at minimizing these off-diagonal terms while still allowing for the measurement of the response of a common shuttle mass that supports the individual sensor elements.

Despite the fact that thermomechanical noise, absorption-desorption noise, temperature fluctuations, and other factors known to contribute to a system's frequency

resolution have been studied in the context of SDOF resonant mass sensors (see, for example, References [182, 183]), to the best of the author's knowledge, the impact of these effects in coupled oscillator systems has thus far not been considered. As such, present understanding facilitates, at best, a conservative estimate of the frequency resolution(s) associated with the sensor/experimental setup described herein. Currently, the frequency resolution is believed to be limited by the resolution of the spectrum analyzer/laser vibrometer system detailed in Section 2.3 and thus a conservative frequency resolution estimate of 1.5 Hz, which is significantly larger than the smallest frequency shift measurable with the experimental setup, is assumed for each of the system's resonances. This results in sub-picogram mass sensitivities for the sensor in its current experimental configuration. In final device implementations, however, additional hardware components, such as phase locked loops, may appreciably alter this resolution. As such, ongoing studies are aimed at extending the results of Reference [182] to MDOF devices in hopes of refining this approximation.

2.5 Design and Integration Issues

Though the preliminary results detailed thus far in the present work (obtained from a first-generation device) are believed to be a positive indication of the feasibility of the SISO, multi-analyte sensor, a number of design and integration issues must still be addressed prior to the implementation of these devices. The following subsections detail the most pertinent issues.

2.5.1 Response Measurement

A fundamental issue that must be addressed in the design of any SISO, multi-analyte sensor is the method of response measurement. In the present work, all of the included data was recovered optically through laser vibrometry. However, for most applications this laboratory-based technique is impractical. An obvious alternative is to utilize the

unused sets of electrostatic comb drives incorporated in the first-generation device design in a capacitive detection scheme. However, the capacitance differences induced by the displacement of the shuttle mass, even during near-resonant operation, are of insufficient magnitude (approximately 0.4 fF) to be accurately measured with off-chip electronics. On-chip CMOS electronics may facilitate the detection of these small differential capacitances, but the exploitation of alternative transduction mechanisms is likely a more practical approach. Presently, the author is considering the integration of piezoelectric or magnetomotive elements into future generation designs. Both of these techniques yield readily-attainable, response-proportional voltages and have been successfully integrated in micro- and nano-scale devices in other contexts [164, 184].

2.5.2 System Integration

Highly intertwined with the design issues detailed in the previous section is the integration of the resonant microsensor with integrated or external circuitry capable of measuring the resonance shifts induced in the system's response during analyte detection. Currently, phase locked loops are exploited for such purposes, but it is not readily apparent that such circuits will suffice (or be efficient) for MDOF systems that exhibit multiple resonance shifts. Ongoing research is aimed at examining this approach, as well as a number of alternatives, including the post-processing of acquired data using computer algorithms.

2.5.3 The Inclusion of Additional Sensing Elements

Though the device design described in Section 2.3 is capable of detecting up to four distinct analytes, full exploitation of the SISO, multi-analyte sensor concept requires the inclusion of additional sensing elements (microbeams). Accordingly, future generations of SISO sensors are slated to incorporate ten or more uniquely functionalized

microbeams. While this increased value of N is readily obtainable with careful design, it is important to note that there are practical constraints on the number of microbeams implementable in a single sensor. Specifically, given a non-resonant frequency window of bandwidth B, the number of microbeam resonances (and thus the number of microbeams) that can fit within the specified band, can be approximated by

$$N_{max} \approx \frac{BQ_{nom}}{\omega_{nom}}, \tag{2.14}$$

where ω_{nom} and Q_{nom} represent the nominal frequency (e.g. the mean resonant frequency of the localized microbeam modes) and quality factor (e.g. the mean Q value, computed with respect to half-power points) associated with the coupled microbeam resonances, respectively. In the event that N_{max} proves insufficient for a given application, it may be possible to exploit multiple non-resonant frequency bands. This, however, will require extremely careful design and relatively tight constraints on both geometric and material property uncertainty.

2.5.4 Environmental Issues

Though the first-generation device examined herein operated successfully in a partial vacuum environment (275 mTorr), simulated mass detection proved unsuccessful at 1 atm. While mass sensing in partial vacuum may be suitable for some applications, the vast majority will require that the device operate in ambient pressures. Accordingly, future generations of SISO, multi-analyte sensors must be designed to operate in ambient environmental conditions. In the present device, fluid pumping between the microbeam oscillator and the sidewalls of the device's substrate is believed to be the primary limiting factor. This can likely be remedied in future-generation devices through device scaling, the removal of excess substrate material, and geometrical reconfiguration. More radical changes, including the use of alternative geometries and/or the application of feedback control [185] or parametric amplification [129],

may be worth consideration if these changes prove insufficient.

2.5.5 Surface Functionalization

As detailed in Section 2.3, mass addition was realized in this work via the deposition of a small platinum patch on one of the sensor's microbeams. However, in implementation the system's microbeam oscillators will have to be functionalized with chemically-selective surface layers. Given the considerable amount of research that has focused on the development of chemically-active surfaces for use in microcantilever sensors (see, for example, References [12, 142, 145, 151, 186]), the present intent is to adopt one of the many previously developed functionalization schemes in next-generation, SISO devices to realize the detection of multiple analytes.

2.6 Ongoing Research: Second-Generation Devices

In an attempt to overcome some of the design and integration issues detailed above, a second generation of SISO, multi-analyte sensors is current being developed. This new generation of devices is founded upon the design principles delineated in previous sections, but utilizes suspended microchannels with internal flow-through, as well. This innovative approach, as detailed in References [22–24], not only negates many of the issues associated with low-Q operation and external functionalization, but also allows for fluid-based bio-molecular detection (in addition to conventional chemical sensing), which can be highly beneficial in a variety of medical research applications.

Figure 2.10 depicts a preliminary second-generation device design. Though not explicitly depicted, this device features both internal flow-through (i.e. isolated microfluidic channels) and magnetomotive transduction (i.e. electromagnetic actuation and sensing). Collectively, these additional design elements are expected to alleviate most, if not all, of the concerns expressed in Section 2.5. Not surprisingly, the inclusion of suspended microchannels also leads to added complexity in design. This

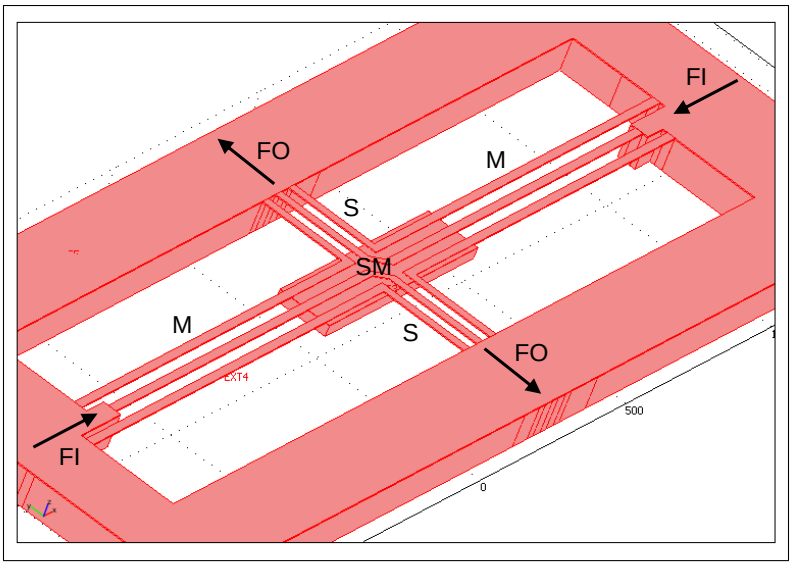

Figure 2.10. Schematic of a representative second-generation, SISO, multi-analyte sensor design. Note that the sensor utilizes internal flow-through in a manner similar to the devices detailed in References [22–24]. Also note that fluid inlets are labeled FI, fluid outlets FO, flexural supports S, functionalized microbeams M, and shuttle mass SM.

.

complexity is principally manifested in the placement/selection of a given sensor's resonant frequencies. Unlike, the system shown in Figure 2.1, which can be designed using back-of-the-envelope calculations, the device depicted in Figure 2.10 requires the iterative use of computer-based finite element techniques (or a shape and size optimization scheme). Figure 2.11 and Table 2.3 detail the carefully-tailored modal behavior of the device depicted in Figure 2.10, which was developed using the aforementioned iterative design process (and is currently being fabricated and tested). Note that equally-spaced and well-isolated localized modes have been (nearly) realized. While this design represents a positive first step towards the successful implementation of the second-generation devices briefly detailed here, an appreciable amount of work remains. Foremost amongst the various unresolved design issues are the effects of fluid-induced internal moments and shear forces, internal fluid damping, and pressure-induced stiffening. These issues, amongst a number of others, are currently being investigated.

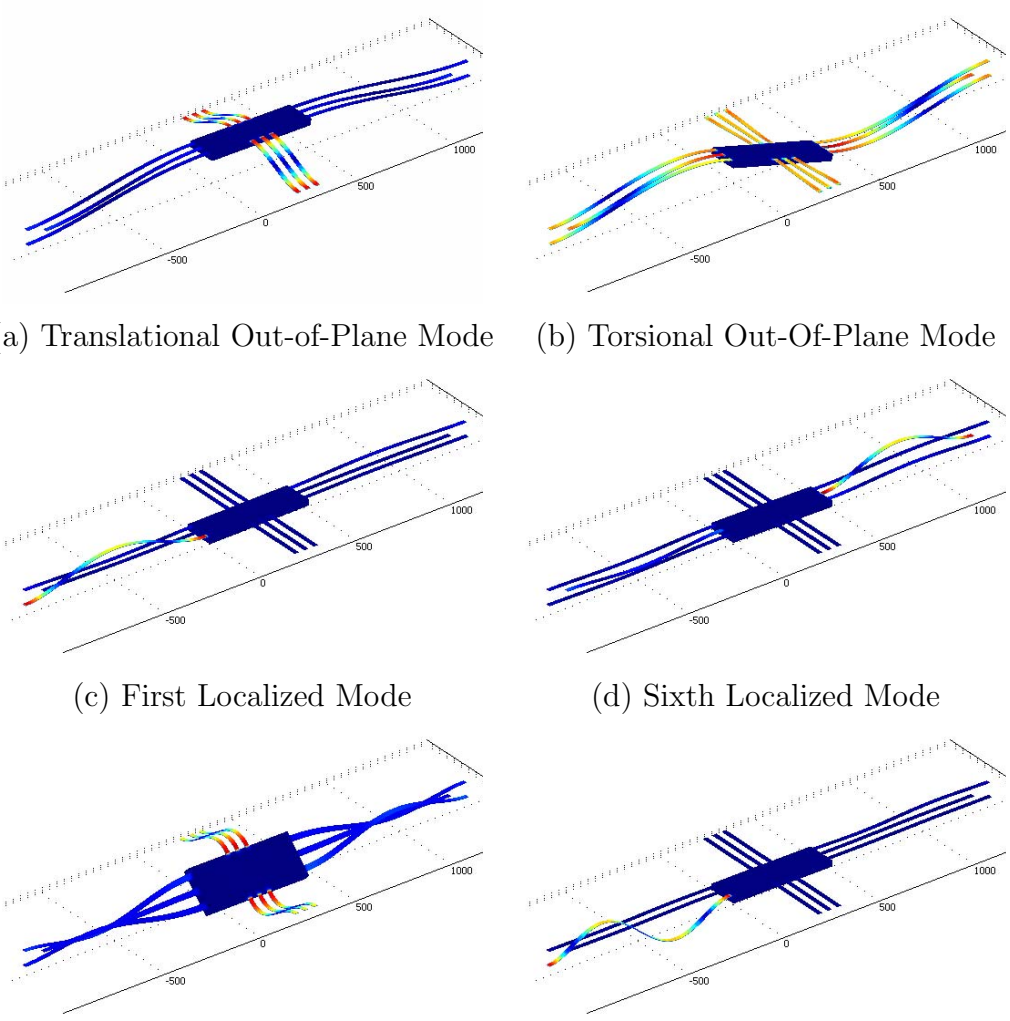

(a) Translational Out-of-Plane Mode (b) Torsional Out-Of-Plane Mode

(c) First Localized Mode (d) Sixth Localized Mode

(e) Torsional Out-Of-Plane Mode (f) Higher-Order Localized Mode

Figure 2.11. Representative mode shapes, recovered through the use of finite element methods, for the device shown in Figure 2.10. Note the localized nature of the modes depicted in (c), (d), and (f). Also note that the other four low-frequency, localized modes are not depicted here for the sake of brevity.

.

Table 2.3. Natural frequencies of the first ten mode shapes of the device depicted in Figure 2.10. Note that these were recovered using computer-based finite element methods.

Mode	Natural Frequency (Hz)
Translational Out-of-Plane Mode	8577
Torsional Out-of-Plane Mode	10163
First Localized Mode	28592
Second Localized Mode	31084
Third Localized Mode	33611
Fourth Localized Mode	36231
Fifth Localized Mode	38817
Sixth Localized Mode	41559
Torsional Out-of-Plane Mode	46000
First Higher-Order Localized Mode	78847

CHAPTER 3

Electrostatically-Actuated Microbeams with Purely-Parametric Excitations

As briefly detailed in the introduction, the general goal of this chapter is to provide a brief, yet thorough, analysis of electrostatically-actuated microbeams with purely-parametric excitations. Specifically, the chapter examines the response characteristics of nonlinear, parametrically-excited microbeam systems that are believed to have practical utility as resonant mass sensors. The chapter begins in Section 3.1 with the presentation of a continuous system model for a microbeam driven by symmetric electrostatic actuation. In Section 3.2, this spatiotemporal model is subsequently reduced to a comparatively-simpler lumped-mass analog using modal projection. In Sections 3.3 and 3.4 the pull-in and nonlinear frequency response behaviors of the system are considered, and the chapter concludes in Section 3.5 with a brief discussion of pertinent design and integration issues.

3.1 A Continuous System Model for a Single Microbeam

To facilitate the development of an accurate lumped-mass model, a continuous system model, derived from 'first principles', is first considered. While a variety of such models have been proposed in literature, that presented in References [68, 158, 160], based on previous aeroelastic plate models developed in References [187] and [188],

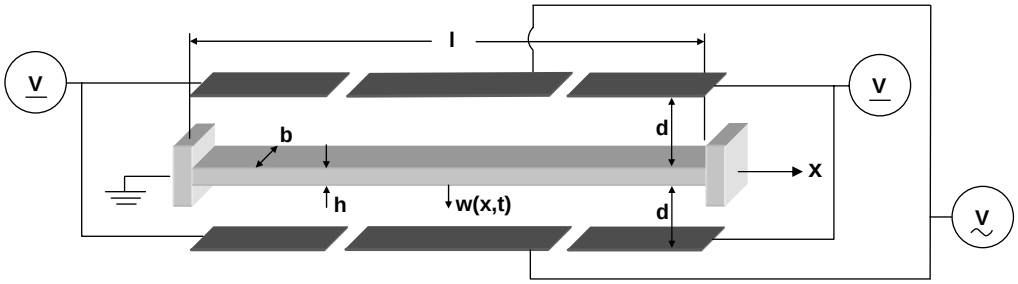

Figure 3.1. A schematic of a special case of the proposed microbeam system (From Reference [105]). Note that in this special case the beam is actuated by three electrode pairs, two of which provide DC excitation while the third provides AC excitation.

is used as a basis of study here.

Assuming that the microbeam system of interest can be accurately modeled as a suspended, fixed-fixed beam (the work is easily extendable to cantilevered systems) actuated using an external electrostatic force (see Figure 3.1), the equation of motion governing the beam's transverse displacement, $w(x,t)$, can be written as [68, 158, 160]

$$EI\frac{\partial^4 w}{\partial x^4} + \rho A\frac{\partial^2 w}{\partial t^2} + c\frac{\partial w}{\partial t} - \left[N + \frac{EA}{2l}\int_0^l \left(\frac{\partial w}{\partial x}\right)^2 dx\right]\frac{\partial^2 w}{\partial x^2} = f_{es}(x,t), \qquad (3.1)$$

with boundary conditions

$$w(0,t) = 0, \qquad w(l,t) = 0, \qquad \left.\frac{\partial w}{\partial x}\right|_{(0,t)} = 0, \qquad \left.\frac{\partial w}{\partial x}\right|_{(l,t)} = 0, \qquad (3.2)$$

where E and ρ (the Modulus of Elasticity and density, respectively) represent the elastic material's properties, I defines the second moment of area, c delineates the viscous damping coefficient, N delineates the uniform applied axial force (a byproduct of microfabrication), and $f_{es}(x,t)$ represents the electrostatic actuation force per unit length. Given that the electrostatic interaction between the beam and the multiple electrodes (see Figure 3.1) can be modeled as a parallel-plate capacitor with a single moving plate, the attractive electrostatic actuation force per unit length, f_{es} can be approximated by

$$f_{es}(x,t) = \sum_i^P \frac{1}{2}\varepsilon_0 b\left[\frac{V_i^2(t)}{(d-w)^2} - \frac{V_i^2(t)}{(d+w)^2}\right]\left[H\left(x-a_i\right) - H\left(x-b_i\right)\right] \qquad (3.3)$$

where

$$H\left(x-\varphi\right)=\begin{cases}1 & x\geq\varphi\\ \\ 0 & x<\varphi\end{cases}, \tag{3.4}$$

ε_0 represents the free space permittivity, and $V_i(t)$ represents the actuation voltage applied to the ith electrode.

To facilitate analysis it proves convenient to nondimensionalize Equation (3.1) in a manner similar to that presented in References [68, 158, 160]. Accordingly, both the transverse displacement, w, and spatial coordinate, x, are normalized by characteristic lengths of the system, the gap width and beam length, respectively, according to

$$\hat{w}=\frac{w}{d} \tag{3.5}$$

and

$$\hat{x}=\frac{x}{l}, \tag{3.6}$$

and time is nondimensionalized by a characteristic period of the system according to

$$\hat{t}=\frac{t}{T}, \tag{3.7}$$

where

$$T=\sqrt{\frac{\rho bhl^4}{EI}}=\sqrt{\frac{12\rho l^4}{Eh^2}}. \tag{3.8}$$

Likewise, the input voltages are normalized by a characteristic voltage of the system, V_C (for example, the DC static pull-in voltage), according to

$$\hat{V}_i(\hat{t})=\frac{V_i(\hat{t})}{V_C}. \tag{3.9}$$

This procedure results in a new equation of motion, given by

$$\begin{aligned}&\frac{\partial^4\hat{w}}{\partial\hat{x}^4}+\frac{\partial^2\hat{w}}{\partial\hat{t}^2}+\hat{c}\frac{\partial\hat{w}}{\partial\hat{t}}-\left[\hat{N}+\alpha_1\Gamma(\hat{w},\hat{w})\right]\frac{\partial^2\hat{w}}{\partial\hat{x}^2}\\ &\qquad=\alpha_2\sum_i^P\hat{V}_i^2(\hat{t})\left[\frac{1}{(1-\hat{w})^2}-\frac{1}{(1+\hat{w})^2}\right]\left[H(\hat{x}-\hat{a}_i)-H(\hat{x}-\hat{b}_i)\right],\end{aligned} \tag{3.10}$$

Table 3.1. Operator and parameter definitions corresponding to the equation of motion presented in Equation (3.10).

Parameter/Operator
$\Gamma\left[f_1(\hat{x},\hat{t}), f_2(\hat{x},\hat{t})\right] = \int_0^1 \frac{\partial f_1}{\partial \hat{x}} \frac{\partial f_2}{\partial \hat{x}} d\hat{x}$
$\hat{c} = \frac{cl^4}{EIT} \qquad \hat{N} = \frac{Nl^2}{EI}$
$\hat{a}_i = \frac{a_i}{l} \qquad \hat{b}_i = \frac{b_i}{l}$
$\alpha_1 = 6\left(\frac{d}{h}\right)^2$
$\alpha_2 = \frac{6\varepsilon_0 l^4 {V_C}^2}{Eh^3 d^3}$

with boundary conditions given by

$$\hat{w}(0,\hat{t}) = 0, \qquad \hat{w}(1,\hat{t}) = 0, \qquad \left.\frac{\partial \hat{w}}{\partial \hat{x}}\right|_{(0,\hat{t})} = 0, \qquad \left.\frac{\partial \hat{w}}{\partial \hat{x}}\right|_{(1,\hat{t})} = 0. \tag{3.11}$$

Note that the parameters and operators that appear in these equations are defined in Table 3.1.

As the form of the forcing presented in Equation (3.10) is difficult to analyze directly, it proves convenient to approximate the spatially-dependent portion of the forcing, through a truncated Taylor series expansion, according to

$$\left[\frac{1}{(1-\hat{w})^2} - \frac{1}{(1+\hat{w})^2}\right] \cong 4\hat{w} + 8\hat{w}^3. \tag{3.12}$$

This results in a new approximative equation of motion, which is valid for 'small' $\hat{w}$, of the form

$$\begin{aligned} &\frac{\partial^4 \hat{w}}{\partial \hat{x}^4} + \frac{\partial^2 \hat{w}}{\partial \hat{t}^2} + \hat{c}\frac{\partial \hat{w}}{\partial \hat{t}} - \left[\hat{N} + \alpha_1 \Gamma(\hat{w},\hat{w})\right] \frac{\partial^2 \hat{w}}{\partial \hat{x}^2} \\ &\qquad = \alpha_2 \sum_i^P \hat{V}_i^2(\hat{t}) \left(4\hat{w} + 8\hat{w}^3\right) \left[H(\hat{x} - \hat{a}_i) - H(\hat{x} - \hat{b}_i)\right]. \end{aligned} \tag{3.13}$$

Note that in contrast to a single electrode system, only odd powered electrostatic terms appear in this equation of motion. Additionally, it should be noted that

the Taylor series approximation proves fairly accurate even in the presence of very small geometric asymmetries (e.g. those on the order of manufacturing tolerances), which could give rise to even powered terms and, in turn, small direct excitation and quadratic nonlinear parametric effects (See Section 3.4 for additional details).

As the electrodes shown in Figure 3.1 are capable of providing AC and/or DC excitation (or perhaps both in an obvious extension not considered directly in this work), it proves convenient to separate the electrostatic terms present in Equation (3.13). This results in a modified equation of motion of the form

$$\begin{aligned}\frac{\partial^4\hat{w}}{\partial\hat{x}^4}+&\frac{\partial^2\hat{w}}{\partial\hat{t}^2}+\hat{c}\frac{\partial\hat{w}}{\partial\hat{t}}-\left[\hat{N}+\alpha_1\Gamma(\hat{w},\hat{w})\right]\frac{\partial^2\hat{w}}{\partial\hat{x}^2}\\ &=\alpha_2\sum_m^Q\hat{V}_m^2\left(4\hat{w}+8\hat{w}^3\right)\left[H(\hat{x}-\hat{a}_m)-H(\hat{x}-\hat{b}_m)\right]\\ &\quad+\alpha_2\sum_n^R\hat{\mathcal{V}}_n^2(\hat{t})\left(4\hat{w}+8\hat{w}^3\right)\left[H(\hat{x}-\hat{a}_n)-H(\hat{x}-\hat{b}_n)\right].\end{aligned}\tag{3.14}$$

Note that here terms of the form $\hat{V}_m^2$ arise from DC actuation and those of the form $\hat{\mathcal{V}}_n^2(\hat{t})$ arise from AC actuation. Using this continuous system model a lumped-mass model can be easily formulated.

3.2 Formulation of the Lumped-Mass Model

Though the system model shown in Equation (3.14) is sufficient for some analyses, the system's pull-in behavior and nonlinear response can be adequately characterized using a comparatively-simpler lumped-mass model. Accordingly, the system's spatially-dependent dynamic variable, $\hat{w}(\hat{x},\hat{t})$, is decomposed using the system's mode shapes, namely,

$$\hat{w}(\hat{x},\hat{t})=\sum_i^\infty A_i(\hat{t})\phi_i(\hat{x}).\tag{3.15}$$

Unfortunately, this results in a set of coupled nonlinear ordinary differential equations, which are cumbersome and of limited applicability (given the approximative nature

of most MEMS models). As such, it proves convenient to develop the nonlinear lumped-mass equation of motion from a linear analog of the modal equation, namely,

$$\phi_i^{iv} - \omega_i^2 \phi_i = 0, \tag{3.16}$$

wherein the applied axial load is assumed to be negligible ($\hat{N} = 0$). As realistic values of $\hat{N}$ (as given, for example, in Reference [68]) yield minimal distortion in the $\hat{N} = 0$ linear mode shapes (especially the first, which is used extensively in this work) this proves to be a valid assumption.

Given that first mode behavior should be dominant during operation, the modal expansion presented in Equation (3.15) can be approximated by a single term. Substituting the resulting mode (normalized through the inner product operator) into Equation (3.14) and projecting the result back onto the first mode (through the inner product operator) yields a final lumped mass model of the form

$$\begin{aligned}
&\ddot{A} + \hat{c}\dot{A} + \left[\int_0^1 \phi^{iv}\phi d\hat{x} - \hat{N}\int_0^1 \phi''\phi d\hat{x}\right] A \\
&\quad + \left[-4\alpha_2 \sum_m^Q \hat{V}_m^2 \int_{\hat{a}_m}^{\hat{b}_m} \phi^2 d\hat{x} - 4\alpha_2 \sum_n^R \hat{\mathcal{V}}_n^2(\hat{t}) \int_{\hat{a}_n}^{\hat{b}_n} \phi^2 d\hat{x}\right] A \\
&\quad + \left[-\alpha_1 \Gamma(\phi,\phi)\int_0^1 \phi''\phi d\hat{x}\right] A^3 \\
&\quad + \left[-8\alpha_2 \sum_m^Q \hat{V}_m^2 \int_{\hat{a}_m}^{\hat{b}_m} \phi^4 d\hat{x} - 8\alpha_2 \sum_n^R \hat{\mathcal{V}}_n^2(\hat{t}) \int_{\hat{a}_n}^{\hat{b}_n} \phi^4 d\hat{x}\right] A^3 = 0.
\end{aligned} \tag{3.17}$$

where

$$(\dot{\bullet}) = \frac{d(\bullet)}{d\hat{t}}, \tag{3.18}$$

and

$$(\bullet)' = \frac{d(\bullet)}{d\hat{x}}. \tag{3.19}$$

To ensure harmonic excitation, the driving voltage,$\hat{\mathcal{V}}_n(\hat{t})$, is taken to be

$$\hat{\mathcal{V}}_n(\hat{t}) = \hat{\mathcal{V}}_n\sqrt{1+\cos\hat{\omega}\hat{t}} = \hat{\mathcal{V}}_n\sqrt{1+\cos\omega t} \tag{3.20}$$

where applicable [102]. Following this substitution, Equation (3.17) is rescaled to account for small damping and small electrostatic excitation (assumptions that are typically valid for MEMS resonators, especially those with high-Q). Likewise, the sum of the nonlinear mechanical stiffness, which is generally hardening, and the nonlinear electrostatic stiffness, which is generally softening, is considered small, for reasons explained in Section 3.4, and a nondimensional scaling parameter, ε, is introduced to facilitate analysis. This results in a final lumped-mass model of the form

$$z'' + 2\varepsilon\zeta z' + (1 + \varepsilon\nu_1 + \varepsilon\lambda_1 \cos\Omega\tau)\, z + \varepsilon\,(\chi + \nu_3 + \lambda_3 \cos\Omega\tau)\, z^3 = 0, \qquad (3.21)$$

with parameters defined as in Table 3.2. Interestingly enough, this lumped-mass model is nearly identical to that previously considered by the author in the analysis of microelectromechanical oscillators driven by non-interdigitated comb drives [106, 107]. Accordingly, the results of previous works, namely, References [106, 107], are exploited throughout this chapter, especially in Section 3.4 where the microbeam's dynamic response is considered.

Though the lumped-mass model developed above is sufficient for most analyses, an alternative model based on a least-squares curve fit of the electrostatic force may prove more desirable in studies where the accuracy of the truncated Taylor series approximation is insufficient or in studies where the operating regime for a given device (in terms of displacement) is well known. As their name implies, these alternative models can be developed by fitting the spatially-dependent portion of the exact electrostatic force (in this case after modal truncation and projection) to a cubic function of displacement over a specified displacement operating regime, while enforcing a specified linear force constraint (as realized by manipulating the Scoefficients contained in ν_1, λ_1, ν_3, and λ_3). The net result of such an approach, as detailed in Figure 3.2, is an improvement in the approximate force model over the specified range of displacement. For example, the least-squares model fit over a displacement domain bounded by plus or minus one-half of the gap width yields a maximum error

Table 3.2. Operator and parameter definitions corresponding to the equation of motion presented in Equation (3.21). Note that the prime operator has been redefined.

Parameter/Operator
$$z = A$$
$$\omega_0^2 = \int_0^1 \phi^{iv}\phi d\hat{x} - \hat{N}\int_0^1 \phi''\phi d\hat{x}$$
$$(\bullet)' = \frac{d(\bullet)}{d\tau}, \qquad \tau = \omega_0 \hat{t}$$
$$\Omega = \frac{\hat{\omega}}{\omega_0}, \qquad 2\varepsilon\zeta = \frac{\hat{c}}{\omega_0}$$
$$\varepsilon\nu_1 = \frac{-4\alpha_2 \sum_m^Q \hat{V}_m^2 \int_{\hat{a}_m}^{\hat{b}_m} \phi^2 d\hat{x} - 4\alpha_2 \sum_n^R \hat{\mathcal{V}}_n^2 \int_{\hat{a}_n}^{\hat{b}_n} \phi^2 d\hat{x}}{\int_0^1 \phi^{iv}\phi d\hat{x} - \hat{N}\int_0^1 \phi''\phi d\hat{x}}$$
$$\varepsilon\lambda_1 = \frac{-4\alpha_2 \sum_n^R \hat{\mathcal{V}}_n^2 \int_{\hat{a}_n}^{\hat{b}_n} \phi^2 d\hat{x}}{\int_0^1 \phi^{iv}\phi d\hat{x} - \hat{N}\int_0^1 \phi''\phi d\hat{x}}$$
$$\varepsilon(\chi + \nu_3) = \frac{-\alpha_1\Gamma(\phi,\phi)\int_0^1 \phi''\phi d\hat{x} - 8\alpha_2 \sum_m^Q \hat{V}_m^2 \int_{\hat{a}_m}^{\hat{b}_m} \phi^4 d\hat{x} - 8\alpha_2 \sum_n^R \hat{\mathcal{V}}_n^2 \int_{\hat{a}_n}^{\hat{b}_n} \phi^4 d\hat{x}}{\int_0^1 \phi^{iv}\phi d\hat{x} - \hat{N}\int_0^1 \phi''\phi d\hat{x}}$$
$$\varepsilon\lambda_3 = \frac{-8\alpha_2 \sum_n^R \hat{\mathcal{V}}_n^2 \int_{\hat{a}_n}^{\hat{b}_n} \phi^4 d\hat{x}}{\int_0^1 \phi^{iv}\phi d\hat{x} - \hat{N}\int_0^1 \phi''\phi d\hat{x}}$$

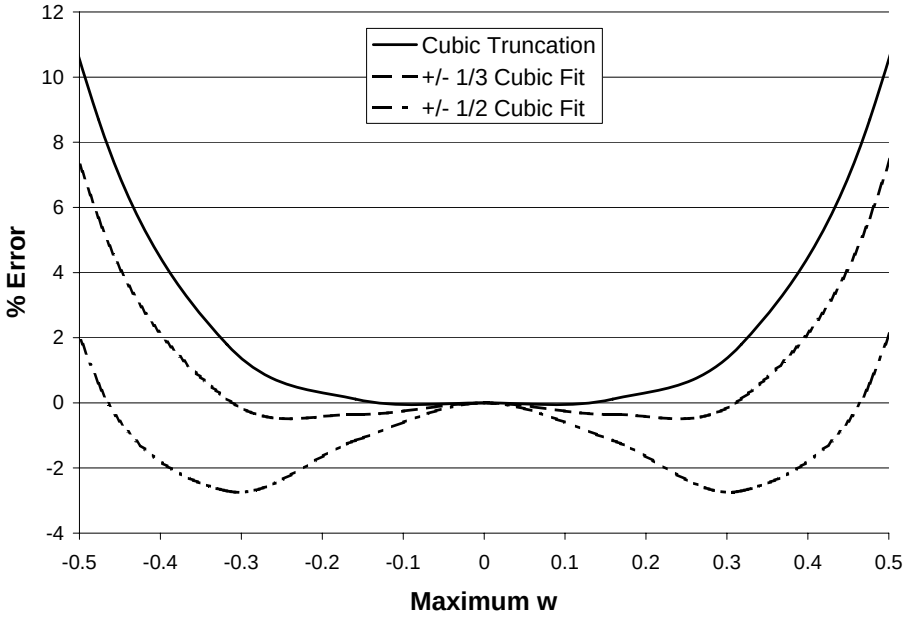

Figure 3.2. Force inaccuracy considered in terms of displacement (limited range) for the various approximative force models (From Reference [105]). Note that as expected, the models produced by curve fitting the electrostatic force over a specified displacement domain exhibit the least error over the given domain.

of about 2.5%, approximately one-fourth of that produced by the truncated Taylor series model. Though such a difference may have minimal consequence with regard to introductory studies, similar to that detailed herein, future studies may benefit from the improvement in accuracy produced by such an approach, especially in cases where global dynamic phenomena (e.g. dynamic pull-in) are of principal concern.

Before proceeding with a discussion of the microbeam system's dynamic response, it proves prudent to briefly detail the operating range wherein the system model and attendant analysis (forthcoming) are believed to be sufficiently accurate for predictive design and, conversely, where limitations in the model and analysis constrain their applicability. To facilitate this discussion, a qualitative phase plane which captures the global behavior of the system, is included in Figure 3.3. Note that the *effective* DC contribution due to both DC ($\hat{V}_m$) and AC ($\hat{\mathcal{V}}_n$) voltage effects has been included within the plot, but AC ($\hat{\mathcal{V}}_n$) voltage effects that directly lead to an *effective* AC

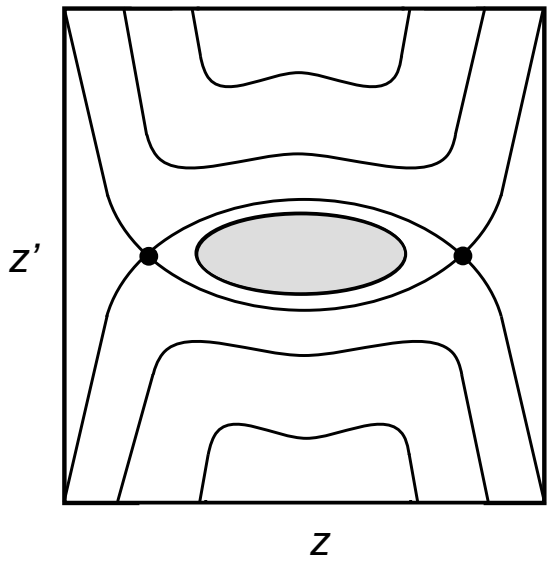

Figure 3.3. A qualitative phase plane for the proposed microbeam system (From Reference [105]). Note that only the *effective* DC electrostatic term (incorporating both DC voltage and some AC voltage effects) is included; inclusion of the AC term would yield perturbations in the solution trajectories shown. Also note that the system model and attendant response analysis, limited by force truncation and perturbation methods, respectively, are believed to be valid only in a local operating region akin to that shaded here.

contribution (and, in turn, to a distortion of the included solution trajectories) have been omitted. In other words, effects due to the term designated ν_1 (which depends on both $\hat{V}_m$ and $\hat{\mathcal{V}}_n$) have been included, while those effects due to λ_1 (which depends on only $\hat{\mathcal{V}}_n$) have been neglected.

Constraints relating to the system model can be generally attributed to the truncation of the Taylor series expansion of the electrostatic force model. Since this truncation requires a magnitude constraint on $\hat{w}$, the system model is accurate only for a limited range of z. Accordingly, the model should only be applied to the predictive design of devices operating in a displacement range bounded by a conservative fraction of the system's gap width – an operating range that is similar to that of most electrostatic sensors and actuators. Constraints relating to the included analysis, discussed in further detail throughout the chapter, can be generally attributed to the nature of the perturbation technique employed. In particular, the local averaging

technique employed in Section 3.4 is applicable only to the local dynamics contained within the heteroclinic cycle (connecting the two saddle points) depicted in Figure 3.3. The analysis of system responses near or outside of this orbit, and thus the analysis of phenomena like dynamic pull-in, would be better facilitated by more global techniques such as those presented in previous works, including References [189, 190]. In light of the limitations detailed above, a conservative qualitative operating region, completely enclosed by the heteroclinic cycle and bounded by a conservative fraction of the system's gap width, is highlighted in Figure 3.3. Within this region, the model and analysis detailed herein should be sufficiently accurate to allow for the predictive design of the proposed devices.

3.3 Pull-In Behavior

Though the impetus of the present study is to explore the nonlinear behavior of a symmetrically-actuated, parametrically-excited microbeam system, as with any electrostatically-actuated MEMS device, it is imperative that the system's pull-in behavior be considered as well. Accordingly, the static pull-in behavior of the system is considered in this section and the dynamic pull-in behavior is discussed, albeit briefly, in the forthcoming section, following a discussion of the system's nonlinear response.

Perhaps the most common 'failure mode' considered in the design of electrostatically-actuated MEMS devices is static pull-in (see, for example, References [160, 191–194]). That is, the operating condition (or conditions in the case of multiple inputs) that leads to destabilization of the system's static operating point. This failure in the proposed parametrically-excited microbeam system is caused by the presence of an electrostatic load in excess of the system's static load bearing capacity. Analytically, this equates to the presence of a negative net linear stiffness in the system's equation of motion. Alternatively, from a bifurcation point of view, the

point at which the failure occurs corresponds to a pitchfork bifurcation in which the stable central equilibrium is destabilized through a merging with the symmetric pair of unstable equilibria. For the system in question here, it is easily shown that the criterion for pull-in is given by

$$\int_0^1 \phi^{iv}\phi d\hat{x} - \hat{N}\int_0^1 \phi''\phi d\hat{x} - 4\alpha_2 \sum_m^Q \hat{V}_m^2 \int_{\hat{a}_m}^{\hat{b}_m} \phi^2 d\hat{x} - 4\alpha_2 \sum_n^R \hat{\mathcal{V}}_n^2 \int_{\hat{a}_n}^{\hat{b}_n} \phi^2 d\hat{x} = 0. \quad (3.22)$$

This expression, in contrast to those associated with most MEM devices, is dependent on both the DC and AC actuation voltages. This can be directly attributed to the form of the excitation used to generate a purely-harmonic excitation.

To explore the static pull-in behavior of the proposed system in further detail, consider the system detailed in Table 3.3 actuated by a single electrode pair (actuated by a single DC voltage input) that spans the beam's length. This system is governed by a static equation of the form

$$\begin{aligned} &\left[\int_0^1 \phi^{iv}\phi d\hat{x} - \hat{N}\int_0^1 \phi''\phi d\hat{x} - 4\alpha_2\hat{V}_0^2 \int_0^1 \phi^2 d\hat{x}\right] A \\ &+ \left[-\alpha_1\Gamma(\phi,\phi)\int_0^1 \phi''\phi d\hat{x} - 8\alpha_2\hat{V}_0^2 \int_0^1 \phi^4 d\hat{x}\right] A^3 = 0. \end{aligned} \quad (3.23)$$

Evoking the fact that pull-in occurs when the net linear stiffness becomes negative, it can be shown that the system should exhibit pull-in at approximately 32.3 V. As shown in Figure 3.4, this prediction is entirely compatible with the behavior governed by Equation (3.23). In fact, due to the enforcement of a linear force constraint in the previously proposed curve fitting techniques, the predicted static pull-in voltage is identical in all three system models developed in the present work (as evident from Figure 3.4).

While the preceding example details the pull-in behavior of a single electrode pair system actuated via a DC voltage, a more relevant example for present purposes is a microbeam system with multiple electrostatic actuation voltages (AC and DC). These systems feature an effective 'pseudo-static' pull-in (the term is used informally here

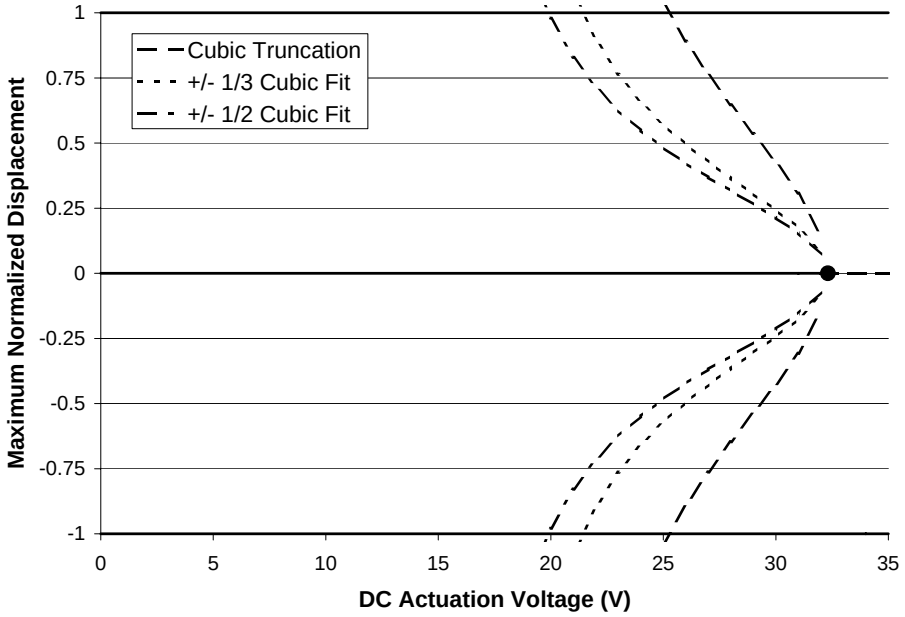

Figure 3.4. Static deflection behavior of the proposed microbeam system as predicted via cubic truncation of the forcing and via curve fitting (From Reference [105]).

Table 3.3. Parameter values for a representative microbeam system.

Parameter Values
$E = 158\,GPa$
$\rho = 2300\,\frac{kg}{m^3}$
$l = 150\,\mu m$
$h = 1\,\mu m$
$b = 10\,\mu m$
$d = 1\,\mu m$
$N = 100\,\mu N$

to designate the operating condition(s) that results in a loss of stability for the trivial solution) behavior that depends on the both the system's AC and DC actuation voltages. Accordingly, pull-in is not governed by a point in a single input parameter space, but rather a curve in a two parameter input space that depends on the electrode geometry of the proposed system. To examine this further, consider a three electrode pair system (similar to that depicted in Figure 3.1), which exhibits a newly defined electrode characteristic $\delta = 0.10$, where δ is defined as half the nondimensional length of the center (AC) electrode. Again, noting that pull-in will occur when the effective linear stiffness becomes negative, the two parameter 'pseudo-static' pull-in curve depicted in Figure 3.5 can be developed. As Figure 3.5 indicates, 'pseudo-static' pull-in is expected for all input voltage combinations that exceed the predicted threshold. To verify this, the system governed by Equation (3.21) was simulated and the respective pull-in points, depicted in Figure 3.5, were recovered. As evident from the figure, the predicted pull-in conforms quite well with (and is conservative with respect to) the simulated results, and while there is some discrepancy for larger AC voltages, this can likely be attributed to dynamic effects. It should be noted that while pull-in is predicted for *all* operating conditions beyond the curve presented, collapse is possible for operating conditions below the curve as well. This is dictated by the nature of the system's nonlinear response and the excitation frequency of the AC voltage input (as described in Section 3.4).

3.4 Dynamic Response

With the static pull-in behavior of the system characterized, attention can turn towards the focus of the present chapter: the microbeam system's dynamic response, the nature of which is perhaps best characterized through the equation of motion presented in Equation (3.21). As noted in Section 3.2, this model is identical in form to that considered by the author in previous works, but incorporates distinct system

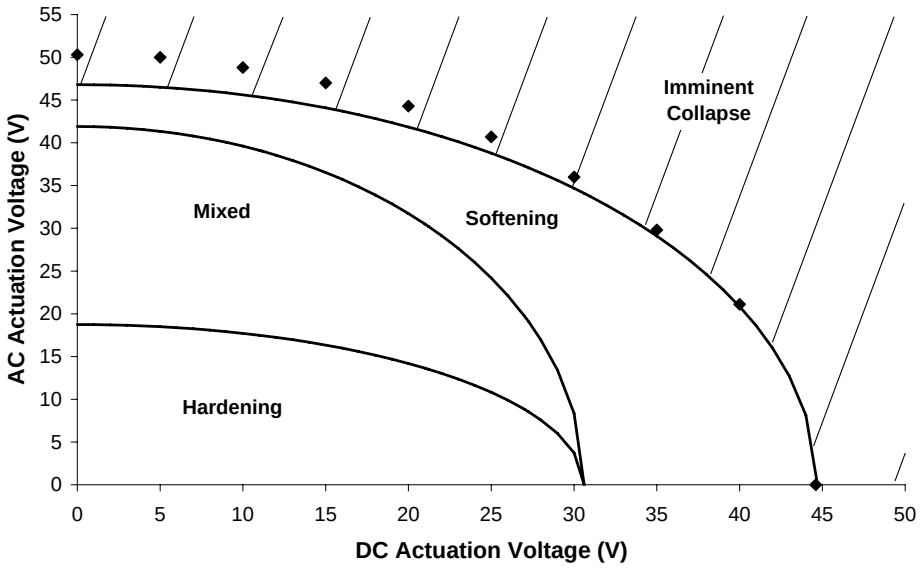

Figure 3.5. A representative two parameter 'pseudo-static' pull-in chart ($\delta = 0.10$) (From Reference [105]). Note that collapse is predicted to occur beyond the noted boundary in the two parameter input voltage space and that the diamonds correspond to points of predicted 'pseudo-static' pull-in obtained via simulation. Also note that collapse is possible below the boundary as dictated by the nature of the system's nonlinear response and excitation frequency.

parameters [106, 107]. Accordingly, interested readers are directed to Reference [107] for detailed information beyond that presented here (including a detailed analysis of the various nonlinear solutions' existence and stability).

As noted in Section 3.2, the equation of motion presented in Equation (3.21) is based on the assumption of 'small' excitation and damping. Likewise, the sum of the hardening nonlinearity, due to mechanical stiffness effects, and the softening nonlinearity, due to electrostatic stiffness effects, is assumed to be small (as achieved through manipulation of the DC bias voltage). This assumption is put in place to distinguish the response of the proposed system from that of electrostatically-actuated resonators dominated by nonlinear mechanical effects. Systems of this type exhibit a nonlinear response that is largely unaffected by electrostatic nonlinearities and thus their response is generally compatible with mechanically-hardening nonlinear oscillators with linear parametric excitation, a topic that has been covered extensively in nonlinear vibrations literature (see, for example, Reference [195]).

To analyze the equation of motion presented in Equation (3.21) it proves convenient to utilize the method of averaging. Likewise, as damping has a minimal effect on the qualitative nature of the system's nonlinear response, it proves convenient to set $\zeta = 0$. Note that the effects of small damping are discussed in some detail in Reference [107].

To facilitate averaging, a standard constrained coordinate transformation given by

$$z(\tau) = a(\tau)\cos\left(\frac{\Omega\tau}{2} + \psi(\tau)\right), \tag{3.24}$$

$$z'(\tau) = -a(\tau)\frac{\Omega}{2}\sin\left(\frac{\Omega\tau}{2} + \psi(\tau)\right), \tag{3.25}$$

is first introduced. Likewise, as near resonant behavior is of principal interest, a detuning parameter, σ, given by

$$\sigma = \frac{\Omega - 2}{\varepsilon}, \tag{3.26}$$

is incorporated. Separating the equation that results from substitution, as well as the state variable constraint equation, in terms of amplitude and phase, and averaging the result over the period $4\pi/\Omega$, results in the system's averaged equations, which are given by

$$a' = \frac{1}{8}a\varepsilon\Big[-8\zeta + \Big(2\lambda_1 + a^2\lambda_3\Big)\sin 2\psi\Big] + \mathcal{O}\Big(\varepsilon^2\Big), \tag{3.27}$$

$$\psi' = \frac{1}{8}\varepsilon\Big[3a^2\left(\chi + \nu_3\right) + 4\nu_1 - 4\sigma + 2\Big(\lambda_1 + a^2\lambda_3\Big)\cos 2\psi\Big] + \mathcal{O}\Big(\varepsilon^2\Big). \tag{3.28}$$

Using Equations (3.27) and (3.28), the steady-state behavior of the microbeam system can be recovered by setting $(a', \psi') = (0, 0)$ and solving for the steady-state values of a and ψ. This process yields a trivial solution and three non-trivial solution branches, the first two of which have amplitudes and phases (note that phases shifted by a multiple of π equate to the same physical response) given by

$$a_1 = \pm\sqrt{\frac{4\sigma + 2\lambda_1 - 4\nu_1}{3\left(\chi + \nu_3\right) - 2\lambda_3}}, \qquad \psi_1 = \frac{\pi}{2}, \tag{3.29}$$

and

$$a_2 = \pm\sqrt{\frac{4\sigma - 2\lambda_1 - 4\nu_1}{3\left(\chi + \nu_3\right) + 2\lambda_3}}, \qquad \psi_2 = 0. \tag{3.30}$$

Generally speaking, these two sets of solution branches are quite similar to those seen in a simple nonlinear oscillator, in that the sign of the term under the square root sign dictates their existence with respect to the forcing frequency (detuning). However, their relationship to the system's overall nonlinear characteristic, is somewhat unique. In particular, due to the differing denominators of each response branch, a single effective nonlinearity, which captures the system's nonlinear behavior, cannot be obtained. Rather multiple effective nonlinearities are required, which reveal the system's nonlinear nature only when collectively considered. To verify this, two effective nonlinearities are defined, as taken from the denominators of a_1 and a_2, according to

$$\eta_1 = 3\left(\chi + \nu_3\right) - 2\lambda_3 \tag{3.31}$$

and

$$\eta_2 = 3\left(\chi + \nu_3\right) + 2\lambda_3. \tag{3.32}$$

As brief analysis reveals, the structure of the system's frequency response differs with the signs of η_1 and η_2. In particular, for $\eta_1 > 0$ and $\eta_2 > 0$ the system locally exhibits a hardening nonlinearity, for $\eta_1 < 0$ and $\eta_2 < 0$ a softening nonlinearity, and for $\eta_1 > 0$ and $\eta_2 < 0$ and $\eta_1 < 0$ and $\eta_2 > 0$ mixed nonlinearities wherein the response branches bend toward or away from one another near resonance [106, 107]. To summarize this result the nonlinear nature of the response can be characterized through consideration of the γ_3 - λ_3 parameter space shown in Figure 3.6. Here γ_3, the effective nonlinear stiffness coefficient, is defined according to

$$\gamma_3 = \chi + \nu_3. \tag{3.33}$$

and λ_3 represents the nonlinear parametric excitation amplitude.

While the signs of η_1 and η_2 largely dictate the nature of the system's nonlinear frequency response, the third solution branch, with amplitude given by

$$a_3 = \pm\sqrt{\frac{-2\lambda_1}{\lambda_3}}, \tag{3.34}$$

can play a significant role as well. However, since the third solution branch's existence is dependent on the sign of λ_1/λ_3, a term that will be positive for most viable configurations of the present system, these solutions are largely unobtainable. Accordingly, only three topologically distinct frequency responses are obtainable here, namely, responses which exhibit hardening, softening, or mixed (response branches bending away from one another) nonlinear characteristics (corresponding to Regions IV - VI in Figure 3.6).

To explore the proposed system's nonlinear response further, consider again the three electrode pair system that was introduced in the preceding section. According to the aforementioned results, the proposed system should be able to exhibit one of

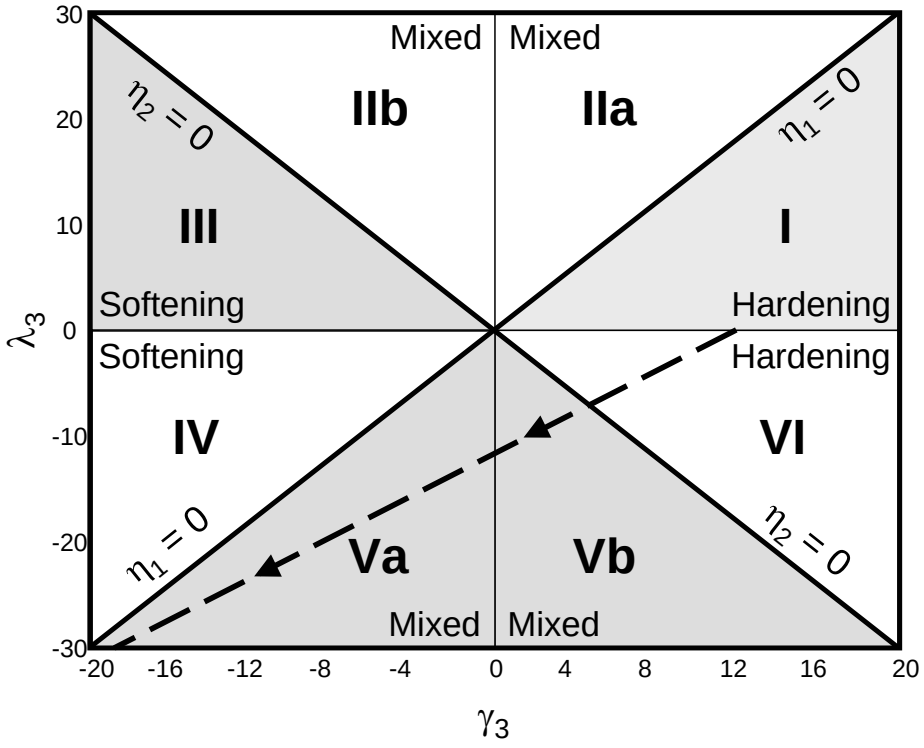

Figure 3.6. The γ_3 - λ_3 parameter space (From References [105, 107]). Those regions designated I and VI exhibit hardening (or quasi-hardening) nonlinear characteristics, those designated III and IV exhibit softening (or quasi-softening) nonlinear characteristics, and those designated IIa, IIb, Va, and Vb exhibit mixed nonlinear characteristics. The devices in question are expected to operate only in the regions designate IV, Va, Vb, and VI. Note that the line included on the plot represents the trajectory followed by the proposed system under a fixed DC voltage of 5 V and a fluctuating AC voltage.

three distinct frequency response structures, as determined by where in the nonlinear parameter space (or in the corresponding two parameter input voltage space, shown in Figure 3.5) the system lies. This is confirmed by Figures 3.7-3.9, which show the system's nonlinear response at three distinct operating conditions in the aforementioned parameter space. As predicted, Figure 3.7 depicts a classical hardening frequency response, Figure 3.9 depicts a classical softening frequency response, and perhaps more interestingly, Figure 3.8 depicts a frequency response wherein the non-trivial response branches bend away from one another near resonance (note that the latter of these responses may prove problematic in implementation, as certain input frequencies lead to unbounded responses – this, however, may be reconcilable through the inclusion of higher order nonlinearities). As evident from Figures 3.7-3.9, each of these responses display desirable characteristics. Perhaps most notably, they each exhibit a stable, non-resonant zero response, which in implementation corresponds to nearly ideal stopband rejection, as well as rapid response roll-off. Both of these characteristics are highly desirable in microresonators.

While the results detailed above are a positive indication of the flexibility of the proposed microbeam system, especially with regard to the potential implementation of softening or hardening devices on the same geometrical platform, it is important to point out the study's limitations. First, while softening behavior is analytically predicted to exist for certain operating conditions, this operating regime lies close to the predicted 'pseudo-static' pull-in point. Accordingly, the system is operating in a regime where *a priori* assumptions begin to break down, most notably due to the presence of $\mathcal{O}(1)$ electrostatic effects. As such, softening regimes may be quite difficult to realize in practical applications. While simulations can provide some clarification of this issue, those completed to date have not yielded definitive results (softening responses have been found for the system design considered herein, but a wide variety of designs have not yet been considered), as such simple experimental

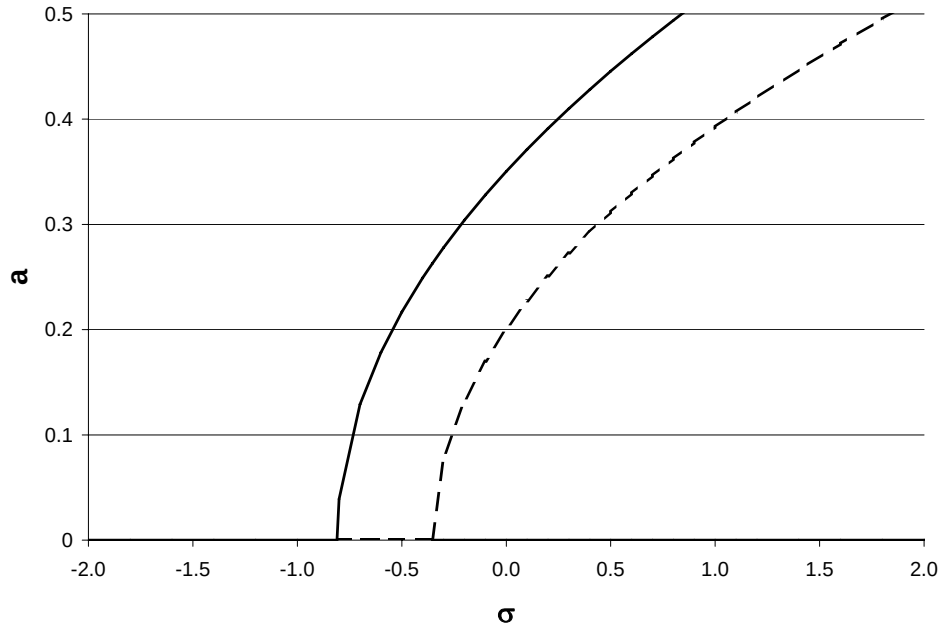

Figure 3.7. Analytically produced frequency response for a representative oscillator excited with 5 V DC and 10 V AC (From Reference [105]). Note the hardening nonlinear characteristic. Also note that here and in Figures 3.8 and 3.9 solid lines indicate a stable response and dashed lines an unstable response.

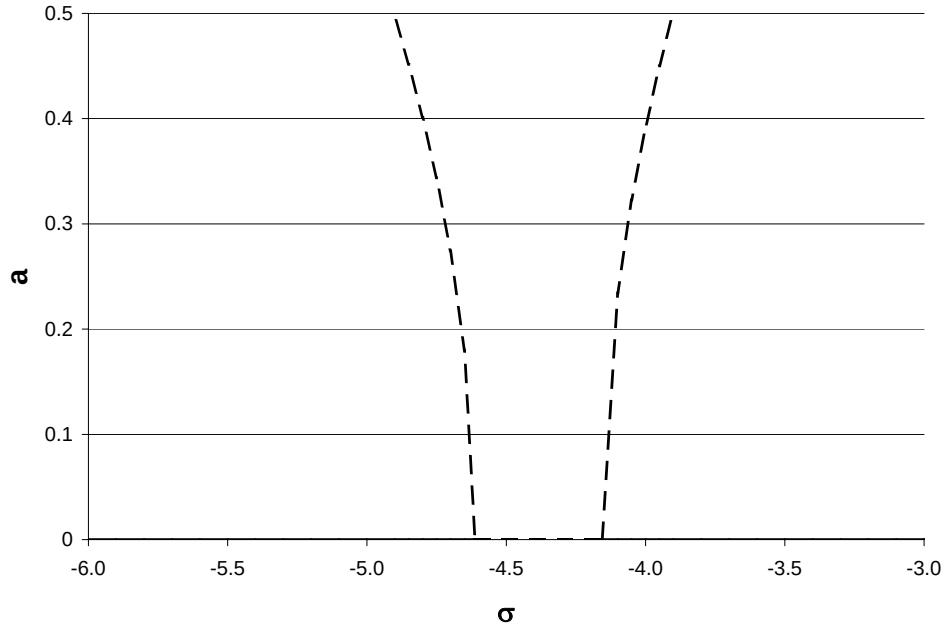

Figure 3.8. Analytically produced frequency response for a representative oscillator excited with 28 V DC and 10 V AC (From Reference [105]). Note the mixed nonlinear characteristic.

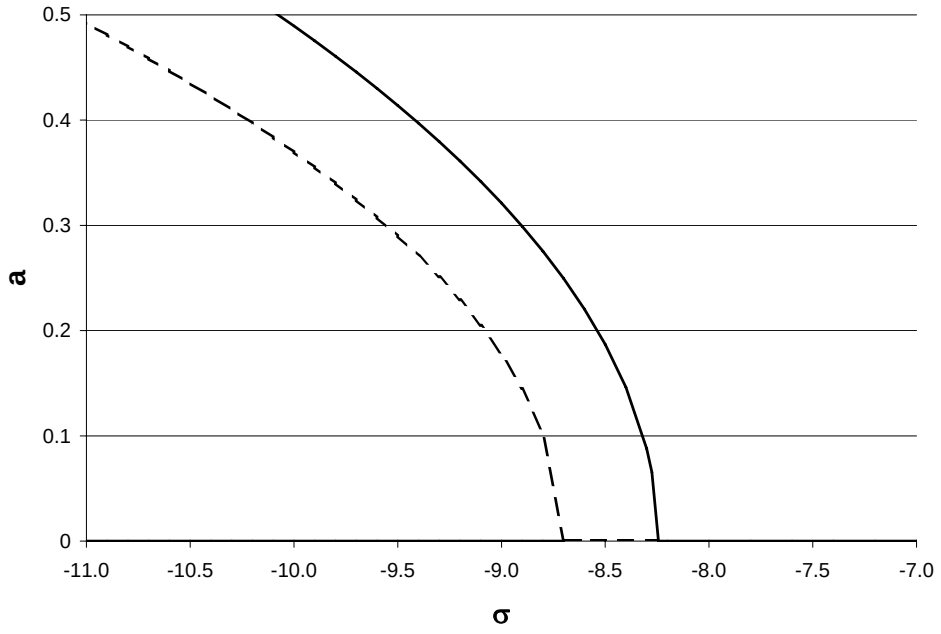

Figure 3.9. Analytically produced frequency response for a representative oscillator excited with 40 V DC and 10 V AC (From Reference [105]). Note the softening nonlinear characteristic.

studies will likely be needed to provide definitive evidence of the softening regime.

Another limitation of the results presented here is that they are based on an approximate force model. While this model is well suited for characterizing local behavior, it does not accurately capture large-amplitude nonlinear frequency response behavior or global system failures, such as those associated with dynamic pull-in. Additionally, the system model does not account for force imbalances arising from either manufacturing imperfections or non-uniform residual stresses. To ensure proper operation, a numerical simulation of a lumped-mass analog of the system presented here was constructed in Simulink$^{\mathrm{TM}}$. The simulation incorporated precise models of the system's linear elastic restoring force and electrostatic restoring and driving forces (no expansions or truncations were used) and an approximative model of the system's nonlinear elastic restoring force. Additionally, asymmetries in the force model, arising from electrostatic or elastic imbalance, were introduced, to ensure that

they did not compromise operation. In general, the results proved quite promising. Though desirable response features, such as absolute stopband rejection, began to deteriorate in the presence of asymmetries, the hardening region proved to be quite robust, with amplitudes and bifurcation points remaining largely invariant (i.e. they shift both in frequency and amplitude by only a small percent), even in the presence of fairly large asymmetries (up to ten percent gap asymmetry or, in the case of elastic asymmetry, ten percent static offset). The softening region proved significantly less robust, but even it featured little degradation in the presence of asymmetries on the order of a few percent, which is about all that can be expected given the proximity of this operating condition to 'pseudo-static' pull-in.

3.5 Design Considerations

As evident from the results of the preceding sections, the proposed microbeam system offers some flexibility for future nonlinear resonant sensor designs. However, inherent to this flexibility are some design complications. In particular, unlike classical parametrically-excited MEM oscillators whose response can be manipulated via various system parameters, which themselves can be varied in a largely independent manner through the design of the comb drives, the behavior of the system in question is tied to a relatively small number of parameters which, when altered, affect both linear and nonlinear response characteristics. In light of this, this section attempts to summarize the aforementioned issues in a manner that may prove useful in the practical design of such devices.

Of utmost importance with any resonant MEMS device, be it a sensor or filter, is the location and width of the system's resonance. Since the proposed system is based on parametric resonance, this is analogous to the classical problem of positioning and orientating a parametrically-excited system's 'wedge of instability', or more specifically, locating and specifying the width of the unstable region of the system's trivial

solution (see, for example, References [106, 107, 195]). For the device in question, this is done by dictating two distinct quantities: the system's purely mechanical natural frequency, which is dependent on the geometry of the microbeam, as well as the axial load in the structure (which is dependent on the nature of the fabrication process amongst other things), and the system's linear electrostatic force, which is largely dependent on the geometric configuration of the electrodes and the magnitude of the system's input voltages. Noting this, it can be shown that for the undamped system the instability region is bounded by the critical frequency (detuning) values of

$$\sigma = \nu_1 \pm \frac{\lambda_1}{2}, \tag{3.35}$$

and centered about the frequency (detuning) value of

$$\sigma = \nu_1, \tag{3.36}$$

as outlined in Reference [107]. As evident from Table 3.2, these critical frequency values, and thus the center frequency as well, are largely dependent on the input voltages of the system (in terms of both location and relative distance). This dependence is confirmed by Figure 3.10, which depicts the system's wedge of instability, for two different DC voltages, in the V_{AC} - Ω parameter space. Similarly, it can be shown that the electrode configuration, as manipulated through the geometric parameter δ (a relative measure of the length of the AC electrode), plays a significant role. In particular, increasing δ produces results consistent with increasing the AC actuation voltage and decreasing the DC actuation voltage for a fixed-δ system.

As highlighted in the previous section, the characteristic form of the system's nonlinearity, and thus the device's mode of nonlinear operation, is dependent on the system's location in the nonlinear parameter space depicted in Figure 3.6, which, in turn, is dependent on the nonlinear mechanical and electrostatic characteristics of the system in question. This is further verified by Figure 3.11, which shows a rudimentary design chart for characterizing this nonlinear parameter effect in terms of the input

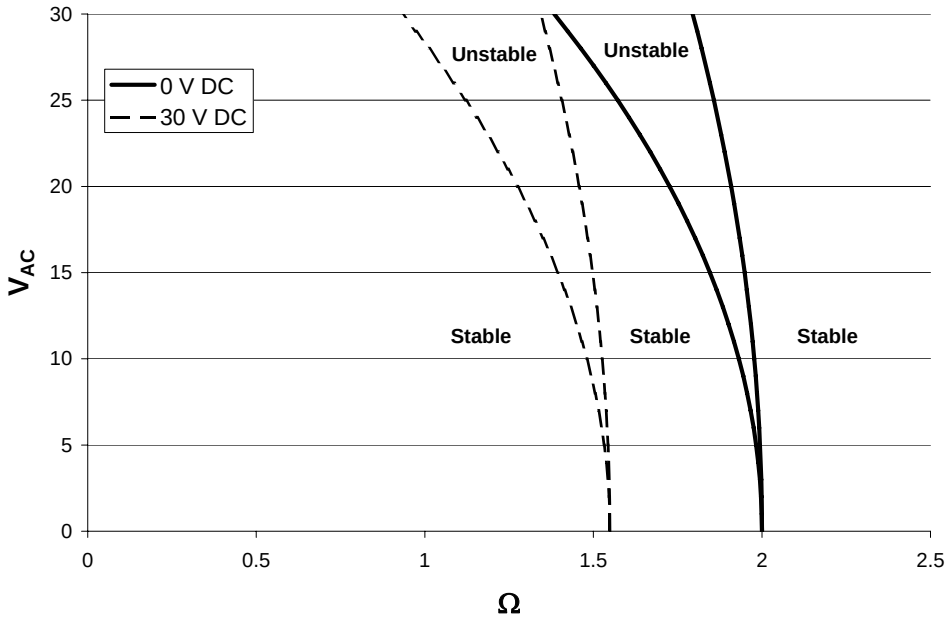

Figure 3.10. Linear instability wedges for the undamped microbeam system actuated at 0 V DC and 30 V DC, respectively (From Reference [105]). The system's zero response is unstable inside of the wedges and stable outside of the wedges. Note that as the DC voltage is increased the instability wedge shifts to the left in the parameter space.

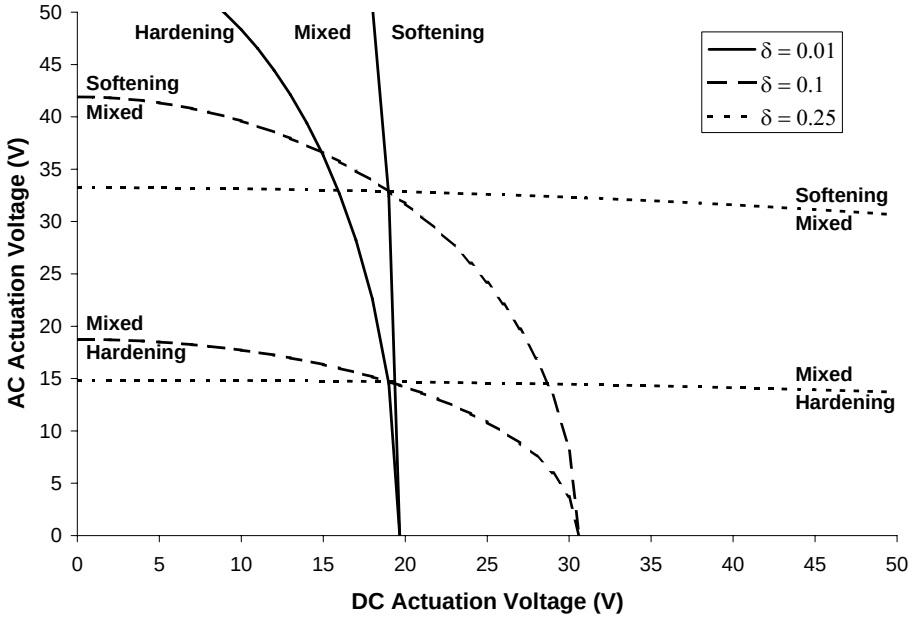

Figure 3.11. Sample design chart for predicting voltage transitions (From Reference [105]). Note that the 'lower' boundaries correspond to transitions between hardening and mixed nonlinear behavior and the 'upper' boundaries correspond to transitions between softening and mixed nonlinear behavior.

voltages and the design parameter δ. As expected, changing the relative size of the electrodes leads to a relative weighting of the appropriate term in the force model, as previously seen in the course of linear design. Accordingly, the nonlinear behavior of the proposed system and the location and width of its linear instability region are highly entwined.

In light of the interdependent nature of the design problem associated with the microbeam system detailed herein, the following iterative strategy is proposed for use in the course of design. To begin, the device's nonlinear mode of operation (most likely hardening, but potentially softening) and allowable operating voltage ranges should be specified. This, in turn, results in approximate magnitude constraints on the relative electrode size and nonlinear mechanical properties of the microbeam. These constraints, in conjunction with a specified purely-mechanical natural frequency (or alternative geometric constraint), can be used to generate a geometric design of the

device in question. The width of the resulting instability zone can then be verified to ensure conformity with the desired characteristic, and the system's 'pseudo-static' (and potentially dynamic) pull-in voltages can be computed to ensure proper device operation. System parameters can then be iteratively 'tuned' until the system's behavior closely matches the desired system behavior.

For reference purposes, it should be noted that the sample device presented in this work was developed via the design strategy detailed above. For this special case, it was desirable to feature a device which exhibited hardening, softening, and mixed nonlinear responses over a practical range of AC and DC voltages, in this case approximately 0 - 50 V. Noting this, viable ranges for δ, α_1, and α_2 were computed. Using these ranges, in conjunction with a nondimensional, purely-mechanical natural frequency target (somewhere on the order of 25, which corresponds to approximately 2.5 MHz) and realistic geometric constraints based on fabrication limitations (e.g. a 1 μm minimum feature size), a potential beam geometry (i.e. l, b, t, d, and δ) was produced (details of which can be found in Table 3.3). Since a specific bandwidth was not needed and pull-in was found to occur outside of, or near the limits of, the voltage operating range, iteration was not needed. However, the beam configuration associated with *this* particular design problem did not appear to be over-constrained and thus bandwidth or pull-in correction via iterative 'tuning' would have been possible, as is generally believed to be the case.

3.6 Nonlinear Resonant Mass Sensing

Though, as detailed above, nonlinear frequency responses with softening characteristics are theoretically obtainable with a given symmetrically-actuated microbeam, the robustness of these nonlinear structures is, at best, sub-optimal. Accordingly, nonlinear resonant mass sensors (such as those detailed in Section 1.5) based on microbeams with purely-parametric excitations should utilize hardening frequency

response structures. While these structures are adequate for quantitative analyte assessment (as they feature readily-computable, albeit complex, response amplitude to added mass relationships), because they lack well defined jump bifurcations (at least on the left hand side of their frequency responses), they have limited applicability as high-sensitivity detectors. Given that an ideal nonlinear mass sensor should be capable of both qualitative and quantitative assessment, ongoing research is focused on alternative transducer designs, namely those detailed in the preceding and forthcoming chapters.

CHAPTER 4

Electromagnetically-Actuated Microbeam Resonators: Introduction and Modeling

As detailed in the introduction, electromagnetically-actuated (EMA) microresonators are believed to have significant potential in a number of engineering applications, including mass sensing. As this potential is inherently tied to the predictability of a given resonator's behavior, the present chapter emphasizes the systematic modeling of the large amplitude oscillations of a representative device. To begin, a spatiotemporal model for the EMA microresonators depicted in Figure 1.3 is developed using classical beam theory. Through the use of modal projection, this distributed model is reduced to a comparatively-simpler lumped-mass model, which is subsequently analyzed in Chapters 5-6 using standard perturbation methods and bifurcation theory. It should be noted that though the system model developed herein was derived specifically for the aforementioned microsystems, the chapter's results are amenable to a variety of parametrically-excited cantilever systems, the analyses of which rarely, if ever, consider the effects of nonlinear parametric excitations (a notable exception is Reference [196]).

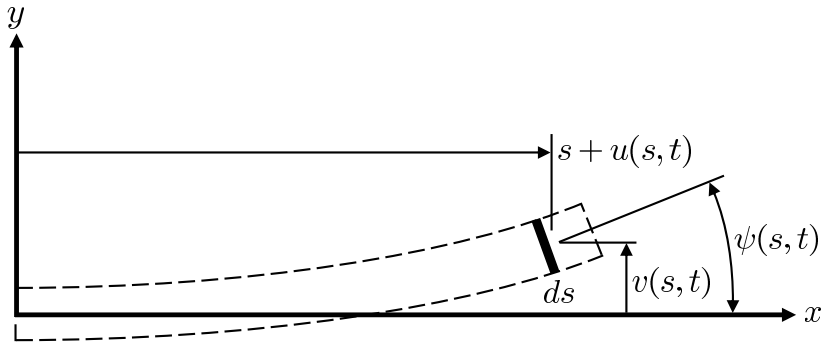

Figure 4.1. Beam element with variable descriptions.

4.1 Formulation of a Distributed-Parameter Model

Given that the electromagnetically-actuated microcantilevers of interest here have been shown (in experiments) to exhibit moderately large response amplitudes near parametric resonance, the distributed-system model used to capture their dynamic behavior must allow for large elastic deformations [171]. As such, the nonlinear, energy-based approach introduced in References [197, 198] and subsequently revisited in Reference [199] is adopted here.

Assuming that the microbeam resonators of interest are uniform and have negligible rotational inertias (the latter assumption is justified by the slenderness of the microbeam systems of interest), the specific Lagrangian of a given oscillator can be approximated by

$$\bar{L} = \frac{1}{2} m \left(\dot{u}^2 + \dot{v}^2 \right) - \frac{1}{2} D \left(\psi' \right)^2 , \tag{4.1}$$

where m and D represent the device's specific mass and flexural stiffness, respectively, and u, v, and ψ are defined as in Figure 4.1. Noting this, and further assuming that the neutral axis of the beam is inextensible, and thus that

$$\left(1 + u'\right)^2 + \left(v'\right)^2 = 1, \tag{4.2}$$

results in a governing variational equation for the system, derived from extended

Hamilton's principle, given by

$$\begin{aligned}\delta H = 0 = \delta \int_{t_1}^{t_2} \int_0^l \left\{ \bar{L} + \frac{1}{2}\lambda \left[1 - \left(1 + u'\right)^2 - \left(v'\right)^2 \right] \right\} ds dt \\ + \int_{t_1}^{t_2} \int_0^l \left(Q_u \delta u + Q_v \delta v \right) ds dt,\end{aligned} \tag{4.3}$$

where l and s represent the beam's total length and arc length variable, Q_u and Q_v represent the planar, non-conservative forces in the u and v directions, respectively, and λ represents a Lagrange multiplier introduced to maintain the inextensibility constraint. Integrating this equation by parts successively, while enforcing the kinematic constraint relating the angle ψ to the planar displacements,

$$\tan\psi = \frac{v'}{1+u'}, \tag{4.4}$$

yields the equations governing longitudinal and transverse dynamics, as well the system's boundary conditions:

$$G_u{}' = \left[A_\psi \frac{\partial \psi}{\partial u'} + \lambda \left(1 + u'\right) \right]' = m\ddot{u} - Q_u, \tag{4.5}$$

$$G_v{}' = \left[A_\psi \frac{\partial \psi}{\partial v'} + \lambda v' \right]' = m\ddot{v} - Q_v, \tag{4.6}$$

$$\left\{ -G_u \delta u - G_v \delta v + H_u \delta u' + H_v \delta v' \right\} \Big|_0^l = 0. \tag{4.7}$$

Note that here and throughout the remainder of the work, A_ψ, H_u, and H_v are given by

$$A_\psi = \frac{\partial^2 \bar{L}}{\partial t \partial \dot{\psi}} + \frac{\partial^2 \bar{L}}{\partial s \partial \psi'} - \frac{\partial \bar{L}}{\partial \psi}, \tag{4.8}$$

$$H_\varphi = \frac{\partial \bar{L}}{\partial \psi'} \frac{\partial \psi}{\partial \varphi'}, \qquad \varphi = u, v. \tag{4.9}$$

In order to decouple Equations (4.5) and (4.6) and ultimately obtain a single equation of motion for the system, the Lagrange multiplier must be extracted from Equation (4.5). To facilitate this, fifth-order Taylor series approximations for both u

and ψ, resulting from the kinematic and inextensibility constraints, are introduced, namely,

$$u(s,t) \approx -\frac{1}{2}\int_0^s \left(v'\right)^2 ds - \frac{1}{8}\int_0^s \left(v'\right)^4 ds, \tag{4.10}$$

$$\psi = v'\left(1 + \frac{\left(v'\right)^2}{6} + \frac{3\left(v'\right)^4}{40} + H.O.T.\right) \approx v' + \frac{\left(v'\right)^3}{6} + \frac{3\left(v'\right)^5}{40}. \tag{4.11}$$

Note that these higher-order expansions are adopted here due to the fact that a third-order, symmetric-potential, nonlinear model is incapable of qualitatively characterizing the nonlinear behavior reported in Reference [171]. While fifth-order expansions are expected to suitably capture the system's dynamics, in reality, an asymmetric model may be required. Ongoing experimentation is aimed at resolving this issue. Assuming ideal cantilever boundary conditions, specifically,

$$u(0,t) = 0, \qquad v(0,t) = 0, \qquad v'(0,t) = 0, \tag{4.12}$$

$$G_u(l,t) = 0 \qquad G_v(l,t) = 0, \qquad H_v - \left.\frac{H_u v'}{1+u'}\right|_{s=l} = 0, \tag{4.13}$$

and that the longitudinal non-conservative force Q_u is accurately represented by a single point load applied at the endpoint of the beam (or more accurately an infinitesimal distance away – an idealization used here to avoid incorporating the force in the system's boundary conditions), defined by

$$Q_u = F_1(t)\delta(s-l), \tag{4.14}$$

where δ represent the Dirac delta function, results in an approximate Lagrange multiplier given by

$$\begin{aligned}\lambda \approx & -Dv'v''' - D\left(v'\right)^2\left(v''\right)^2 - D\left(v'\right)^3 v''' - \frac{1}{2}m\int_l^s \frac{\partial^2}{\partial t^2}\int_0^s \left(v'\right)^2 dsds \\ & - \frac{1}{8}m\int_l^s \frac{\partial^2}{\partial t^2}\int_0^s \left(v'\right)^4 dsds - \frac{1}{4}m\left(v'\right)^2\int_l^s \frac{\partial^2}{\partial t^2}\int_0^s \left(v'\right)^2 dsds \\ & - \int_l^s F_1(t)\delta\left(s-l\right)ds - \frac{1}{2}\left(v'\right)^2\int_l^s F_1(t)\delta\left(s-l\right)ds \\ & - \frac{3}{8}\left(v'\right)^4\int_l^s F_1(t)\delta\left(s-l\right)ds.\end{aligned} \tag{4.15}$$

Substituting this value back into Equation (4.6), defining the specific mass m and the flexural stiffness D according to

$$m = \rho A, \qquad D = EI, \tag{4.16}$$

where ρ, A, E, and I represent the device's mass density, cross-sectional area, Modulus of Elasticity, and cross-sectional moment of inertia, respectively, and further assuming that the transverse non-conservative force is given by

$$Q_v = F_2(t)\delta(s-l) - c\dot{v}, \tag{4.17}$$

where c represents the specific viscous damping coefficient, results in a fifth-order approximation of the system's equation of motion:

$$\begin{aligned}
&\rho A\frac{\partial^2 v}{\partial t^2} + c\frac{\partial v}{\partial t} + EI\frac{\partial^4 v}{\partial s^4} + EI\left(\frac{\partial^2 v}{\partial s^2}\right)^3 + 4EI\left(\frac{\partial v}{\partial s}\right)\left(\frac{\partial^2 v}{\partial s^2}\right)\left(\frac{\partial^3 v}{\partial s^3}\right) \\
&\quad + 6EI\left(\frac{\partial v}{\partial s}\right)^2\left(\frac{\partial^2 v}{\partial s^2}\right)^3 + 8EI\left(\frac{\partial v}{\partial s}\right)^3\left(\frac{\partial^2 v}{\partial s^2}\right)\left(\frac{\partial^3 v}{\partial s^3}\right) \\
&\quad + EI\left(\frac{\partial v}{\partial s}\right)^2\left(\frac{\partial^4 v}{\partial s^4}\right) + EI\left(\frac{\partial v}{\partial s}\right)^4\left(\frac{\partial^4 v}{\partial s^4}\right) \\
&\quad + \frac{1}{2}\rho A\frac{\partial^2 v}{\partial s^2}\int_l^s \frac{\partial^2}{\partial t^2}\int_0^s \left(\frac{\partial v}{\partial s}\right)^2 dsds \\
&\quad + \frac{1}{2}\rho A\frac{\partial v}{\partial s}\int_0^s \frac{\partial^2}{\partial t^2}\left(\frac{\partial v}{\partial s}\right)^2 ds + \frac{\partial^2 v}{\partial s^2}\int_l^s F_1(t)\delta\left(s-l\right) ds \\
&\quad + \frac{1}{8}\rho A\frac{\partial^2 v}{\partial s^2}\int_l^s \frac{\partial^2}{\partial t^2}\int_0^s \left(\frac{\partial v}{\partial s}\right)^4 dsds \\
&\quad + \frac{1}{8}\rho A\frac{\partial v}{\partial s}\int_0^s \frac{\partial^2}{\partial t^2}\left(\frac{\partial v}{\partial s}\right)^4 ds \\
&\quad + \frac{3}{4}\rho A\left(\frac{\partial v}{\partial s}\right)^2\left(\frac{\partial^2 v}{\partial s^2}\right)\int_l^s \frac{\partial^2}{\partial t^2}\int_0^s \left(\frac{\partial v}{\partial s}\right)^2 dsds \\
&\quad + \frac{1}{4}\rho A\left(\frac{\partial v}{\partial s}\right)^3\int_0^s \frac{\partial^2}{\partial t^2}\left(\frac{\partial v}{\partial s}\right)^2 ds \\
&\quad + \frac{3}{2}\left(\frac{\partial v}{\partial s}\right)^2\left(\frac{\partial^2 v}{\partial s^2}\right)\int_l^s F_1(t)\delta\left(s-l\right) ds \\
&\quad + \frac{15}{8}\left(\frac{\partial v}{\partial s}\right)^4\left(\frac{\partial^2 v}{\partial s^2}\right)\int_l^s F_1(t)\delta\left(s-l\right) ds \\
&\quad = F_2(t)\delta\left(s-l\right).
\end{aligned} \tag{4.18}$$

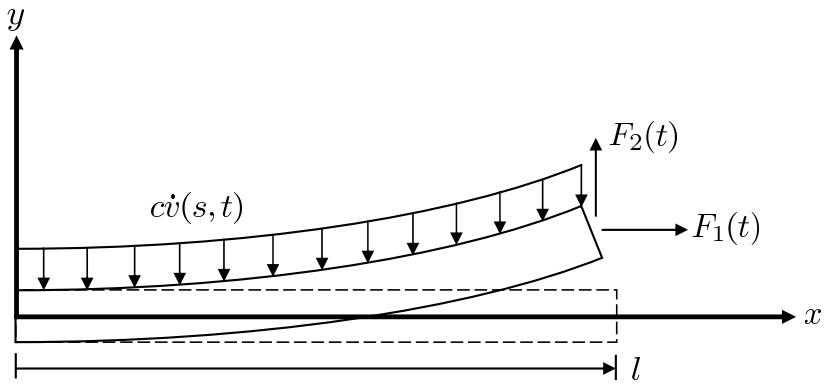

Figure 4.2. Schematic of the beam with non-conservative force contributions.

To reduce the number of free parameters in Equation (4.18), a consistent scaling of the displacement and time variables is introduced. Specifically, the vertical displacement v and the arc length variable s are scaled by a characteristic displacement of the system v_0 (e.g. the beam's thickness or width) and undeformed length l, respectively, according to

$$\hat{v} = \frac{v}{v_0}, \qquad \hat{s} = \frac{s}{l}, \tag{4.19}$$

and time is scaled by a characteristic period of the system T according to

$$\hat{t} = \frac{t}{T}, \tag{4.20}$$

where

$$T = \sqrt{\frac{\rho A l^4}{EI}}. \tag{4.21}$$

Introducing a new nondimensional damping coefficient $\hat{c}$, defined by

$$\hat{c} = \frac{cT}{\rho A}, \tag{4.22}$$

and invoking the Dirac delta identity

$$\delta(ax) = \frac{1}{a}\delta(x), \qquad a > 0 \tag{4.23}$$

reveals a scaled, distributed-parameter model for the system given by

$$\begin{aligned}
&\frac{\partial^2\hat{v}}{\partial\hat{t}^2}+\hat{c}\frac{\partial\hat{v}}{\partial\hat{t}}+\frac{\partial^4\hat{v}}{\partial\hat{s}^4}+\frac{v_0^2}{l^2}\left(\frac{\partial^2\hat{v}}{\partial\hat{s}^2}\right)^3+4\frac{v_0^2}{l^2}\left(\frac{\partial\hat{v}}{\partial\hat{s}}\right)\left(\frac{\partial^2\hat{v}}{\partial\hat{s}^2}\right)\left(\frac{\partial^3\hat{v}}{\partial\hat{s}^3}\right)\\
&\quad+\frac{v_0^2}{l^2}\left(\frac{\partial\hat{v}}{\partial\hat{s}}\right)^2\left(\frac{\partial^4\hat{v}}{\partial\hat{s}^4}\right)+\frac{v_0^2}{2l^2}\frac{\partial\hat{v}}{\partial\hat{s}}\int_0^{\hat{s}}\frac{\partial^2}{\partial\hat{t}^2}\left(\frac{\partial\hat{v}}{\partial\hat{s}}\right)^2d\hat{s}\\
&\quad+\frac{v_0^2}{2l^2}\frac{\partial^2\hat{v}}{\partial\hat{s}^2}\int_1^{\hat{s}}\frac{\partial^2}{\partial\hat{t}^2}\int_0^{\hat{s}}\left(\frac{\partial\hat{v}}{\partial\hat{s}}\right)^2d\hat{s}d\hat{s}+\frac{l^2}{EI}\frac{\partial^2\hat{v}}{\partial\hat{s}^2}\int_1^{\hat{s}}F_1(t)\delta\left(\hat{s}-1\right)d\hat{s}\\
&\quad+6\frac{v_0^4}{l^4}\left(\frac{\partial\hat{v}}{\partial\hat{s}}\right)^2\left(\frac{\partial^2\hat{v}}{\partial\hat{s}^2}\right)^3+8\frac{v_0^4}{l^4}\left(\frac{\partial\hat{v}}{\partial\hat{s}}\right)^3\left(\frac{\partial^2\hat{v}}{\partial\hat{s}^2}\right)\left(\frac{\partial^3\hat{v}}{\partial\hat{s}^3}\right)\\
&\quad+\frac{v_0^4}{l^4}\left(\frac{\partial\hat{v}}{\partial\hat{s}}\right)^4\left(\frac{\partial^4\hat{v}}{\partial\hat{s}^4}\right)+\frac{v_0^4}{8l^4}\frac{\partial^2\hat{v}}{\partial\hat{s}^2}\int_1^{\hat{s}}\frac{\partial^2}{\partial\hat{t}^2}\int_0^{\hat{s}}\left(\frac{\partial\hat{v}}{\partial\hat{s}}\right)^4d\hat{s}d\hat{s}\\
&\quad+\frac{v_0^4}{8l^4}\frac{\partial\hat{v}}{\partial\hat{s}}\int_0^{\hat{s}}\frac{\partial^2}{\partial\hat{t}^2}\left(\frac{\partial\hat{v}}{\partial\hat{s}}\right)^4d\hat{s}+\frac{v_0^4}{4l^4}\left(\frac{\partial\hat{v}}{\partial\hat{s}}\right)^3\int_0^{\hat{s}}\frac{\partial^2}{\partial\hat{t}^2}\left(\frac{\partial\hat{v}}{\partial\hat{s}}\right)^2d\hat{s}\\
&\quad+\frac{3v_0^4}{4l^4}\left(\frac{\partial\hat{v}}{\partial\hat{s}}\right)^2\left(\frac{\partial^2\hat{v}}{\partial\hat{s}^2}\right)\int_1^{\hat{s}}\frac{\partial^2}{\partial\hat{t}^2}\int_0^{\hat{s}}\left(\frac{\partial\hat{v}}{\partial\hat{s}}\right)^2d\hat{s}d\hat{s}\\
&\quad+\frac{3v_0^2}{2EI}\left(\frac{\partial\hat{v}}{\partial\hat{s}}\right)^2\left(\frac{\partial^2\hat{v}}{\partial\hat{s}^2}\right)\int_1^{\hat{s}}F_1(t)\delta\left(\hat{s}-1\right)d\hat{s}\\
&\quad+\frac{15v_0^4}{8EIl^2}\left(\frac{\partial\hat{v}}{\partial\hat{s}}\right)^4\left(\frac{\partial^2\hat{v}}{\partial\hat{s}^2}\right)\int_1^{\hat{s}}F_1(t)\delta\left(\hat{s}-1\right)d\hat{s}\\
&\quad=\frac{F_2(t)l^3}{v_0EI}\delta\left(\hat{s}-1\right).
\end{aligned}\tag{4.24}$$

Though, theoretically, the behavior of the system can be directly recovered from this equation of motion, the practicality of this approach is questionable. As such, the model presented in Equation (4.24) is used to develop a consistent lumped-mass model, which is amenable to analysis.

4.2 Formulation of a Lumped-Mass Model

To facilitate nonlinear analysis and ultimately predictive design, the governing partial differential equation presented in Equation (4.24) can be reduced to a system of nonlinear ordinary differential equations using modal projection. Specifically, the dynamic variable $\hat{v}(\hat{s},\hat{t})$ can be expanded using the system's mode shapes $\Psi_i(\hat{s})$ ac-

cording to

$$\hat{v}(\hat{s},\hat{t}) = \sum_{i=1}^{\infty} w_i(\hat{t})\Psi_i(\hat{s}). \tag{4.25}$$

Given the dominance of first mode behavior in the experimental studies completed to date, a truncated, single-mode expansion proves sufficient for analysis, namely,

$$\hat{v}(\hat{s},\hat{t}) = w(\hat{t})\Psi(\hat{s}). \tag{4.26}$$

As the system's non-conservative forces and nonlinearities are subsequently assumed to be 'small' and, in practice, lead to minimal distortion of the system's mode shapes, the first assumed mode can be recovered from the linear differential equation

$$\Psi^{iv} - w^2\Psi = 0, \tag{4.27}$$

with boundary conditions

$$\Psi(0) = 0, \qquad \Psi'(0) = 0, \qquad \Psi''(1) = 0, \qquad \Psi'''(1) = 0. \tag{4.28}$$

Though additional mode shapes and/or mode shapes accounting for the applied axial load $F_1(t)$ could be included in the above expansion to increase the accuracy of the lumped-mass model, the slight improvement that results is largely negated by the added complexity of the analysis, as well as the general uncertainty associated with resonant microsystems.

Prior to the final derivation of the EMA microbeam's lumped-mass model, it also proves convenient to expand the system's applied non-conservative forces in terms of physical parameters. As these forces (apart from a small contribution arising from viscous damping) result from the interaction between an external permanent magnet and a current loop integrated into the microbeam oscillator, they can be approximated using the Lorentz force model

$$\vec{F}(t) = i(t)\int d\vec{l}\times\vec{B}, \tag{4.29}$$

where $i(t)$, $d\vec{l}$, and $\vec{B}$ represent the current passing through the integrated loop, the length of a differential element of the loop, and the magnetic field, respectively. Assuming a two harmonic AC drive current with an additional DC component (which could be used for frequency tuning) this results in a non-conservative force model of the form

$$\begin{aligned}\vec{F}(t) &= F_1(t)\mathbf{i} + F_2(t)\mathbf{j} \\ &= \left(i_{DC} + i_1 \cos\omega t + i_2 \cos 2\omega t\right) gB \left(\cos\alpha\mathbf{i} + \sin\alpha\mathbf{j}\right),\end{aligned} \tag{4.30}$$

where g represents the width of current loop and α specifies the orientation of the magnetic field (assumed to be uniform and unidirectional) with respect to a vertical reference (measured in the counterclockwise direction). Introducing this model, as well as the state variable expansion detailed above, into Equation (4.24) and projecting the resulting equation back onto the first mode through the use of an inner product operator results in the final, lumped-mass equation of motion for the system given by

$$\begin{aligned}&z'' + 2\varepsilon\zeta z' + \left(1 + \varepsilon\lambda_1 \cos\Omega\tau + \varepsilon\gamma_1 \cos 2\Omega\tau\right) z \\ &\quad + \left(\varepsilon\chi_3 + \varepsilon\lambda_3 \cos\Omega\tau + \varepsilon\gamma_3 \cos 2\Omega\tau\right) z^3 + \varepsilon\beta\left(z'^2 z + z^2 z''\right) \\ &\quad + \left(\varepsilon\chi_5 + \varepsilon\lambda_5 \cos\Omega\tau + \varepsilon\gamma_5 \cos 2\Omega\tau\right) z^5 + \varepsilon\nu_1 z^3 z'^2 + \varepsilon\nu_2 z^4 z'' \\ &\quad = \varepsilon\eta_0 + \varepsilon\eta_1 \cos\Omega\tau + \varepsilon\eta_2 \cos 2\Omega\tau.\end{aligned} \tag{4.31}$$

System parameters that appear in this equation are defined in Appendix A.

4.3 Induced Electromotive Force

While the equation of motion detailed above adequately characterizes the current-input/displacement-output behavior of the system of interest, it fails to characterize how the acquired displacement is converted back into an electrical signal. Given that the principal motivation for utilizing magnetomotive transduction is that a response-dependent electromotive force (emf) can be readily obtained from a given device, it is

prudent to proceed with the derivation of the exact relationship that exists between the system's dynamic response and the induced emf voltage. This relationship is obtained here through a direct application of Faraday's Law [200, 201].

Noting that the magnetic flux $\Phi(t)$ through a surface is given by

$$\Phi(t) = \int\int_S (\vec{B} \cdot \hat{n}) dS, \tag{4.32}$$

where $\hat{n}$ represents a unit vector normal to the enclosed surface and dS represents a differential area element on the surface, the flux passing through a given microbeam resonator can be shown to be

$$\Phi(t) = \int\int_S B \sin\alpha \sin\psi dS + \int\int_S B \cos\alpha \cos\psi dS, \tag{4.33}$$

where B, α, and ψ are defined as above. Expanding this flux in terms of the angle ψ, substituting as appropriate, and truncating the result yields an approximate flux given by

$$\Phi(t) \approx Bg \sin\alpha \int_0^l v' ds + Bg \cos\alpha \int_0^l \left(1 - \frac{v'^2}{2} - \frac{v'^4}{8}\right) ds. \tag{4.34}$$

Substituting the nondimensional parameters detailed in Section 4.1 into this expression and projecting the result onto the system's first mode shape Ψ, results in a 'lumped-mass' approximation for the flux:

$$\begin{aligned} \Phi(\hat{t}) =& Bg \sin\alpha v_0 \int_0^1 \Psi \int_0^1 \Psi' d\hat{s} d\hat{s} z + Bg \cos\alpha l \int_0^1 \Psi d\hat{s} \\ &+ \frac{Bg \cos\alpha v_0^2}{2l} \int_0^1 \Psi \int_0^1 \Psi'^2 d\hat{s} d\hat{s} z^2 + \frac{Bg \cos\alpha v_0^4}{8l^3} \int_0^1 \Psi \int_0^1 \Psi'^4 d\hat{s} d\hat{s} z^4. \end{aligned} \tag{4.35}$$

The induced emf can be directly recovered from this approximation through the use of Faraday's Law, namely,

$$V_{emf} = -\frac{\partial \Phi(t)}{\partial t} = -\frac{\partial \Phi(t)}{\partial \hat{t}} \frac{\partial \hat{t}}{\partial t}. \tag{4.36}$$

This results in a closed-form expression for the induced emf, which is given by

$$V_{emf} = \kappa_1 \dot{z} + \kappa_2 z \dot{z} + \kappa_4 z^3 \dot{z}, \tag{4.37}$$

where

$$\kappa_1 = -\frac{Bg\sin\alpha v_0}{T}\int_0^1 \Psi \int_0^1 \Psi' d\hat{s}d\hat{s},$$
$$\kappa_2 = -\frac{Bg\cos\alpha v_0^2}{lT}\int_0^1 \Psi \int_0^1 \Psi'^2 d\hat{s}d\hat{s}, \tag{4.38}$$
$$\kappa_4 = -\frac{Bg\cos\alpha v_0^4}{2l^3T}\int_0^1 \Psi \int_0^1 \Psi'^4 d\hat{s}d\hat{s}.$$

Brief examination of Equation (4.37) reveals a handful of noteworthy characteristics. First, if the external magnetic field is oriented vertically (i.e. $\alpha = 0^\circ$), the induced emf has a purely-nonlinear dependence on the system's dynamic response. Likewise, if the external magnetic field is oriented horizontally (i.e. $\alpha = 90^\circ$), the induced emf is directly proportional the system's velocity. Intermediate orientations, unfortunately, feature a relatively complex emf/dynamic response relationship. Depending on the exact orientation and geometry of interest, this may hinder emf-based measurement readout. Ongoing experimentation utilizing and comparing both induced-emf and laser vibrometry outputs are aimed at rectifying some of the issues associated with the measurement readout of systems with arbitrary field orientations.

CHAPTER 5

Electromagnetically-Actuated Microbeam Resonators: Nonlinear Behavior

Though the equation of motion detailed in the previous chapter, Equation (4.31), is similar in form to those previously considered by the author in References [105–107], the nonlinear, parametrically-excited system must be revisited here due to the addition of fifth-order nonlinearities (which, as previously noted, are required to fully explain all of the system behaviors recorded to date). As this represents a nontrivial extension of prior work, the analysis contained herein begins anew, despite a partial overlap with the work detailed in References [106, 107].

5.1 Derivation of the System's Averaged Equations

Given that systems with purely-parametric excitations are likely to have the most desirable nonlinear frequency response characteristics, especially for applications akin to resonant mass sensing, the present investigation focuses on resonator configurations in which the magnetic field is oriented in the vertical direction (i.e. $\alpha = 0^{\circ}$). This special case eliminates the direct forcing terms which appear in the system's equation of motion (i.e., $\eta_i = 0$, $i = 0, 1, 2$), due to their dependence on $\sin\alpha$. Additionally, for the sake of analysis, all nonlinear, forcing, and damping parameters which appear in the parametrically-excited system's equation of motion are subsequently assumed

to be 'small' (as denoted by the presence of the book-keeping parameter ε). This assumption, which is typically valid for MEMS resonators operating in lightly-damped environments (see, for example, Reference [107]), greatly simplifies analysis.

Due to the highly-nonlinear nature of Equation (4.31), a standard perturbation technique, the method of averaging, is utilized for analysis. To facilitate this approach, a constrained coordinate change is first introduced into Equation (4.31):

$$z(\tau) = a(\tau)\cos\left[\Omega\tau + \psi(\tau)\right], \tag{5.1}$$

$$z'(\tau) = -a(\tau)\Omega\sin\left[\Omega\tau + \psi(\tau)\right]. \tag{5.2}$$

In addition, to capture the system's near-resonant behavior, a frequency detuning parameter σ is introduced, which is given by

$$\sigma = \frac{\Omega - 1}{\varepsilon}. \tag{5.3}$$

Substituting each of these expressions into Equation (4.31), separating the resulting equation and the constraint equation in terms of amplitude and phase, and averaging each over one period of the oscillator's response ($2\pi/\Omega$) yields the 'slow-flow' equations that govern the system's behavior. To order ε, these averaged equations are given by

$$a' = \frac{1}{64}a\varepsilon\left[-64\zeta + \left(16\gamma_1 + 8\gamma_3 a^2 + 5\gamma_5 a^4\right)\sin 2\psi\right] + \mathcal{O}(\varepsilon^2), \tag{5.4}$$

$$\begin{aligned}\psi' = \frac{1}{64}\varepsilon\Big[&8a^2\left(3\chi_3 - 2\beta\right) + 4a^4\left(5\chi_5 + \nu_1 - 5\nu_2\right) - 64\sigma \\ &+ \left(16\left(\gamma_1 + a^2\gamma_3\right) + 15a^4\gamma_5\right)\cos 2\psi\Big] + \mathcal{O}(\varepsilon^2).\end{aligned} \tag{5.5}$$

For reference purposes, note that higher-order perturbation methods, though traditionally utilized for systems with higher-order nonlinearities, have not been utilized here due to the nature of the system's scaling, which was carefully chosen to ensure that the net electromagnetic force appeared at $\mathcal{O}(\varepsilon)$ without the use of amplitude expansions. This approach, though slightly unconventional, was justified experimentally in Reference [107], amongst others.

5.2 Steady-State System Behaviors

With the averaged equations detailed above in hand, the system's steady-state behavior can be recovered by setting the left hand sides of Equations (5.4) and (5.5) equal to zero and solving for the steady-state amplitudes and phases. Given that the system's nonlinear behavior is of principal interest here and that this behavior is largely unaffected by damping, damping is assumed to be negligible (i.e. $\zeta = 0$). Readers interested in the effects of small damping are referred to Reference [107].

Setting $(a', \psi') = (0, 0)$ reveals that the EMA microresonator has a trivial solution (with indeterminant phase) and four pairs of physically-realizable, nontrivial solutions given, in terms of amplitude and phase, by

$$\bar{a}_1 = \pm 2\sqrt{\frac{-\nu_{3,1} + \sqrt{{\nu_{3,1}}^2 - \nu_{5,1}(\gamma_1 - 4\sigma)}}{\nu_{5,1}}}, \qquad \bar{\psi}_1 = 0, \tag{5.6}$$

$$\bar{a}_2 = \pm 2\sqrt{\frac{-\nu_{3,1} - \sqrt{{\nu_{3,1}}^2 - \nu_{5,1}(\gamma_1 - 4\sigma)}}{\nu_{5,1}}}, \qquad \bar{\psi}_2 = 0, \tag{5.7}$$

$$\bar{a}_3 = \pm 2\sqrt{\frac{-\nu_{3,2} + \sqrt{{\nu_{3,2}}^2 + \nu_{5,2}(\gamma_1 + 4\sigma)}}{\nu_{5,2}}}, \qquad \bar{\psi}_3 = \frac{\pi}{2}, \tag{5.8}$$

$$\bar{a}_4 = \pm 2\sqrt{\frac{-\nu_{3,2} - \sqrt{{\nu_{3,2}}^2 + \nu_{5,2}(\gamma_1 + 4\sigma)}}{\nu_{5,2}}}, \qquad \bar{\psi}_4 = \frac{\pi}{2}. \tag{5.9}$$

Note that each $\pm$ pair of these solutions, as well as solutions with magnitude π phase shifts, represent the same physical response. Furthermore, note that here and throughout the remaining portions of this chapter, ρ_3 and ρ_5 are used to represent the system's third- and fifth-order mechanical nonlinearities (incorporating inertial terms), given by

$$\rho_3 = 3\chi_3 - 2\beta, \qquad \rho_5 = 5\chi_5 + \nu_1 - 5\nu_2, \tag{5.10}$$

and $\nu_{3,1}$, $\nu_{3,2}$, $\nu_{5,1}$, and $\nu_{5,2}$ are used to represent the system's third- and fifth-order

effective nonlinearities, which are given by

$$\nu_{3,1} = \rho_3 + 2\gamma_3, \qquad \nu_{3,2} = \rho_3 - 2\gamma_3, \tag{5.11}$$

$$\nu_{5,1} = 4\rho_5 + 15\gamma_5, \qquad \nu_{5,2} = 4\rho_5 - 15\gamma_5. \tag{5.12}$$

Each of these parameters prove critical in characterizing the system's steady-state behavior.

Though not directly pertinent to the present study, it is also worth noting that under certain conditions the system examined herein can feature two additional constant-amplitude solution pairs of amplitude

$$\bar{a}_5 = \pm\frac{2}{\sqrt{5}}\sqrt{\frac{-\gamma_3 + \sqrt{\gamma_3^2 - 5\gamma_1\gamma_5}}{\gamma_5}}, \tag{5.13}$$

$$\bar{a}_6 = \pm\frac{2}{\sqrt{5}}\sqrt{\frac{-\gamma_3 - \sqrt{\gamma_3^2 - 5\gamma_1\gamma_5}}{\gamma_5}}. \tag{5.14}$$

As these solutions are not realizable with current device designs, further discussion is omitted. It should be noted, however, that the inclusion of alternative transduction mechanisms and/or the use of nonuniform beam geometries could potentially lead to the emergence of these solutions (see, for example, the electrostatically-actuated, comb-driven devices detailed in Reference [107]). As this, in turn, could lead to detrimental changes in the system's qualitative behavior, care must be taken to avoid these solutions in the course of design.

Before proceeding with a thorough examination of the system's qualitative behavior and its dependence on the third- and fifth-order effective nonlinearities detailed above, it is prudent to briefly analyze the stability of the system's steady-state solutions. For present purposes, the local stability of the system's response can be determined by considering the linear behavior of the system's averaged equations near each of the aforementioned steady-state solutions.

Defining a composite state vector $X(\tau)$ according to

$$X(\tau) = \begin{bmatrix} a(\tau) \\ \psi(\tau) \end{bmatrix} \tag{5.15}$$

and a composite steady-state solution vector $\bar{X}$ according to

$$\bar{X} = \begin{bmatrix} \bar{a} \\ \bar{\psi} \end{bmatrix}, \tag{5.16}$$

the local, linearized equation of motion for the system can be rewritten as

$$Y'(\tau) = J(\bar{X})Y(\tau), \tag{5.17}$$

where $Y(\tau)$ represents the state vector's deviation from the steady state, namely,

$$Y(\tau) = X(\tau) - \bar{X}, \tag{5.18}$$

and J represents the Jacobian matrix of the averaged equations evaluated at the steady state. Using Equation (5.17), the stability of the various responses can be directly deduced by computing the eigenvalues of the Jacobian J at the respective steady-state.

To simplify stability analysis, the system's eigenvalues can be characterized using the trace and determinant of the 2×2 Jacobian detailed above [202]. Specifically, the eigenvalues can be expressed in terms of the trace, T, and the determinant, Δ, as

$$\Lambda_{1,2} = \frac{1}{2}\left(T \pm \sqrt{T^2 - 4\Delta}\right). \tag{5.19}$$

For the undamped case under consideration here, the trace of the Jacobian for each of the steady-state responses is zero ($T = 0$), and thus for nontrivial eigenvalues only two generic equilibrium types are possible: saddles (unstable) and centers (marginally stable). As such, the type of equilibrium that exists depends solely on the sign of the determinant Δ. Specifically, when $\Delta > 0$ the equilibrium is a center, and when

$\Delta < 0$ the equilibrium is a saddle. The remaining case, $\Delta = 0$, corresponds to the degenerate case of two identically zero eigenvalues, and, as such, is used here only to identify where changes in stability occur.

Utilizing the criteria outlined above, the stability of the five solutions of interest (the trivial solution and the four physically-consistent solution pairs) can be determined. In particular, it can be shown (with a conversion to Cartesian coordinates) that the trivial solution exists as a saddle point for all frequencies (detuning values) between σ_1 and σ_2, where

$$\sigma_{1,2} = \pm\frac{\gamma_1}{4}, \tag{5.20}$$

and as a center elsewhere. Similarly, a_1 and a_2 can be shown to have critical detuning values of σ_1 and σ_3, where

$$\sigma_3 = \frac{-{\nu_{3,1}}^2}{4\nu_{5,1}} + \frac{\gamma_1}{4}, \tag{5.21}$$

and a_3 and a_4 can be shown to have critical detuning values of σ_2 and σ_4, where

$$\sigma_4 = \frac{-{\nu_{3,2}}^2}{4\nu_{5,2}} - \frac{\gamma_1}{4}. \tag{5.22}$$

As each of these critical detuning values, as well as the sign of the Jacobian's determinant in between, is dependent on numerous system parameters, a number of distinct stability configurations exist. Rather than delineating each of these configurations here, the cases are detailed below as part of an examination of the system's frequency response.

5.3 Nonlinear Frequency Response Structures

As evident from Equations (5.6)-(5.9), the qualitative behavior of the system detailed herein is not dependent on a single effective nonlinearity, but rather a set of effective nonlinearities, which collectively dictate the nature of the system response. In Chapter 3 and Reference [107], the author examined similar behavior in the context of a third-order, parametrically-excited system using a simple, nonlinear parameter space

investigation. Though a similar approach is adopted here, the addition of fifth-order nonlinearities requires a hierarchical analysis.

Generally speaking, the third-order effective nonlinearities detailed in Equation (5.11) dictate the system's nontrivial behavior in the vicinity of the pitchfork bifurcations that occur at σ_1 and σ_2. In particular, selecting system parameters such that $\nu_{3,1} > 0$ and $\nu_{3,2} > 0$ results in a frequency response structure with third-order hardening characteristics and selecting $\nu_{3,1} < 0$ and $\nu_{3,2} < 0$ results in a frequency response structure with third-order softening characteristics. Clearly, under certain conditions, $\nu_{3,1}$ and $\nu_{3,2}$ can be selected to have opposite signs. Under these conditions the system exhibits 'mixed' nonlinear characteristics, wherein the response curves initially bend away from one another. (Note that in certain, physically-inconsistent cases these curves bend toward one another. The response is significantly more complicated in these cases, however, as one or more constant amplitude solutions also exist.)

To summarize the results outlined above, it proves convenient to utilize the upper half-plane of third-order nonlinear parameter space shown in Figure 5.1a, as identifying the oscillator's location within this parameter space allows for the rapid prediction of the system's qualitative behavior (at least to third-order). (Note that as detailed in Section 5.4, the EMA microbeam resonators detailed herein are not expected to operate in the lower half-plane of the parameter space, wherein the previously-detailed, constant-amplitude solutions exist.) For example, noting that an unforced system initially lies on the positive portion of the ρ_3 axis reveals that the resonator, in the absence of excitation, exhibits third-order hardening characteristics. This position is not fixed, however, as adding an effective AC excitation allows the oscillator's location in the third-order parameter space to translate in the vertical direction, thus allowing the system's third-order behavior to transition to a mixed response. Likewise, adding an effective DC excitation allows the oscillator's location to translate in the horizontal direction, thus facilitating transitions to softening or mixed third-order responses.

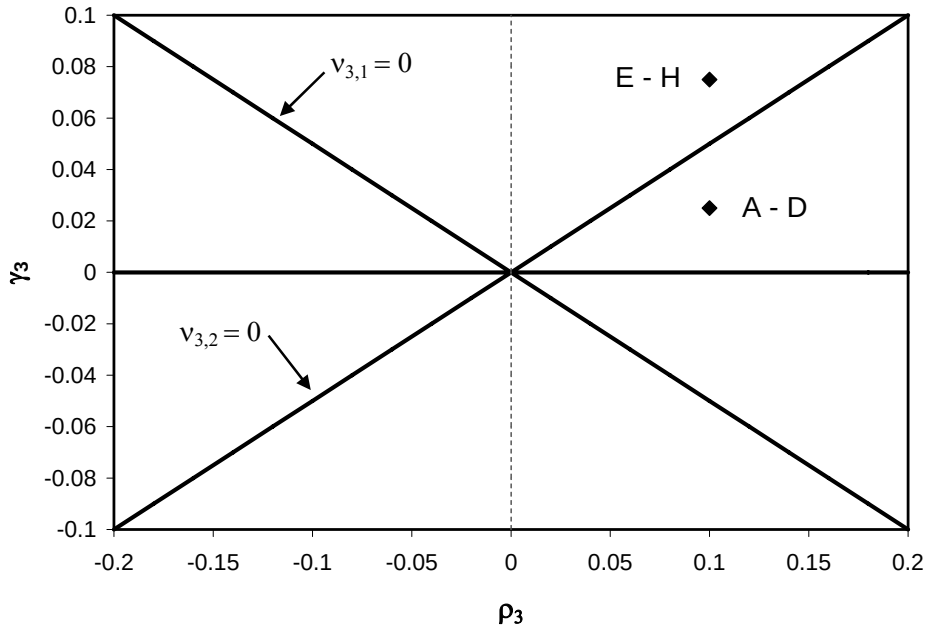

(a)

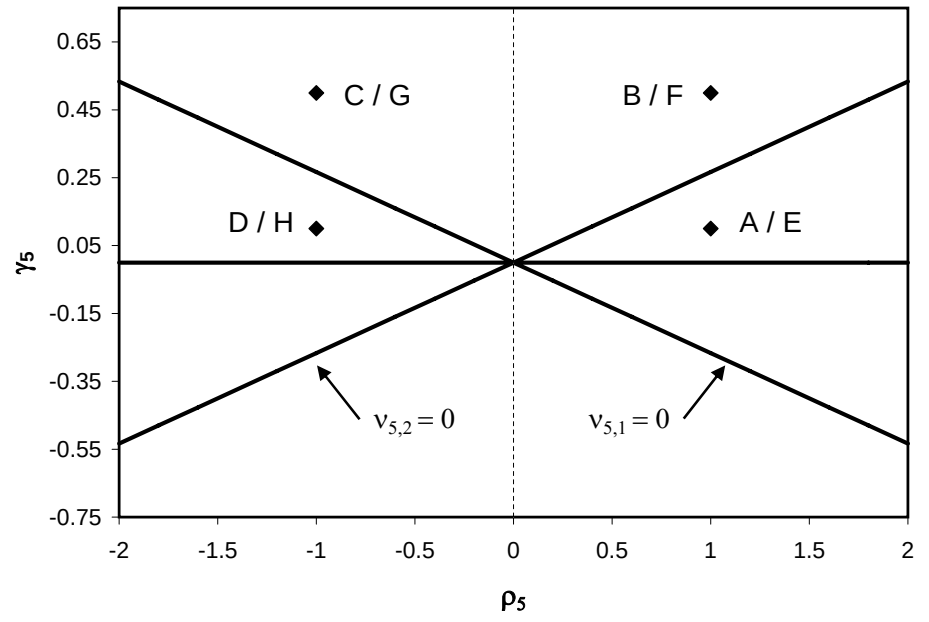

(b)

Figure 5.1. (a) Third- and (b) fifth-order nonlinear parameter spaces corresponding to the system detailed in Equation (4.31). Note that the labeled data points correspond to the various cases delineated in Table 5.1, as well as the frequency response plots shown in Figures 5.2-5.9.

While the resonator's third-order nonlinearities dictate the immediate post-pitchfork-bifurcation behavior of the system, the fifth-order effective nonlinearities dictate the system's 'global' frequency response behavior (as limited, of course, by the nonlinear model and perturbation technique employed) and facilitate the unfolding of the system's behavior in situations where the system's third-order effective nonlinearities are near zero. In particular, selecting the system parameters such that $\nu_{5,1} > 0$ and $\nu_{5,2} > 0$ results in a frequency response with fifth-order hardening characteristics and selecting $\nu_{5,1} < 0$ and $\nu_{5,2} < 0$ renders a frequency response with fifth-order softening characteristics. Likewise, under certain conditions, $\nu_{5,1}$ and $\nu_{5,2}$ can be selected to have opposite signs. This leads to frequency response structures with 'mixed' nonlinear characteristics, wherein the response curves eventually bend away from one another, potentially leading to globally unbounded responses. (Note that the term 'globally unbounded' is used loosely herein to designate the fact that some initial conditions result in an unbounded response. 'Globally bounded' is used to designate the fact that *all* initial conditions lead to a bounded response.)

As with the third-order nonlinearities, it proves convenient to utilize the upper half-plane of the fifth-order nonlinear parameter space, shown in Figure 5.1b, in order to characterize the qualitative behavior of the system's global frequency response. As the system behavior within this parameter space, as well as its dependence on effective AC and DC excitations, is largely akin to that described above in the context of the system's third-order nonlinearities, further discussion is omitted.

In order to display each of the qualitatively distinct frequency responses that can be recovered for the equation of motion detailed in Equation (4.31), a number of representative cases, detailed in Table 5.1 and by the data points in Figure 5.1, are subsequently considered. Note that while most of these cases are readily obtainable using a given EMA microcantilever design, additional responses have been included for the sake of completeness (largely to assist those working on related problems).

Table 5.1. Parameter values used to produce the frequency response plots shown in Figures 5.2-5.9.

Case	γ_1	ρ_3	γ_3	ρ_5	γ_5
A	0.1	0.1	0.025	1	0.1
B	0.1	0.1	0.025	1	0.5
C	0.1	0.1	0.025	-1	0.5
D	0.1	0.1	0.025	-1	0.1
E	0.1	0.1	0.075	1	0.1
F	0.1	0.1	0.075	1	0.5
G	0.1	0.1	0.075	-1	0.5
H	0.1	0.1	0.075	-1	0.1

Furthermore, note that only those cases in the first quadrant of the third-order parameter space are included. The behavior of oscillators operating in the second quadrant, namely those operating with large, negative, DC tuning biases, can be easily determined through symmetry arguments.

The frequency response plots corresponding to data points A-H in Table 5.1 and Figure 5.1 are included in Figures 5.2-5.9. As the vast majority of these plots include responses that are qualitatively distinct from one another, each is considered in turn.

The frequency response plot shown in Figure 5.2, representative of all systems with $\nu_{3,1} > 0$, $\nu_{3,2} > 0$, $\nu_{5,1} > 0$, and $\nu_{5,2} > 0$ and corresponding to Case A, clearly depicts a classical hardening response. That is, the system's nontrivial response branches both result from pitchfork bifurcations (one supercritical and one subcritical) occurring at σ_1 and σ_2, respectively, and bend to the right, ultimately yielding a globally bounded system response. The response shown in Figure 5.3, representative of all systems with $\nu_{3,1} > 0$, $\nu_{3,2} > 0$, $\nu_{5,1} > 0$, and $\nu_{5,2} < 0$ and corresponding to Case B, is slightly more complicated. Here, the response incorporates all of the features detailed above for Case A, but also an additional saddle-node bifurcation at σ_4. This additional bifurcation point not only leads to a destabilization of the left branch, but also causes the branch to bend to the left yielding a globally unbounded system response. Figure 5.4, corresponding to Case C, depicts a response qualitatively

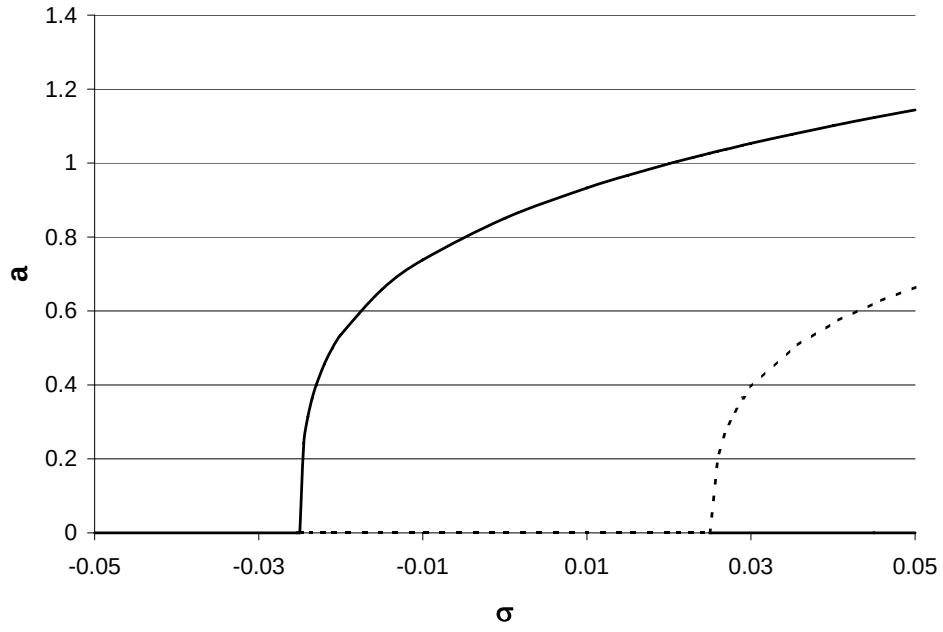

Figure 5.2. Frequency response plot corresponding to Case A. Note that here, and in Figures 5.3-5.12, solid lines are used to indicate a stable response. Likewise, dashed lines are used to indicate an unstable response.

equivalent to that seen in Case B, despite the fact that the sign of ρ_5 has changed. Though counterintuitive, this is consistent with the system's stated dependence on the fifth-order effective nonlinearities, and is thus included only for the sake of completeness. The final frequency response plot realizable for positive values of $\nu_{3,1}$ and $\nu_{3,2}$, designated Case D, is depicted in Figure 5.5. Here, due to the fact that both $\nu_{5,1}$ and $\nu_{5,2}$ are negative, each of the system's nontrivial branches undergo saddle-node bifurcations, at σ_3 and σ_4 respectively, yielding a globally bounded response, wherein both response branches ultimately bend to the left in a softening-like manner.

Figures 5.6-5.9, corresponding to Cases E-H, are representative of systems with mixed third-order nonlinearities, that is systems with $\nu_{3,1} > 0$ and $\nu_{3,2} < 0$. The first response in this series, designated Case E and representative of systems with $\nu_{5,1} > 0$ and $\nu_{5,2} > 0$, is shown in Figure 5.6. Here, as expected, the system has two nontrivial branches – the result of pitchfork bifurcations at σ_1 and σ_2, respectively

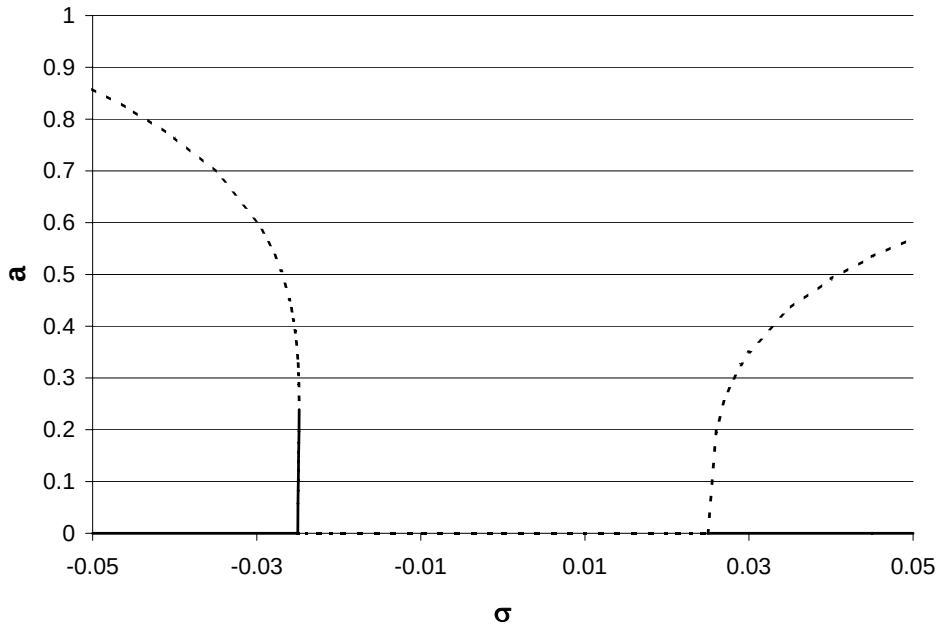

(a)

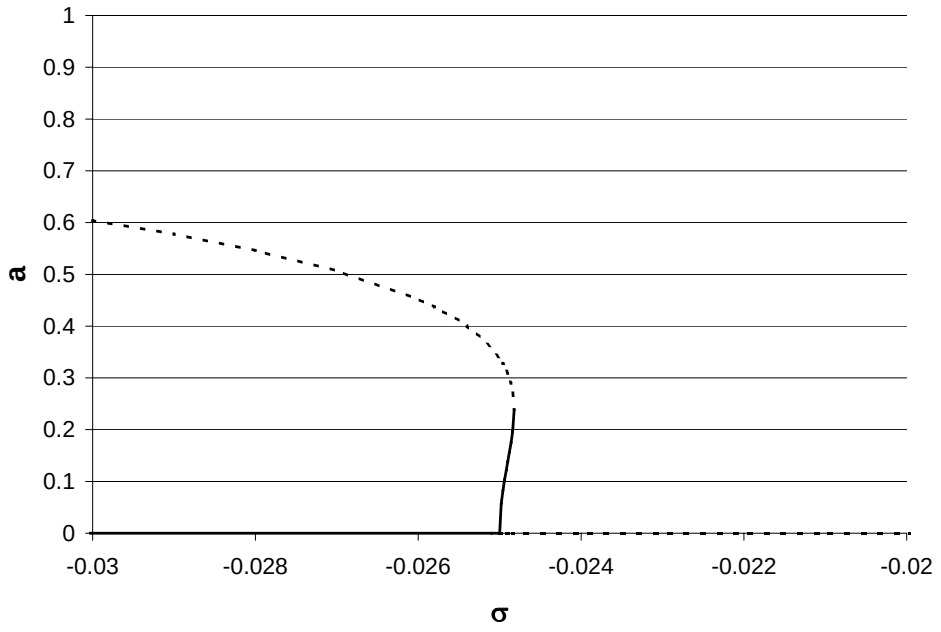

(b)

Figure 5.3. (a) Frequency response plot corresponding to Case B. (b) The system's frequency response in the proximity of $\sigma = -0.025$.

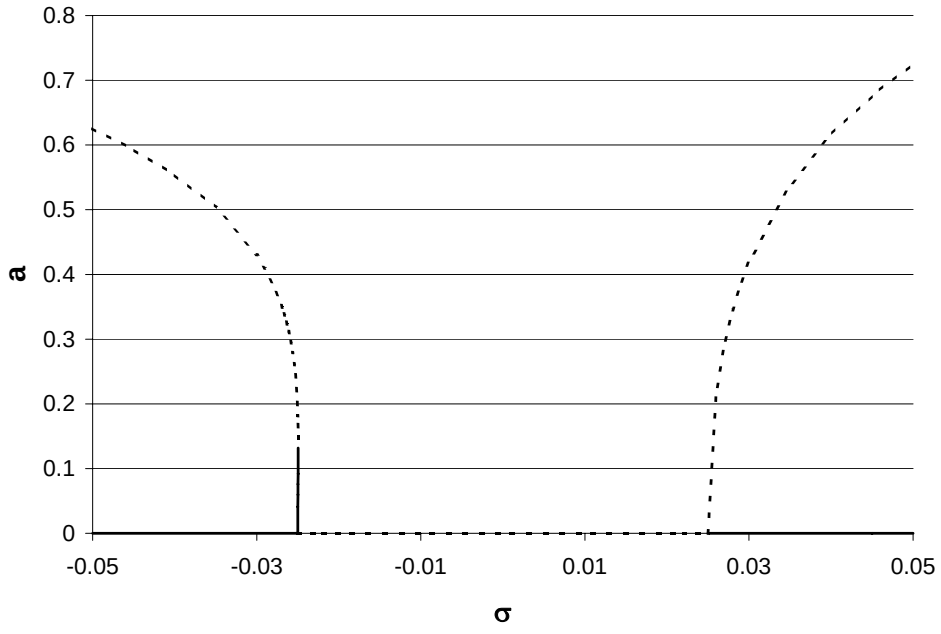

(a)

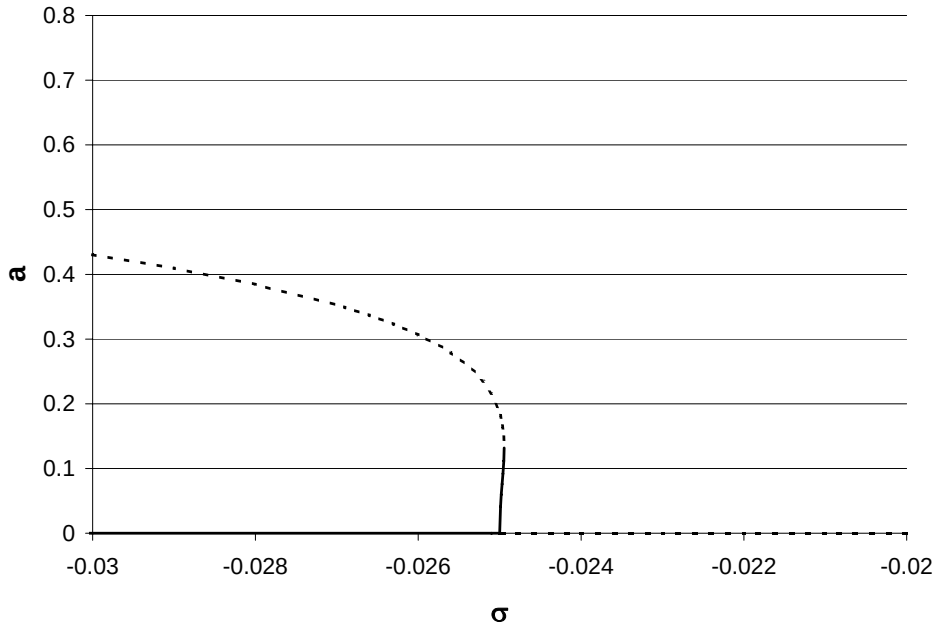

(b)

Figure 5.4. (a) Frequency response plot corresponding to Case C. (b) The system's frequency response in the proximity of $\sigma = -0.025$.

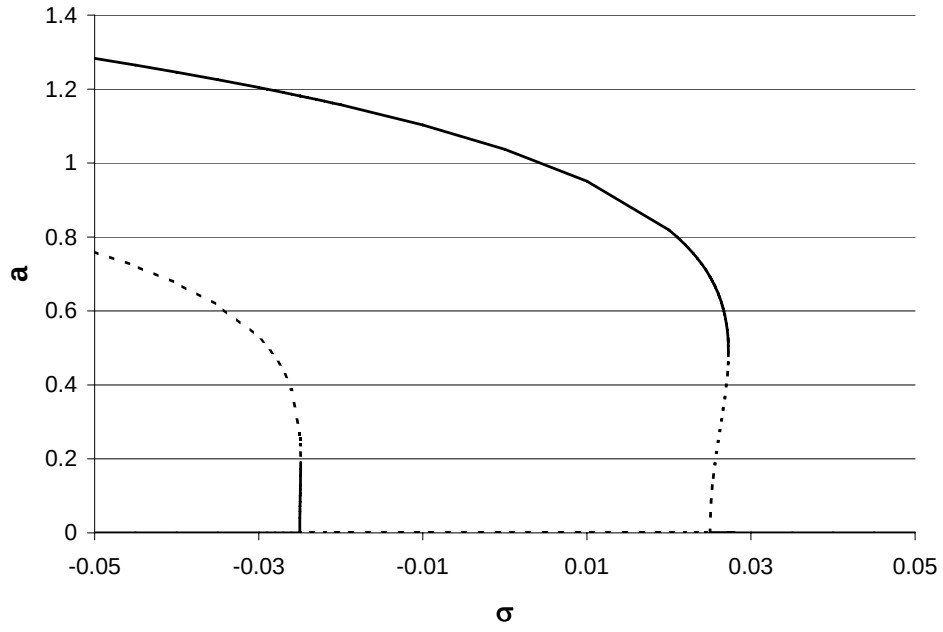

Figure 5.5. Frequency response plot corresponding to Case D.

– that initially bend away from one another. However, in this case, the left branch undergoes a saddle-node bifurcation at σ_4, which not only stabilizes the branch, but also causes it to bend to the right, ultimately yielding a globally stable, hardening-like system response. Figures 5.7 and 5.8, corresponding to Cases F and G, respectively, are representative of systems with $\nu_{5,1} > 0$ and $\nu_{5,2} < 0$. Here, neither of the nontrivial branches undergo additional bifurcations, and thus these branches which initially bend away from each other continue to do so for all values of detuning. The last response in the series, designated Case H and corresponding to systems with $\nu_{5,1} < 0$ and $\nu_{5,2} < 0$ is shown in Figure 5.9. Here, as with all other frequency responses in this series, the responses branches initially bend away from one another. However, at σ_3 the right branch undergoes a saddle-node bifurcation, which not only stabilizes it, but also causes it to bend to the left, yielding a softening-like response.

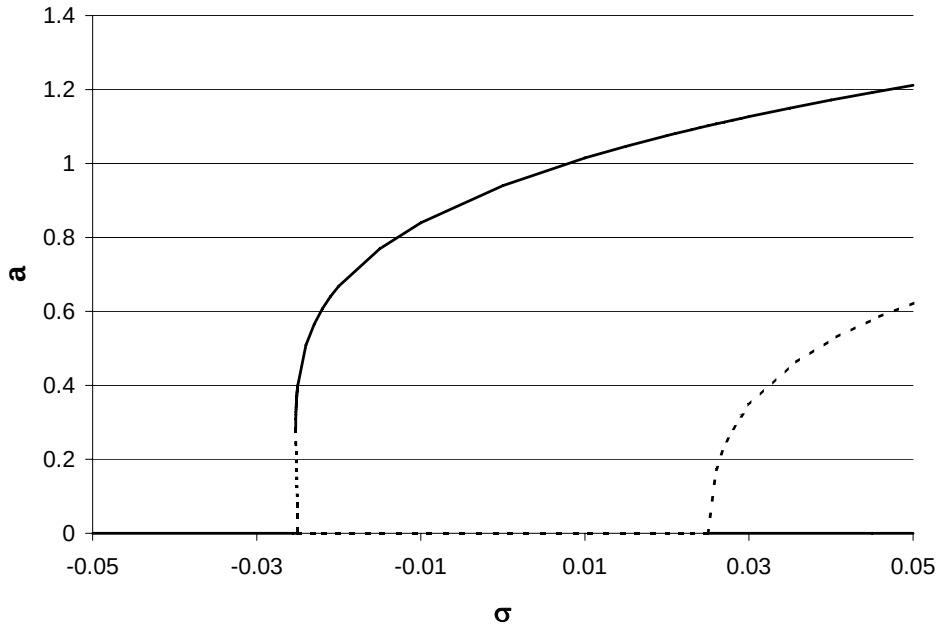

(a)

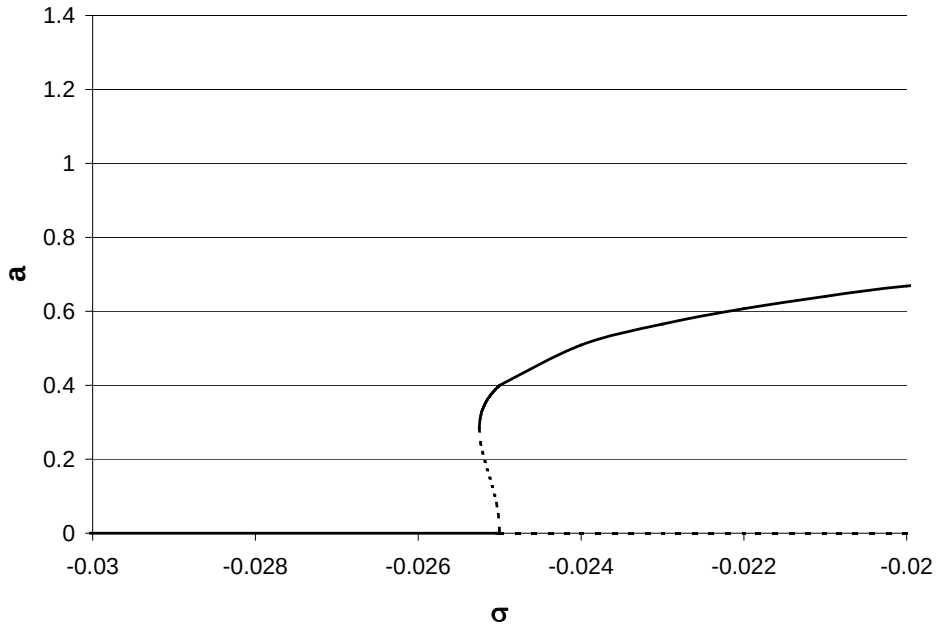

(b)

Figure 5.6. (a) Frequency response plot corresponding to Case E. (b) The system's frequency response in the proximity of $\sigma = -0.025$.

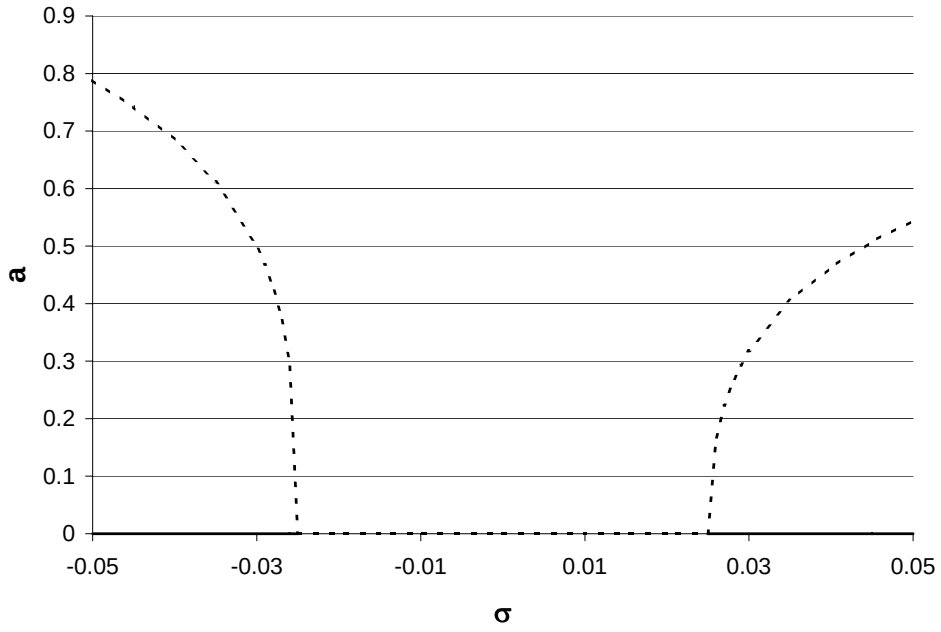

Figure 5.7. Frequency response plot corresponding to Case F.

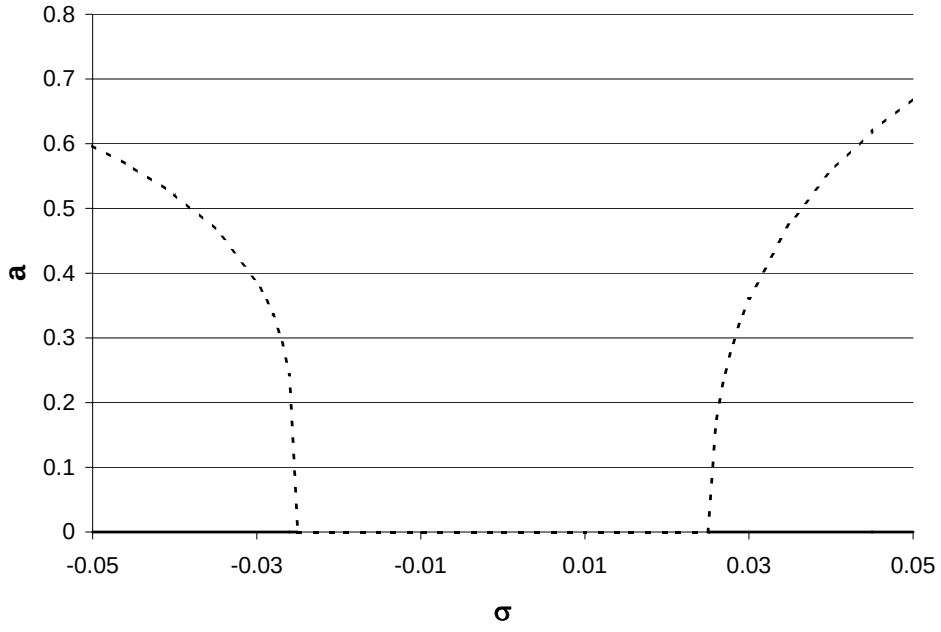

Figure 5.8. Frequency response plot corresponding to Case G.

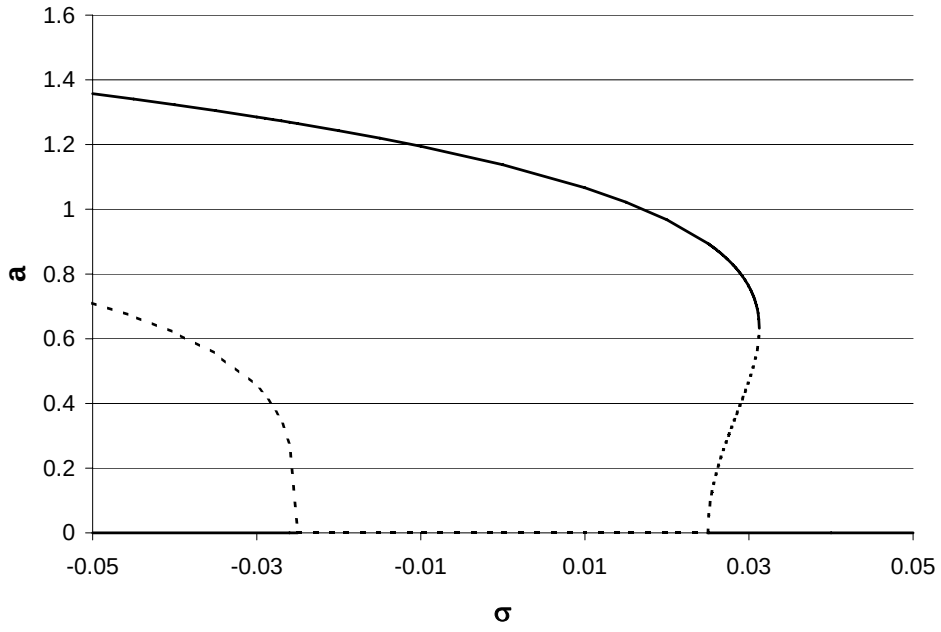

Figure 5.9. Frequency response plot corresponding to Case H.

5.4 The Response of a Representative EMA Microbeam System

While the preceding section provides a comprehensive overview of the qualitatively-distinct frequency response structures that can be realized with a given electromagnetically-actuated microbeam system, it does not clearly delineate how these responses depend on various system parameters and excitation signals. In light of this, the present section examines the frequency response behavior of a representative parametrically-excited EMA microbeam (see Table 5.2 for details). Note that for present purposes, the impedance of the microbeam system is assumed to be of sufficient magnitude that the induced emf does not appreciably impact the system's excitation signal. The behavior of 'self-coupled' systems, wherein the emf does appreciably alter the drive current, is briefly considered in Chapter 7.

Using the results of Section 5.2, the behavior of the representative microbeam system delineated in Table 5.2 can be systematically recovered. As this behavior is

Table 5.2. Parameter values, obtained from a representative microcantilever, used to produce the frequency response plots shown in Figures 5.10-5.12.

Physical Parameter	Value
Width	23.5 μm
Length	162 μm
Thickness	250 nm
Young's Modulus (E)	159 GPa
Mass Density (ρ)	0.1 kg/m^3
Magnetic Field Strength (B)	1 T

qualitatively dependent on the magnitudes of i_{DC} and i_2, the present discussion is framed in the context of varying drive currents.

Figure 5.10 depicts the frequency response structure of an electromagnetically-actuated microbeam excited with comparatively small drive amplitudes, namely, i_{DC} = 0.0 mA and i_2 = 1.0 mA. As expected, this operating condition, much like its unforced counterpart, renders a hardening response, similar to Case A, wherein both of the system's nontrivial response branches bend to the right. As increasing the amplitude of the system's AC drive current (i_2) from this operating point yields purely-vertical translations in both of the nonlinear parameter spaces presented in Figure 5.1, the qualitative response depicted in Figure 5.10 is maintained with increasing AC current until the system bifurcates at the $\nu_{3,2} = 0$ threshold, or approximately i_2 = 4.68 mA. Here the frequency response depicted in Figure 5.11, which was produced using drive currents of i_{DC} = 0.0 mA and i_2 = 6.0 mA, first emerges. This response, similar to Case E, features hardening-like global behavior, wherein both response branches eventually bend to the right (following an additional saddle node bifurcation on the left nontrivial branch). Further increasing the system's AC drive current (i_2) from this operating point again yields purely-vertical translations in both of the nonlinear parameter spaces depicted in Figure 5.1. Accordingly, the qualitative response depicted in Figure 5.11 is maintained with increasing AC current until the system bifurcates again at the $\nu_{5,2} = 0$ threshold, or i_2 = 69.2 mA. Here the

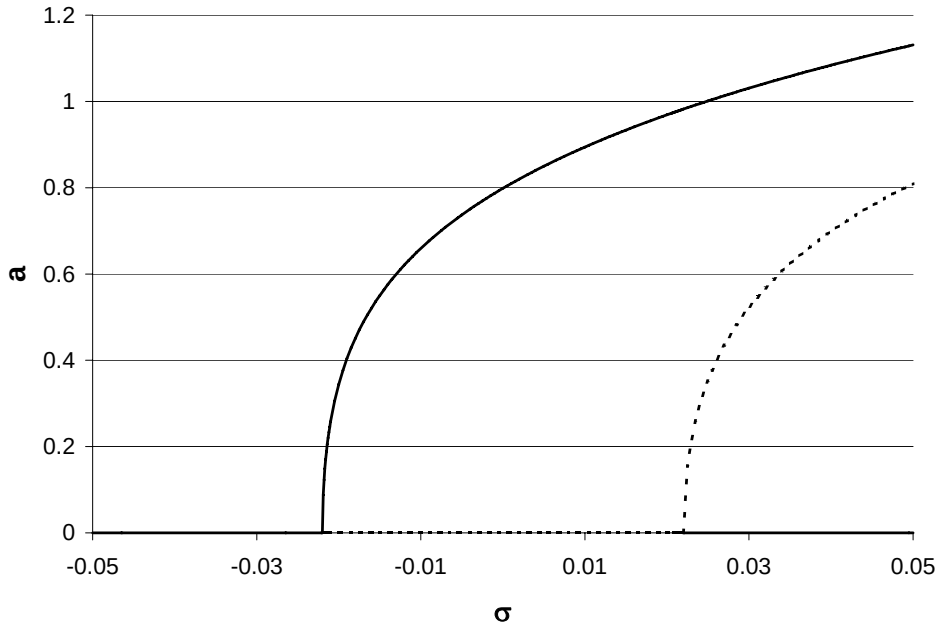

Figure 5.10. Frequency response plot corresponding to the representative microbeam system (see Table 5.2) operated with $i_{DC} = 0.0$ mA and $i_2 = 1.0$ mA.

frequency response structure shown in Figure 5.12, which was produced using drive currents of $i_{DC} = 0.0$ mA and $i_2 = 80.0$ mA, emerges. This response, similar to Case F, features a globally unbounded frequency response, wherein the nontrivial response branches bend away from one another. Generally speaking, this response, which will undoubtedly be bounded in practice by higher-order nonlinearities, is believed to be of limited practical utility.

While the preceding discussion details each of the qualitatively-distinct frequency response structures that can be obtained by fixing i_{DC} and varying i_2, it is important to note that the DC bias current can be changed independently or concurrently, as well. This not only allows for linear frequency tuning, but also facilitates the emergence of additional, distinct nonlinear frequency response structures. Rather than delineating each of these new structures, of which there are many, here, suffice it to note that a number of qualitatively-distinct response can be realized by varying each of the two drive currents provided that the buckling instability and burnout

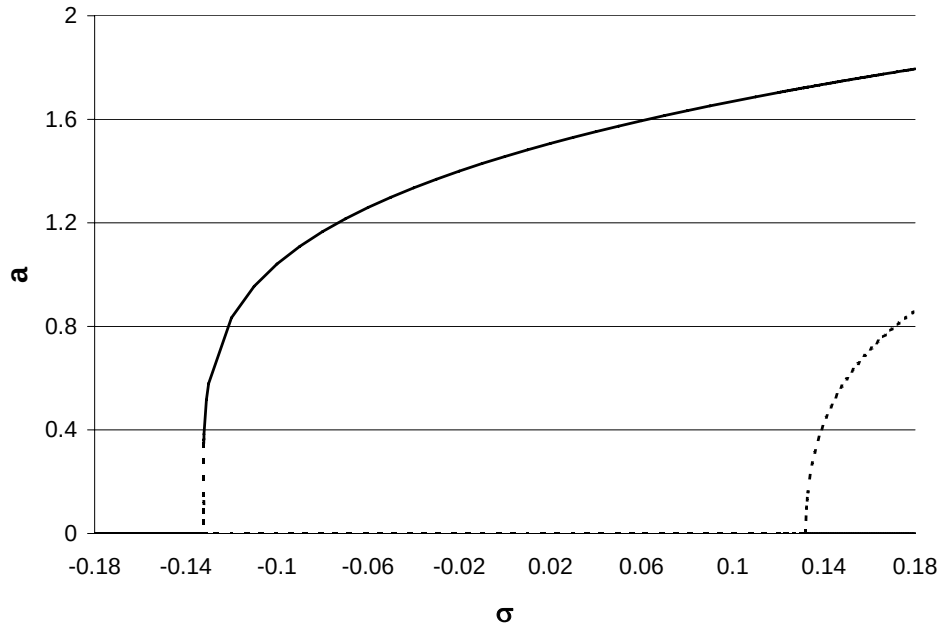

Figure 5.11. Frequency response plot corresponding to the representative microbeam system (see Table 5.2) operated with $i_{DC} = 0.0$ mA and $i_2 = 6.0$ mA.

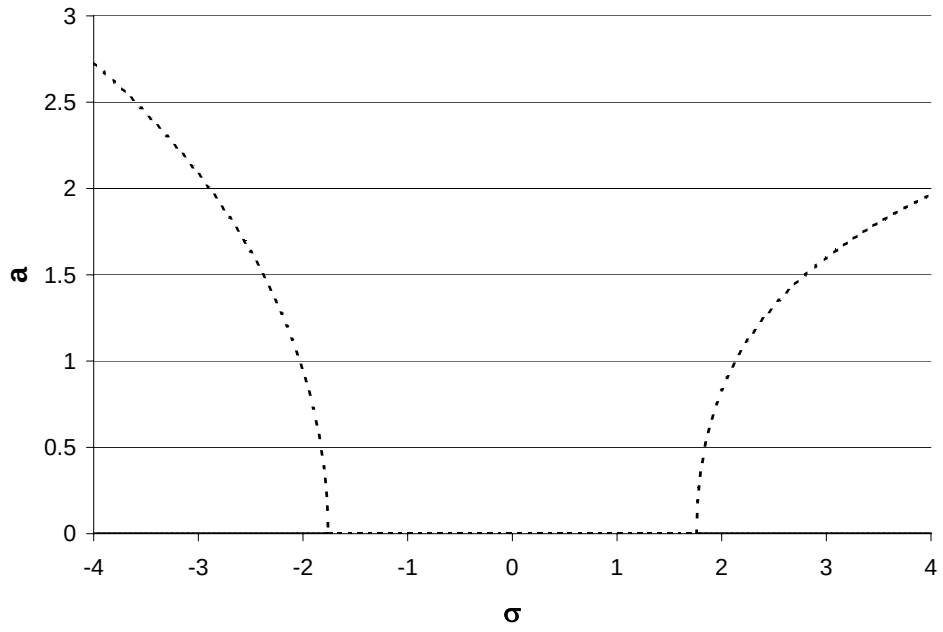

Figure 5.12. Frequency response plot corresponding to the representative microbeam system (see Table 5.2) operated with $i_{DC} = 0.0$ mA and $i_2 = 80.0$ mA.

thresholds are not exceeded.

5.5 Exploiting Nonlinear Frequency Response Structures for Mass Sensing

In light of the results detailed in Section 5.4, it is prudent to revisit the stated application for the EMA microsystems detailed herein, namely, resonant mass sensing. As detailed in the introduction, resonant mass sensors that utilize nonlinear frequency response structures ideally exploit sharp transitions in amplitude, that occur at a given instability point. While both subcritical and supercritical pitchfork bifurcations can lead to such transitions, sub-critical pitchfork bifurcations offer greater utility, because jump bifurcations are often attendant to this instability. In light of this, the most desirable frequency response structures for mass sensing are likely akin to that depicted in Figure 5.11 (Note that due to the large number of parameters associated with these systems, frequency response structures similar to those described herein are perhaps best realized though guess and check design techniques or more advanced iterative procedures). This response not only features a subcritical instability, but also exhibits an additional saddle-node bifurcation, which renders a hardening-like frequency response. Collectively, these features not only allow for qualitative analyte assessment, as a jump in amplitude can be equivocated with an analyte detection event, but also quantitative assessment, as post-bifurcation changes in amplitude can be used to quantify the mass or concentration of target analyte present.

To quantify the aforementioned jump in amplitude, as well as its sensitivity to changes in the detuning parameter σ, it is helpful to revisit Equations (5.8) and (5.9). Using these expressions, quick computation reveals that the change in amplitude near the subcritical instability at σ_2, provided $\nu_{3,2} < 0$, is given by

$$a = 2\sqrt{\frac{-2\nu_{3,2}}{\nu_{5,2}}}. \tag{5.23}$$

Likewise, the sensitivity of the response amplitude near the instability, as computed with respect to the detuning parameter σ, is given by

$$\frac{\partial a}{\partial \sigma} = \sqrt{\frac{-2\nu_{5,2}}{{\nu_{3,2}}^3}}. \tag{5.24}$$

Though ideally it would be best to maximize each of these quantities, there is clearly a trade-off that must be considered during design. As this design consideration is dependent on the application of interest (namely, whether quantitative or qualitative assessment has priority) further discussion is omitted here.

Before proceeding, it is important to note that the performance of the mass sensors detailed herein, much like that of their linear counterparts detailed in Chapter 2, is heavily dependent on the amount and type of noise present during the course of operation. In linear systems, additive and multiplicative noise affects a given device by constraining the accuracy with which a given frequency shift can be measured (the system's so-called frequency resolution). In nonlinear devices, however, additive and multiplicative noise affects the location of the aforementioned jump bifurcation. Recent work by collaborators, in addition to others, has attempted to quantitatively characterize the effects of this noise in nonlinear, parametrically-excited systems [156, 203]. However, a deeper understanding must be sought prior to final sensor implementation.

CHAPTER 6

Electromagnetically-Actuated Microbeam Resonators: Parametric Amplification

As noted in the introduction, since the publication of Rugar and Grütter's seminal work in 1991 [129], parametric amplification, the process of amplifying a time-varying signal with a parametric pump, has been demonstrated in a wide variety of resonant microtransducers (see, for example, References [103, 130–138]). Despite the breadth of this research, to the best of the author's knowledge, parametric amplification has not been successfully implemented in EMA resonators. Given that these devices exploit induced electromotive forces (emf) for sensing, which can be several orders of magnitude smaller than the drive signal (typically 10 μV or below), the need for on-chip, low-noise response amplification in electromagnetically-sensed microsystems is paramount. In light of this, the present chapter investigates the implementation of degenerate, mechanical domain parametric amplification in EMA microsystems, specifically, resonant microcantilevers similar to that shown in Figure 1.3. The realization of low-noise response amplification in these systems should facilitate their eventual implementation as linear resonant mass sensors.

Using the results of Chapter 4, the present investigation begins in Section 6.1 with the development of a consistent lumped-mass model for the amplified microcantilever system. In Section 6.2, this model is analyzed using the method of averaging and

pertinent system metrics are recovered. The chapter concludes in Section 6.3 with an examination of preliminary experimental results which (partially) validate the work's analytical findings.

6.1 Model Development

Since parametric amplification is, generally speaking, a linear phenomenon, a truncated variant of the system model presented in Equation (4.24), namely,

$$\frac{\partial^2 \hat{v}}{\partial \hat{t}^2} + \hat{c}\frac{\partial \hat{v}}{\partial \hat{t}} + \frac{\partial^4 \hat{v}}{\partial \hat{s}^4} + \frac{l^2}{EI}\frac{\partial^2 \hat{v}}{\partial \hat{s}^2}\int_1^{\hat{s}} F_1(t)\delta\left(\hat{s}-1\right) d\hat{s} = \frac{F_2(t)l^3}{v_0 EI}\delta\left(\hat{s}-1\right) \tag{6.1}$$

can be used as a basis of study. Here, however, an alternative form of the Lorentz force given by

$$\begin{aligned} \vec{F}(\hat{t}) &= F_1(\hat{t})\mathbf{i} + F_2(\hat{t})\mathbf{j} \\ &= \left[i_1 \cos(\hat{\omega}\hat{t}+\phi) + i_2 \cos 2\hat{\omega}\hat{t}\right] gB\left(\cos\alpha\mathbf{i} + \sin\alpha\mathbf{j}\right), \end{aligned} \tag{6.2}$$

must be used. Note that current components with frequency $\hat{\omega}$ are used here, in conjunction with the obliquely oriented magnetic field, to provide a direct excitation to the system. Similarly, current components with frequency $2\hat{\omega}$ are used, in conjunction with the obliquely oriented magnetic field, for parametric pumping. Furthermore, note that this specific force model, which includes a strict 2:1 excitation frequency ratio and a relative phase term, is utilized due to the present study's focus on *degenerate* parametric amplification. This phase-sensitive amplification technique is emphasized here because it, in theory, is noise free down to the quantum mechanical level [129, 136, 204]. Investigations of *non-degenerate* parametric amplification, which is phase-independent and does not require the strict frequency constraint, but is known to yield additional noise, are left to subsequent works.

Given that a lumped-mass model proves sufficiently accurate for the present analysis, the dynamic variable $\hat{v}(\hat{s},\hat{t})$ appearing in Equation (6.1) can be decomposed, as

before, into its spatial and temporal components using the microbeam's first mode shape $\Psi(\hat{s})$, which is derived from the beam's simplified spatial eigenvalue problem

$$\Psi^{iv} - \omega_i^2 \Psi = 0, \tag{6.3}$$

with boundary conditions

$$\Psi(0) = 0, \qquad \Psi'(0) = 0, \qquad \Psi''(1) = 0, \qquad \Psi'''(1) = 0, \tag{6.4}$$

according to

$$\hat{v}(\hat{s}, \hat{t}) = w(\hat{t})\Psi(\hat{s}). \tag{6.5}$$

(Note that here, as before, an axial force component can be added to the modal equation to yield a more accurate mode shape approximation. This additional term is neglected here, because the axial force produces minimal distortion in the system's first mode shape.) Projecting the decomposed governing equation back onto the system's first mode shape through the use of an inner product operator results in a final lumped-mass equation of motion for the system given by

$$\begin{aligned} z'' + 2\varepsilon\zeta z' + [1 + \varepsilon\lambda_1 \cos(\Omega\tau + \phi) + \varepsilon\gamma_1 \cos 2\Omega\tau]\, z \\ = \varepsilon\eta_1 \cos(\Omega\tau + \phi) + \varepsilon\eta_2 \cos 2\Omega\tau. \end{aligned} \tag{6.6}$$

System parameters corresponding to this equation are defined in Table 6.1.

6.2 Steady-State Amplifier Response

As the equation of motion detailed above is linear, an analytical expression for the system's response can be derived using conventional state transition techniques. However, as this solution method requires the use of an infinite (Peano-Baker) series, both qualitative analysis and predictive design benefit from an alternative approach. Accordingly, the present work utilizes a standard perturbation technique, the method of averaging, to derive a closed-form (approximate) solution. To facilitate this approach,

Table 6.1. Nondimensional parameter definitions corresponding to Equation (6.6). Note that ε represents a 'small' parameter introduced for the sake of analysis.

Parameter
$z = w(\hat{t})$
$\tau = \omega_0 \hat{t}, \qquad (\bullet)' = \dfrac{d(\bullet)}{d\tau}$
$\hat{\omega} = \omega T, \qquad \Omega = \dfrac{\hat{\omega}}{\omega_0}$
$\omega_0^2 = \displaystyle\int_0^1 \Psi \Psi^{iv} d\hat{s}$
$\varepsilon\zeta = \dfrac{\hat{c}}{2\omega_0}$
$\varepsilon\lambda_1 = \dfrac{i_1 g B l^2 \cos\alpha}{EI w_0^2} \displaystyle\int_0^1 \Psi \Psi'' \int_1^{\hat{s}} \delta(\hat{s}-1)\, d\hat{s} d\hat{s}$
$\varepsilon\gamma_1 = \dfrac{i_2 g B l^2 \cos\alpha}{EI w_0^2} \displaystyle\int_0^1 \Psi \Psi'' \int_1^{\hat{s}} \delta(\hat{s}-1)\, d\hat{s} d\hat{s}$
$\varepsilon\eta_1 = \dfrac{i_1 g B l^3 \sin\alpha}{EI v_0 \omega_0^2} \displaystyle\int_0^1 \Psi \delta(\hat{s}-1)\, d\hat{s}$
$\varepsilon\eta_2 = \dfrac{i_2 g B l^3 \sin\alpha}{EI v_0 \omega_0^2} \displaystyle\int_0^1 \Psi \delta(\hat{s}-1)\, d\hat{s}$

a constrained coordinate change, given by

$$\begin{aligned} z(\tau) &= X(\tau)\cos(\Omega\tau) + Y(\tau)\sin(\Omega\tau), \\ z'(\tau) &= -X(\tau)\Omega\sin(\Omega\tau) + Y(\tau)\Omega\cos(\Omega\tau), \end{aligned} \tag{6.7}$$

and a frequency detuning parameter σ, defined by

$$\sigma = \frac{\Omega - 1}{\varepsilon}, \tag{6.8}$$

are introduced into Equation (6.6). Separating the equation that results from substitution, as well as the state variable constraint equation, in terms of X' and Y', and averaging over one period of the oscillator's response ($2\pi/\Omega$) yields a pair of averaged equations governing the system's behavior:

$$\begin{aligned} X' &= -\frac{1}{4}\varepsilon\left(\gamma_1 Y + 4\sigma Y + 4\zeta X - 2\eta_1\sin\phi\right) + \mathcal{O}(\varepsilon^2), \\ Y' &= -\frac{1}{4}\varepsilon\left(\gamma_1 X - 4\sigma X + 4\zeta Y - 2\eta_1\cos\phi\right) + \mathcal{O}(\varepsilon^2). \end{aligned} \tag{6.9}$$

Using this set of equations, the transducer's steady-state behavior can be recovered by setting $(X', Y') = (0, 0)$ and solving for the dynamic variables X and Y. This yields a steady-state solution given, in terms of amplitude and phase, by

$$\bar{a} = 2\sqrt{\frac{\eta_1^2\left[\gamma_1^2 + 16(\zeta^2+\sigma^2) + 8\gamma_1\left(\sigma\cos 2\phi - \zeta\sin 2\phi\right)\right]}{\left[\gamma_1^2 - 16(\sigma^2+\zeta^2)\right]^2}}, \tag{6.10}$$

$$\bar{\psi} = \arctan\left[\frac{(\gamma_1 - 4\sigma)\sin\phi - 4\zeta\cos\phi}{(\gamma_1 + 4\sigma)\cos\phi - 4\zeta\sin\phi}\right], \tag{6.11}$$

where

$$\bar{a} = \sqrt{\bar{X}^2 + \bar{Y}^2}, \qquad \bar{\psi} = \arctan\frac{\bar{Y}}{\bar{X}}. \tag{6.12}$$

Using this closed-form expression for the amplifier's response amplitude, the gain of the system can be recovered. For present purposes, this amplifier metric is defined according to

$$G = \frac{\bar{a}_{pump\ on}}{\bar{a}_{pump\ off}} = \frac{\bar{a}}{\bar{a}|_{\gamma_1=0}}, \tag{6.13}$$

which at $\sigma = 0$ yields

$$G(\sigma = 0) = 4\zeta \sqrt{\frac{\gamma_1^2 + 16\zeta^2 - 8\gamma_1 \zeta \sin 2\phi}{(\gamma_1^2 - 16\zeta^2)^2}}. \tag{6.14}$$

Before proceeding with an analytical examination of the amplifier's performance, it is important to note that due to the potential for parametric resonance in the microscale amplifier, robust operation requires that the system function below the resonator's Arnold tongue or 'wedge of instability': a threshold which dictates the onset of parametric resonance (for additional details see, for example, References [125, 195]). For this particular system, the equation governing the aforementioned threshold can be directly recovered from the denominator of Equation (6.12), namely,

$$\gamma_1^2 - 16(\sigma^2 + \zeta^2) = 0. \tag{6.15}$$

This conditions results in a maximum allowable value for the system's pump amplitude, γ_1, given by

$$\gamma_{1,crit} = 4\sqrt{\sigma^2 + \zeta^2}. \tag{6.16}$$

Note that for reference purposes, a set of representative Arnold tongues (recovered for various levels of damping) are depicted in Figure 6.1. For the sake of completeness, it is also worth noting that higher-order instability regions can also be utilized for amplification. However, as these wedges are more difficult to locate experimentally, particular emphasis is placed here on the primary instability region (i.e. near $\sigma = 0$).

With a maximum bound on γ_1 established, the resonant amplifier's qualitative behavior can be readily characterized. Figure 6.2, for example, depicts the system's frequency response for γ_1 values of 0 (unpumped), 0.01, and 0.02. As evident, with increasing pump amplitude the normalized resonant amplitude increases from unity to approximately 1.33 to 2. Though these gains are appreciable, Figure 6.3 verifies that significantly larger gains are obtainable as the pump amplitude approaches $\gamma_{1,crit}$, which is 0.04 for this particular example. Specifically, the figure shows a monotonic

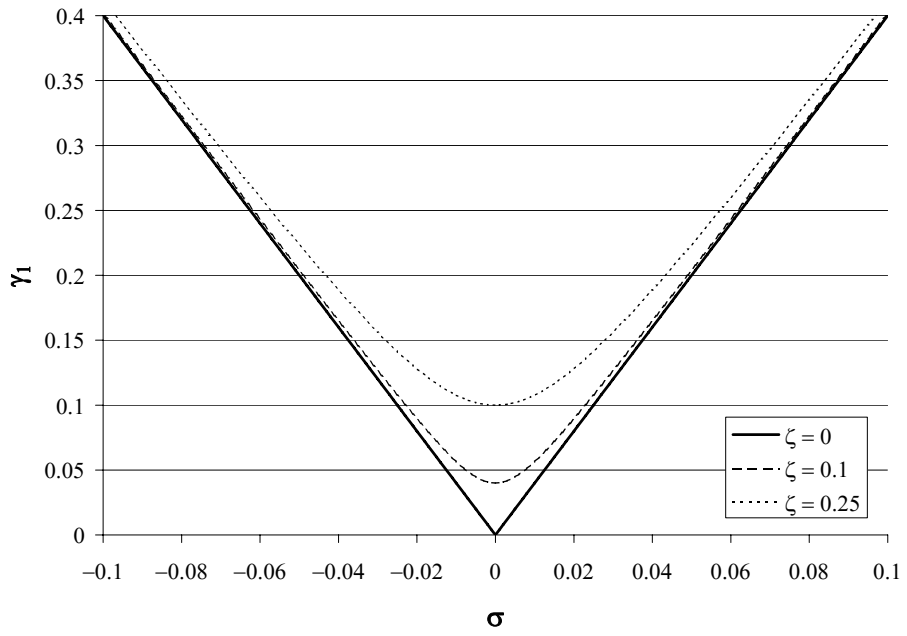

Figure 6.1. The system's Arnold tongue/'wedge of instability' near $\sigma = 0$. Note that robust amplification requires that the system operate below the parametric resonance threshold.

increase in gain with increasing pump amplitude, with the gain approaching infinity as γ_1 approaches $\gamma_{1,crit}$ (as the parametric instability is reached). Likewise, gains approaching infinity can realized by fixing γ_1 and increasing ζ until the parametric instability and pump value coincide. Though these large, multiple-order-of-magnitude gains are promising, it is important to note that both system uncertainties and nonlinearities can hinder the realization of extremely large gains in micromechanical devices (though gains on the order of 4 are experimentally realized in the following section).

Before proceeding with an experimental investigation of the parametric amplifiers described herein, it is important to note the phase-dependent nature of the system gain given in Equation (6.14). Figure 6.4 graphically depicts this dependence. As evident, as the relative excitation phase ϕ is varied, the system gain changes appreciably, with maximum gains being realized for relative phase angles of -45° (and 180° multiples) and minimum gains being realized for relative phase angles of 45° (and 180°

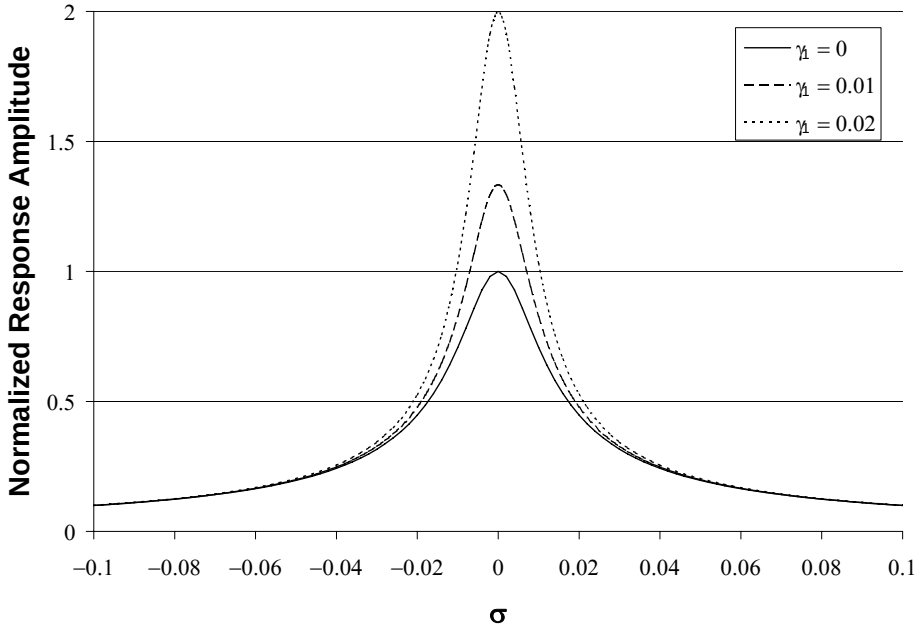

Figure 6.2. Frequency response curves (theoretical) corresponding to three different pump amplitudes (values of γ_1). Note that the responses have been normalized such that the peak amplitude of the unpumped system is unity. Also note that here and in Figures 6.3-6.4 $\zeta = 0.01$.

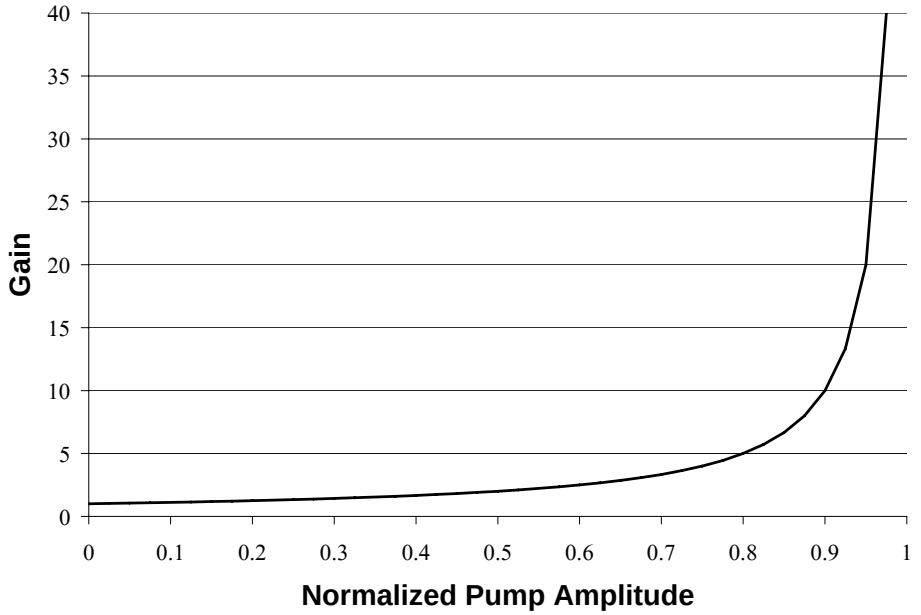

Figure 6.3. Amplifier gain (theoretical) plotted versus pump amplitude for an oscillator operating at $\sigma = 0$ with $\phi = -45°$. Note that the pump amplitude has been normalized such that the parametric resonance threshold occurs at unity.

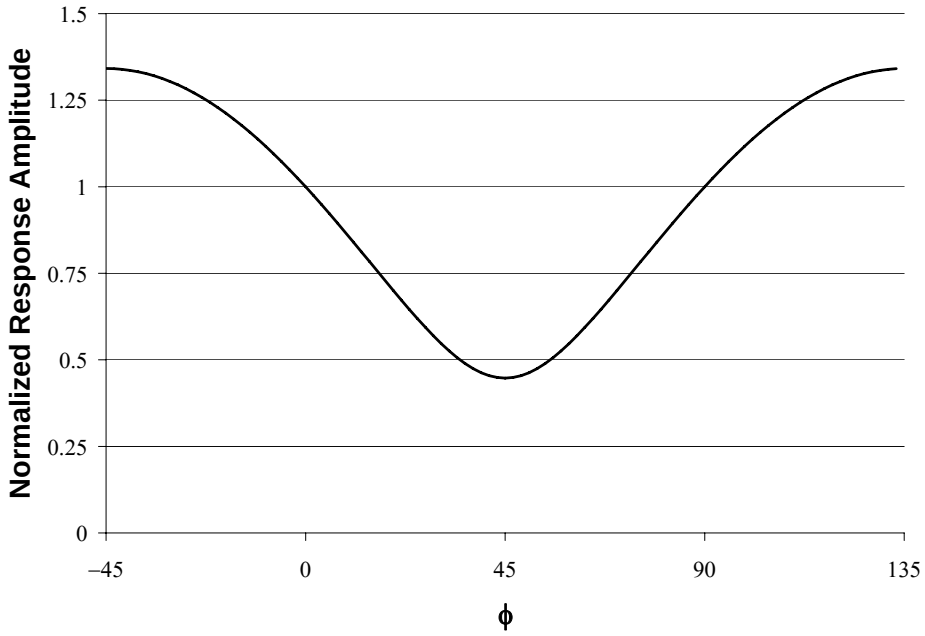

Figure 6.4. Response amplitude (theoretical) versus phase plot. Note that the response has been normalized such that the amplitude at $\phi = 0^\circ$ is unity. For this plot $\gamma_1 = 0.02$.

multiples). Clearly the former case is ideal for most scenarios, namely, those where robust amplification is desired. The latter case, however, may provide an effective means of truncating undesirable resonances in some microstructures.

6.3 Experimental Results

In order to verify the analytical results presented in the preceding section, a series of silicon microcantilevers, similar to that shown in Figure 1.3, were fabricated (additional details can be found in References [157, 171]). A representative device, measuring 23.5 μm wide by 162 μm long by 250 nm thick, with a first natural frequency of approximately 40.82 kHz, was then mounted on a test-rig containing an integrated NdFeB permanent magnet (1 T), oriented such that $\alpha = 15^\circ$ (to ensure a strong parametric pump), and placed in a partial-vacuum environment (an ambient pressure of approximately 35 mT was recorded). The parametrically-amplified

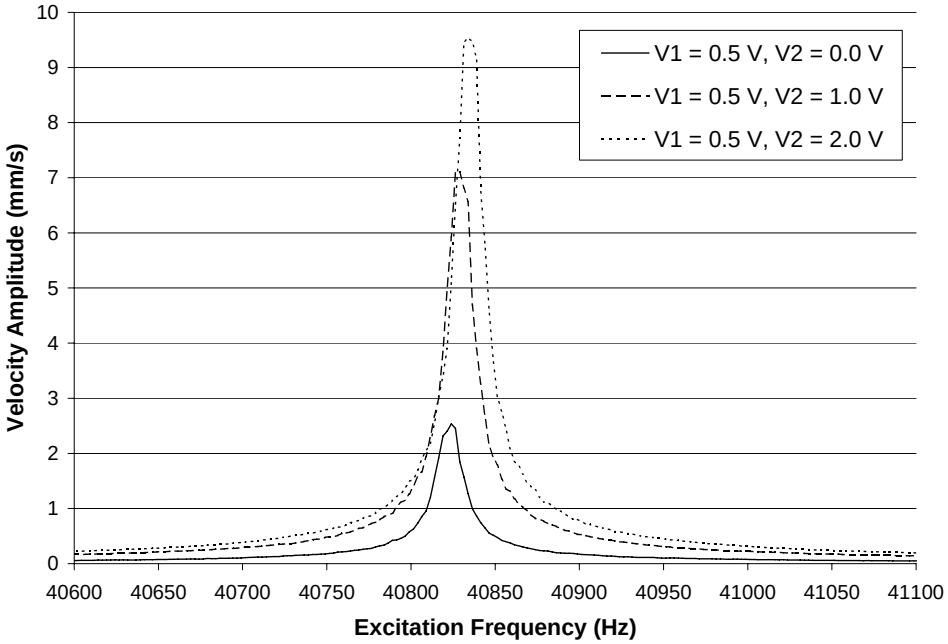

Figure 6.5. Frequency response curves (experimental) obtained for three different pump amplitudes. Note that this relative phase configuration leads to resonance amplification.

system was then driven with a 0.5 V harmonic signal (V_1) and tested using a wide range of pump amplitude (V_2) and relative excitation phase (ϕ) settings. Preliminary results acquired during the course of experimentation are summarized below. Note that voltage inputs were used in place of current inputs solely for experimental convenience.

Figures 6.5 and 6.6 depict the frequency response behavior of the EMA microcantilever system with two distinct relative phase values (unfortunately, as the relative phases appear to have shifted, through experimentation, the exact values of ϕ here are unknown). As evident, the first excitation signal resulted in appreciable amplifier gains. Likewise, the second excitation signal resulted in truncated resonant amplitudes. Though quite preliminary, these results are believed to be a positive indication of the feasibility of parametric amplification in electromagnetically-actuated microsystems.

Figure 6.7 depicts the experimental gain/phase relationship that was recovered

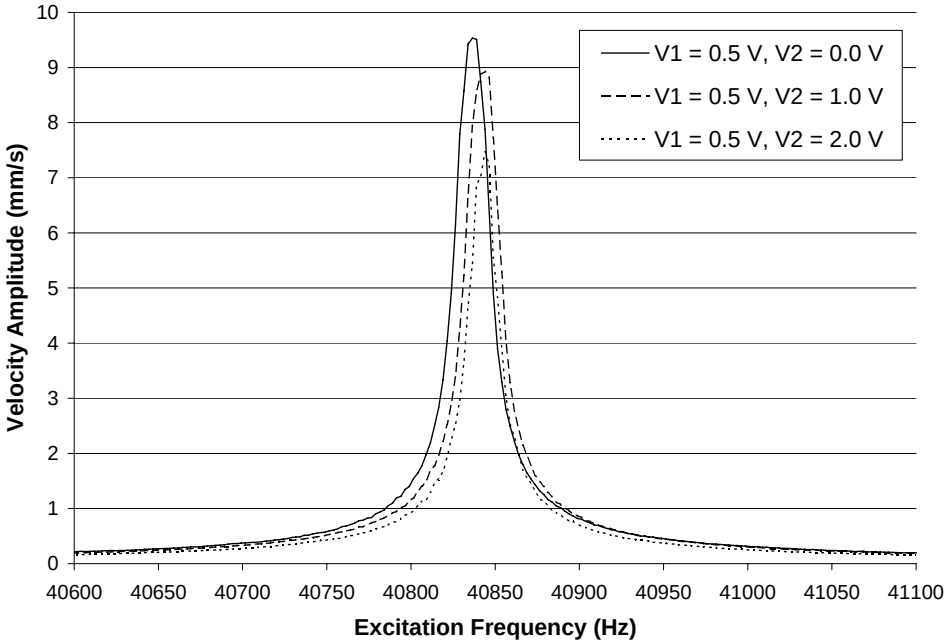

Figure 6.6. Frequency response curves (experimental) obtained for three different pump amplitudes. Note that this relative phase configuration leads to resonance truncation.

from the EMA microbeam actuated by a signal with identifiable relative phase information. Though the location of the minimum gain is shifted slightly from the value predicted in Figure 6.4, the trends exhibited by the two plots are quite similar.

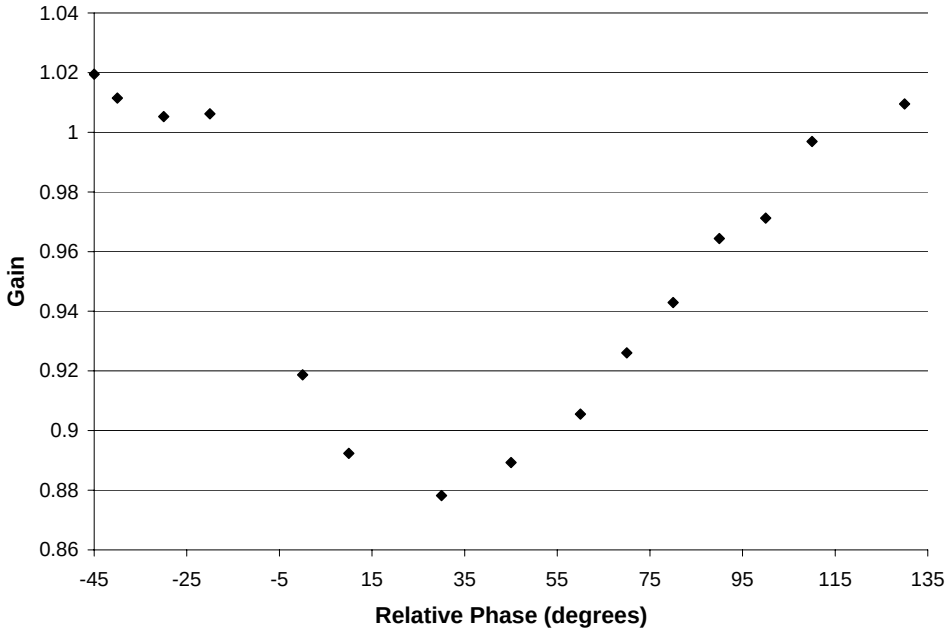

Figure 6.7. Gain (experimental) versus phase plot. Note that the response has been normalized such that the gain at $\phi = 0$ is unity.

CHAPTER 7

Conclusions and Directions for Future Work

This dissertation examines the use of coupled, nonlinear, and/or parametrically-excited microelectromechanical oscillators in resonant mass sensing applications. Specifically, the work considers the behavior of (i) single input - single output, multi-analyte mass sensors based on coupled array architectures (Chapter 2), (ii) electrostatically-actuated microbeams driven with purely-parametric excitations (Chapter 3), and (iii) electromagnetically-actuated and sensed microbeam systems (Chapters 4-6). Not surprisingly, given this breadth of coverage, a number of distinct conclusions can be drawn from the work. Rather than recapitulating each of these points, which are detailed at some length in the preceding chapters, here, the dissertation's major contributions are outlined below in Section 7.1. This is followed in Section 7.2 by a brief overview of ongoing and future work.

7.1 Contributions of the Work

In the broadest sense, the investigation detailed herein serves to further the general understanding of resonant mass sensors based on coupled, nonlinear, and/or parametrically-excited microresonators. In the course of realizing this goal, however, a number of specific contributions have been made to the fields of nonlinear dynamics,

vibrations, and MEMS. These contributions are detailed on a topical basis below.

- Chapter 2 of the work summarizes the design and development of a promising new class of resonant microsensors. The key feature of these devices is that they exploit vibration localization in a set of functionalized, frequency-mistuned microbeam resonators, each coupled to a common shuttle mass, to facilitate the detection of multiple analytes using a single sensor input (actuation signal) and a single sensor output (measurement readout). This novel SISO approach, in turn, facilitates the development of reduced power, highly integrable microsensors with performance metrics comparable to their more conventional counterparts.
- Chapter 3 of the work details the modeling, analysis, and design of a new class of electrostatically-actuated microbeams with purely-parametric excitations. These devices utilize symmetric electrostatic actuation to negate direct and/or even-powered, nonlinear parametric excitations. While this approach facilitates the realization of superior frequency response characteristics, typical device configurations render hardening frequency response structures, which are deemed to be poorly suited for the application at hand: resonant mass sensing.
- Chapters 4-6 of the work detail the modeling and analysis of nonlinear and parametrically-amplified, electromagnetically-actuated microresonators. These devices are well suited for resonant mass sensing because they are highly scalable and offer a 'self-sensing' capability (i.e. they produce a response-related electromotive force). Chapter 4 of the work summarizes the development of the first consistent, nonlinear, lumped-mass model for an electromagnetically-actuated microbeam system driven by nonlinear parametric excitations. This model is subsequently analyzed in Chapter 5 using standard perturbation methods and bifurcation theory. Frequency response structures that are well suited for nonlinear resonant mass sensing are identified and practical design issues are noted as appropriate. The technical portion of the work then concludes in Chapter 6 with

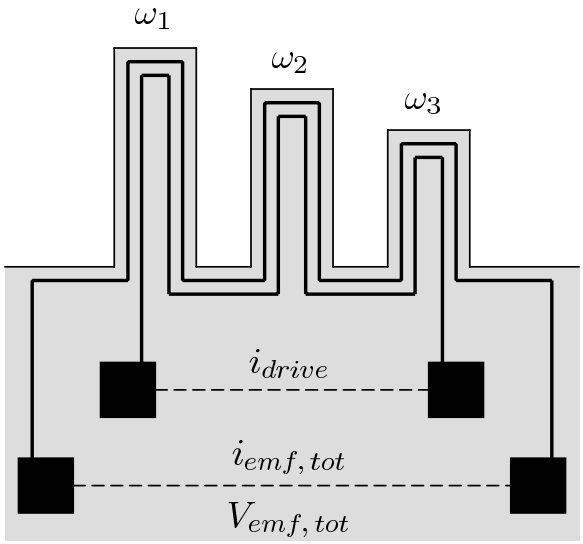

Figure 7.1. A schematic of the proposed multi-analyte sensor.

a demonstration of parametric amplification in an electromagnetically-actuated microresonator. Taken collectively, these endeavors create a firm foundation for future analytical and experimental investigations of electromagnetically-actuated microtransducers.

7.2 Future Work

While a number of areas for future work have been identified throughout the course of this dissertation, a select number of research directions are believed to be of particular importance. These topics include:

- *Single Input - Single Output, Multi-Analyte Sensors with Internal Flow-Through*: As detailed in Section 2.6, many of the issues associated with the first generation of SISO resonant mass sensors, including ambient operation and functionalization, can be overcome by incorporating internal microfluidic channels in the resonator's microbeams. Unfortunately, while recent work has made some headway in this direction (see Section 2.6), fabrication constraints are currently limiting further sensor development. Accordingly, future work is

aimed at refining the process flows needed to overcome this technical impediment.

- *Experimental Verification of the Nonlinear Behaviors Exhibited by Electromagnetically-Actuated Microbeam Resonators*: As detailed in Section 5.4, electromagnetically-actuated microbeam resonators are believed to be capable of exhibiting extremely rich nonlinear frequency response structures. However, before the results of Chapter 5 can be truly utilized in the design of nonlinear resonant mass sensors, the behaviors predicted to occur in these systems, as well as the system model itself, must be experimentally verified. Ongoing experimentation is currently focused on verifying both the nonlinear model and its associated behaviors. This research is intended to serve as a precursor to the development of functional, nonlinear, resonant mass sensors based on electromagnetically-actuated microresonators.
- *Self-Coupled Electromagnetically-Actuated Microbeams*: As detailed in Section 5.4, the analyses presented in Chapters 5 and 6 were based on the assumption that the drive signal provided by the electromagnetically-actuated resonator's current source remained invariant in the presence of a time-varying electromotive force (emf). While this assumption is a good first approximation for most microsystems, in some resonators the induced electromotive force may lead to 'self-coupling', that is, a drive current which is dependent on the dynamic response of the system. Given the form of the induced electromotive force detailed in Section 4.3, this, in turn, could potentially yield parametrically-excited systems with even nonlinearities (asymmetric potentials). As comparatively little is known about such systems, a wealth of information could be recovered through a systematic theoretical and experimental analysis.
- *Coupled Electromagnetically-Actuated Microbeam Arrays*: Though isolated, 'self-coupled', electromagnetically-actuated microbeams are of direct interest,

arrays of electromagnetically-actuated resonators, coupled through a common current loop, may be of greater utility. For example, a single input - single output, multi-analyte resonant mass sensor could be realized by coupling a number of frequency-mistuned resonators through a common current loop (see Figure 7.1). Such a device would offer all of the benefits attendant to the sensor highlighted in Chapter 2, but would not require the use of an additional shuttle mass oscillator, and thus would be much simpler to design. From a more general standpoint, devices coupled via a common current loop would also facilitate the analysis of collective behaviors, such as localization, in systems with all-to-all coupling. As the majority of studies completed to date on all-to-all coupling have been analytical in nature, experimental research in this area could have a meaningful impact.

- *Characterization of Sensitivity in Coupled and/or Nonlinear Resonant Mass Sensors*: As detailed in Chapter 2, mass sensitivity is a well defined quantity for an uncoupled, linear sensor. However, this pertinent performance metric is ill-defined, at best, in coupled and/or nonlinear resonant mass sensors. Accordingly, future work is aimed at developing a uniform definition for this metric. This task requires not only the identification of the system's mass responsivity, that is, how much the resonator's natural frequency or response amplitude changes with a given change in mass, but also an identification of the system's frequency resolution, that is, how small of a frequency shift can be accurately measured in the given resonator in the presence of noise and system uncertainty.

APPENDICES

APPENDIX A

Parameter Definitions

The following definitions correspond to the parameters included in Equation (4.31).

$$z = w(\hat{t}) \tag{A.1}$$

$$\omega_0^2 = \int_0^1 \Psi\Psi^{iv} d\hat{s} + \frac{i_{DC} g B l^2 \cos\alpha}{EI} \int_0^1 \Psi\Psi'' \int_1^{\hat{s}} \delta\left(\hat{s}-1\right) d\hat{s} d\hat{s} \tag{A.2}$$

$$\tau = \omega_0 \hat{t} \tag{A.3}$$

$$\Omega = \frac{\hat{w}}{w_0} \tag{A.4}$$

$$\varepsilon\zeta = \frac{\hat{c}}{2\omega_0} \tag{A.5}$$

$$\varepsilon\lambda_1 = \frac{i_1 g B l^2 \cos\alpha}{EI w_0^2} \int_0^1 \Psi\Psi'' \int_1^{\hat{s}} \delta\left(\hat{s}-1\right) d\hat{s} d\hat{s} \tag{A.6}$$

$$\varepsilon\gamma_1 = \frac{i_2 g B l^2 \cos\alpha}{EI w_0^2} \int_0^1 \Psi\Psi'' \int_1^{\hat{s}} \delta\left(\hat{s}-1\right) d\hat{s} d\hat{s} \tag{A.7}$$

$$\varepsilon\chi_3 = \frac{v_0^2}{\omega_0^2 l^2}\int_0^1 \Psi\Psi''^3 d\hat{s} + \frac{4v_0^2}{\omega_0^2 l^2}\int_0^1 \Psi\Psi'\Psi''\Psi''' d\hat{s} + \frac{v_0^2}{\omega_0^2 l^2}\int_0^1 \Psi\Psi'^2\Psi^{iv} d\hat{s} + \frac{3v_0^2 i_{DC} gB\cos\alpha}{2EI\omega_0^2}\int_0^1 \Psi\Psi'^2\Psi''\int_1^{\hat{s}} \delta\left(\hat{s}-1\right) d\hat{s}d\hat{s} \tag{A.8}$$

$$\varepsilon\chi_5 = \frac{6v_0^4}{\omega_0^2 l^4}\int_0^1 \Psi\Psi'^2\Psi''^3 d\hat{s} + \frac{8v_0^4}{\omega_0^2 l^4}\int_0^1 \Psi\Psi'^3\Psi''\Psi''' d\hat{s} + \frac{v_0^4}{\omega_0^2 l^4}\int_0^1 \Psi\Psi'^4\Psi^{iv} d\hat{s} + \frac{15v_0^4 i_{DC} gB\cos\alpha}{8EIl^2\omega_0^2}\int_0^1 \Psi\Psi'^4\Psi''\int_1^{\hat{s}} \delta\left(\hat{s}-1\right) d\hat{s}d\hat{s} \tag{A.9}$$

$$\varepsilon\lambda_3 = \frac{3i_1 v_0^2 gB\cos\alpha}{2EIw_0^2}\int_0^1 \Psi\Psi'^2\Psi''\int_1^{\hat{s}} \delta\left(\hat{s}-1\right) d\hat{s}d\hat{s} \tag{A.10}$$

$$\varepsilon\gamma_3 = \frac{3i_2 v_0^2 gB\cos\alpha}{2EIw_0^2}\int_0^1 \Psi\Psi'^2\Psi''\int_1^{\hat{s}} \delta\left(\hat{s}-1\right) d\hat{s}d\hat{s} \tag{A.11}$$

$$\varepsilon\lambda_5 = \frac{15i_1 v_0^4 gB\cos\alpha}{8EIl^2w_0^2}\int_0^1 \Psi\Psi'^4\Psi''\int_1^{\hat{s}} \delta\left(\hat{s}-1\right) d\hat{s}d\hat{s} \tag{A.12}$$

$$\varepsilon\gamma_5 = \frac{15i_2 v_0^4 gB\cos\alpha}{8EIl^2w_0^2}\int_0^1 \Psi\Psi'^4\Psi''\int_1^{\hat{s}} \delta\left(\hat{s}-1\right) d\hat{s}d\hat{s} \tag{A.13}$$

$$\varepsilon\beta = \frac{v_0^2}{l^2}\int_0^1 \Psi\Psi''\int_1^{\hat{s}}\int_0^{\hat{s}} \Psi'^2 d\hat{s}d\hat{s}d\hat{s} + \frac{v_0^2}{l^2}\int_0^1 \Psi\Psi'\int_0^{\hat{s}} \Psi'^2 d\hat{s}d\hat{s} \tag{A.14}$$

$$\varepsilon\nu_1 = \frac{3v_0^4}{2l^4}\int_0^1 \Psi\Psi''\int_1^{\hat{s}}\int_0^{\hat{s}} \Psi'^4 d\hat{s}d\hat{s}d\hat{s} + \frac{3v_0^4}{2l^4}\int_0^1 \Psi\Psi'\int_0^{\hat{s}} \Psi'^4 d\hat{s}d\hat{s} + \frac{3v_0^4}{2l^4}\int_0^1 \Psi\Psi'^2\Psi''\int_1^{\hat{s}}\int_0^{\hat{s}} \Psi'^2 d\hat{s}d\hat{s}d\hat{s} + \frac{v_0^4}{2l^4}\int_0^1 \Psi\Psi'^3\int_0^{\hat{s}} \Psi'^2 d\hat{s}d\hat{s} \tag{A.15}$$

$$\varepsilon\nu_2 = \frac{v_0^4}{2l^4}\int_0^1 \Psi\Psi''\int_1^{\hat{s}}\int_0^{\hat{s}} \Psi'^4 d\hat{s}d\hat{s}d\hat{s} + \frac{v_0^4}{2l^4}\int_0^1 \Psi\Psi'\int_0^{\hat{s}} \Psi'^4 d\hat{s}d\hat{s} + \frac{3v_0^4}{2l^4}\int_0^1 \Psi\Psi'^2\Psi''\int_1^{\hat{s}}\int_0^{\hat{s}} \Psi'^2 d\hat{s}d\hat{s}d\hat{s} + \frac{v_0^4}{2l^4}\int_0^1 \Psi\Psi'^3\int_0^{\hat{s}} \Psi'^2 d\hat{s}d\hat{s} \tag{A.16}$$

$$\varepsilon\eta_0 = \frac{i_{DC} g B l^3 \sin\alpha}{EI v_0 \omega_0^2} \int_0^1 \Psi\delta\left(\hat{s}-1\right) d\hat{s} \tag{A.17}$$

$$\varepsilon\eta_1 = \frac{i_1 g B l^3 \sin\alpha}{EI v_0 \omega_0^2} \int_0^1 \Psi\delta\left(\hat{s}-1\right) d\hat{s} \tag{A.18}$$

$$\varepsilon\eta_2 = \frac{i_2 g B l^3 \sin\alpha}{EI v_0 \omega_0^2} \int_0^1 \Psi\delta\left(\hat{s}-1\right) d\hat{s} \tag{A.19}$$

BIBLIOGRAPHY

BIBLIOGRAPHY

[1] H. C. Nathanson, W. E. Newell, R. A. Wickstrom, and J. R. Davis Jr., "The resonant gate transistor," *IEEE Transactions on Electron Devices*, vol. 14, no. 3, pp. 117–133, 1967.

[2] H. C. Nathanson and R. A. Wickstrom, "A resonant-gate silicon surface transistor with high-Q band-pass properties," *Applied Physics Letters*, vol. 7, no. 4, pp. 84–86, 1965.

[3] K. Petersen, "Silicon as a mechanical material," *Proceedings of the IEEE*, vol. 70, no. 5, pp. 420–457, 1982.

[4] B. Piekarski, D. DeVoe, M. Dubey, R. Kaul, J. Conrad, and R. Zeto, "Surface micromachined piezoelectric resonant beam filters," *Sensors and Actuators A: Physical*, vol. 91, no. 3, pp. 313–320, 2001.

[5] K. Wang and C. T.-C. Nguyen, "High-order micromechanical electronic filters," in *Proceedings of the 1997 IEEE International Micro Electro Mechanical Workshop*, (Nagoya, Japan), pp. 25–30, 1997.

[6] D. S. Greywall, "Micromechanical RF filters excited by the Lorentz force," *Journal of Micromechanics and Microengineering*, vol. 9, no. 1, pp. 78–84, 1999.

[7] L. Lin, R. T. Howe, and A. P. Pisano, "Microelectromechanical filters for signal processing," *Journal of Microelectromechanical Systems*, vol. 7, no. 3, pp. 286–294, 1998.

[8] C. T.-C. Nguyen, "Micromechanical filters for miniaturized low-power communications," in *Proceedings of SPIE: Smart Structures and Materials (Smart Electronics and MEMS)* (V. K. Varadan, ed.), (Newport Beach, California), pp. 55–66, 1999.

[9] B. Ilic, D. Czaplewski, M. Zalalutdinov, H. G. Craighead, P. Neuzil, C. Campagnolo, and C. Batt, "Single cell detection with micromechanical oscillators," *Journal of Vacuum Science and Technology B*, vol. 19, no. 6, pp. 2825–2828, 2001.

[10] B. Ilic, Y. Yang, and H. G. Craighead, "Virus detection using nanoelectromechanical devices," *Applied Physics Letters*, vol. 85, no. 13, pp. 2604–2606, 2004.

[11] H. P. Lang, M. Hegner, and C. Gerber, "Cantilever array sensors," *Materials Today*, vol. 8, no. 4, pp. 30–36, 2005.

[12] H. P. Lang, R. Berger, F. Battiston, J.-P. Ramseyer, E. Meyer, C. Andreoli, J. Brugger, P. Vettiger, M. Despont, T. Mezzacasa, L. Scandella, H.-J. Guntherodt, C. Gerber, and J. K. Gimzewski, "A chemical sensor based on a micromechanical cantilever array for the identification of gases and vapors," *Applied Physics A: Material Science & Processing*, vol. 66, supplement 1, pp. S61–S64, 1998.

[13] N. V. Lavrik, M. J. Sepaniak, and P. G. Datskos, "Cantilever transducers as a platform for chemical and biological sensors," *Review of Scientific Instruments*, vol. 75, no. 7, pp. 2229–2253, 2004.

[14] N. Nugaeva, K. Y. Gfeller, N. Backmann, H. P. Lang, M. Duggelin, and M. Hegner, "Micromechanical cantilever array sensors for selective fungal immobilization and fast growth detection," *Biosensors and Bioelectronics*, vol. 21, no. 6, pp. 849–856, 2005.

[15] R. Raiteri, M. Grattarola, H.-J. Butt, and P. Skladal, "Micromechanical cantilever-based biosensors," *Sensors and Actuators B: Chemical*, vol. 79, no. 2-3, pp. 115–126, 2001.

[16] X. Su, C. Dai, J. Zhang, and S. J. O'Shea, "Quartz tuning fork biosensor," *Biosensors and Bioelectronics*, vol. 17, no. 1-2, pp. 111–117, 2002.

[17] T. Thundat, P. I. Oden, and R. J. Warmack, "Microcantilever sensors," *Microscale Thermophysical Engineering*, vol. 1, no. 3, pp. 185–199, 1997.

[18] I. Voiculescu, M. E. Zaghloul, R. A. McGill, E. J. Houser, and G. K. Fedder, "Electrostatically actuated resonant microcantilever beam in CMOS technology for the detection of chemical weapons," *IEEE Sensors Journal*, vol. 5, no. 4, pp. 641–647, 2005.

[19] W. Zhang and K. Turner, "Parametrically resonant mass sensor," in *Proceedings of Hilton Head 2004: The 2004 Workshop on Solid-State Sensors and Actuators*, (Hilton Head, South Carolina), pp. 49–52, 2004.

[20] C. Ziegler, "Cantilever-based biosensors," *Analytical and Bioanalytical Chemistry*, vol. 379, no. 7-8, pp. 946–959, 2004.

[21] A. Zribi, A. Knobloch, W.-C. Tian, and S. Goodwin, "Micromachined resonant multiple gas sensor," *Sensors and Actuators A: Physical*, vol. 122, no. 1, pp. 31–38, 2005.

[22] T. P. Burg, M. Godin, S. M. Knudsen, W. Shen, G. Carlson, J. S. Foster, K. Babcock, and S. R. Manalis, "Weighing of biomolecules, single cells and single nanoparticles in fluid," *Nature*, vol. 446, no. 7139, pp. 1066–1069, 2007.

[23] T. P. Burg and S. R. Manalis, "Suspended microchannel resonators for biomolecular detection," *Applied Physics Letters*, vol. 83, no. 13, pp. 2698–2700, 2003.

[24] T. P. Burg, A. R. Mirza, N. Milovich, C. H. Tsau, G. A. Popescu, J. S. Foster, and S. R. Manalis, "Vacuum-packaged suspended microchannel resonant mass sensor for biomolecular detection," *Journal of Microelectromechanical Systems*, vol. 15, no. 6, pp. 1466–1476, 2006.

[25] K. Y. Gfeller, N. Nugaeva, and M. Hegner, "Micromechanical oscillators as rapid biosensor for the detection of active growth of Escherichia Coli," *Biosensors and Bioelectronics*, vol. 21, no. 3, pp. 528–533, 2005.

[26] A. Gupta, D. Akin, and R. Bashir, "Single virus particle mass detection using microresonators with nanoscale thickness," *Applied Physics Letters*, vol. 84, no. 11, pp. 1976–1978, 2004.

[27] A. Gupta, D. Akin, and R. Bashir, "Detection of bacterial cells and antibodies using surface miromachined thin silicon cantilever resonators," *Journal of Vacuum Science and Technology B*, vol. 22, no. 6, pp. 2785–2791, 2004.

[28] B. Ilic, H. G. Craighead, S. Krylov, W. Senaratne, C. Ober, and P. Neuzil, "Attogram detection using nanoelectromechanical oscillators," *Journal of Applied Physics*, vol. 95, no. 7, pp. 3694–3703, 2004.

[29] K. M. Klein, G. T. Ostrowicki, A. Gewirtz, and S. K. Sitaraman, "Micro and nano thin film devices as bio-assays for cancer diagnosis," in *Proceedings of IMECE 2006: The 2006 ASME International Mechanical Engineering Conference and Exposition*, (Chicago, Illinois), 2006.

[30] M. Maute, S. Raible, F. E. Prins, D. P. Kern, H. Ulmer, U. Weimar, and W. Gopel, "Detection of volatile organic compounds (VOCS) with polymer-coated cantilevers," *Sensors and Actuators B: Chemical*, vol. 58, no. 1-3, pp. 505–511, 1999.

[31] T. Ono, X. Li, H. Miyashita, and M. Esashi, "Mass sensing of adsorbed molecules in sub-picogram sample with ultrathin silicon resonator," *Review of Scientific Instruments*, vol. 74, no. 3, pp. 1240–1243, 2003.

[32] L. A. Pinnaduwage, D. L. Hedden, A. Gehl, V. I. Boiadjiev, J. E. Hawk, E. J. Houser, S. Stepnowski, R. A. McGill, L. Deel, and R. T. Lareau, "A sensitive, handheld vapor sensor based on microcantilevers," *Review of Scientific Instruments*, vol. 75, no. 11, pp. 4554–4557, 2004.

[33] F. Ayazi and K. Najafi, "A HARPSS polysilicon vibrating ring gyroscope," *Journal of Microelectromechanical Systems*, vol. 10, no. 2, pp. 169–179, 2001.

[34] V. Bhadbhade and N. Jalili, "Coupled flexural/torsional vibrations of a piezoelectrically-actuated vibrating beam gyroscope," in *Proceedings of IMECE 2006: The 2006 ASME International Mechanical Engineering Congress and Exposition*, (Chicago, Illinois), 2006.

[35] L. A. Oropeza-Ramos and K. L. Turner, "Parametric resonance amplification in a MEMgyroscope," in *Proceedings of IEEE Sensors 2005: The Fourth IEEE Conference on Sensors*, (Irvine, California), 2005.

[36] A. M. Shkel, R. Horowitz, A. Seshia, and R. T. Howe, "Dynamics and control of micromachined gyroscopes," in *Proceedings of the American Control Conference*, (San Diego, California), 1999.

[37] F. Wang, L. Hobbs, and M. Smith, "A silicon gyroscope with electronic frequency tuning," in *Proceedings of IMECE 2006: The 2006 ASME International Mechanical Engineering Congress and Exposition*, (Chicago, Illinois), 2006.

[38] S. Beeby, G. Ensell, M. Kraft, and N. White, *MEMS Mechanical Sensors*. Microelectromechanical Systems (MEMS) Series, Boston: Artech House, 2004.

[39] M. Elwenspoek and R. Wiegerink, *Mechanical Microsensors*. Microtechnology and MEMS, Berlin: Springer, 2001.

[40] G. Binnig, C. F. Quate, and C. Gerber, "Atomic force microscope," *Physical Review Letters*, vol. 56, no. 9, pp. 930–933, 1986.

[41] O. Sahin, G. Yaralioglu, R. Grow, S. F. Zappe, A. Atalar, C. Quate, and O. Solgaard, "High-resolution imaging of elastic properties using harmonic cantilevers," *Sensors and Actuators A: Physical*, vol. 114, no. 2-3, pp. 183–190, 2004.

[42] S. I. Lee, S. W. Howell, A. Raman, and R. Reifenberger, "Nonlinear dynamics of microcantilevers in tapping mode atomic force microscopy: A comparison

between theory and experiment," *Physics Review B*, vol. 66, no. 11, 115409, 2002.

[43] D. Sarid, *Exploring Scanning Probe Microscopy with Mathematica*. Wiley-Interscience, 1997.

[44] W. C. Tang, T.-C. H. Nguyen, and R. T. Howe, "Laterally driven polysilicon resonant microstructures," *Sensors and Actuators*, vol. 20, no. 1-2, pp. 25–32, 1989.

[45] W. C. Tang, T.-C. H. Nguyen, M. W. Judy, and R. T. Howe, "Electrostatic-comb drive of lateral polysilicon resonators," in *Proceedings of Transducers '89: The 5th International Conference on Solid-State Sensors and Actuators and Eurosensors III*, vol. 2, pp. 328–331, 1990.

[46] R. T. Howe and R. S. Muller, "Resonant-microbridge vapor sensor," *IEEE Transactions on Electron Devices*, vol. ED-33, no. 4, pp. 499–506, 1986.

[47] M. A. Schmidt and R. T. Howe, "Silicon resonant microsensors," *Ceramic Engineering and Science Proceedings*, vol. 8, no. 9-10, pp. 1019–1034, 1987.

[48] G. Stemme, "Resonant silicon sensors," *Journal of Micromechanics and Microengineering*, vol. 1, no. 2, pp. 113–125, 1991.

[49] H. J. De Los Santos, *Introduction to Microwave Microelectromechanical Systems*. New York: Artech House, 1999.

[50] D. L. DeVoe, "Piezoelectric thin film miocromechanical beam resonators," *Sensors and Actuators A: Physical*, vol. 88, pp. 263–272, 2001.

[51] S. Basak, A. Raman, and S. V. Garimella, "Dynamic response optimization of piezoelectrically excited thin resonant beams," *Journal of Vibration and Acoustics*, vol. 127, no. 1, pp. 18–27, 2005.

[52] C. R. Tellier and T. G. Leblois, "On the design of GaAs (HHL) resonant cantilevers: Study of piezoelectric excitation, of piezoresistive sensing, and of micromachined structures," *Sensors and Actuators A: Physical*, vol. 132, no. 1, pp. 224–235, 2006.

[53] A. N. Cleland and M. L. Roukes, "Fabrication of high frequency nanometer scale mechanical resonators from bulk Si crystals," *Applied Physics Letters*, vol. 69, no. 18, pp. 2653–2655, 1996.

[54] T. Kemp and M. Ward, "Tunable response nano-mechanical beam resonator," *Sensors and Actuators A: Physical*, vol. 123-124, pp. 281–284, 2005.

[55] I. Bargatin, I. Kozinsky, and M. L. Roukes, "Efficient electrothermal actuation of multiple modes of high-frequency nanoelectromechanical resonators," *Applied Physics Letters*, vol. 90, 093116, 2007.

[56] H. Jianqiang, Z. Changchun, L. Junhua, and H. Yongning, "Depedence of the resonance frequency of thermally excited microcantilever resonators on temperature," *Sensors and Actuators A: Physical*, vol. 101, no. 1-2, pp. 37–41, 2002.

[57] A. R. Kadam, G. P. Nordin, and M. A. George, "Use of thermally induced higher order modes of a microcantilever for mercury vapor detection," *Journal of Applied Physics*, vol. 99, 094905, 2006.

[58] B. Ilic, S. Krylov, K. Aubin, R. Reichenbach, and H. G. Craighead, "Optical excitation of nanoelectromechanical oscillators," *Applied Physics Letters*, vol. 86, 193114, 2005.

[59] T. S. J. Lammerink, M. Elwenspoek, and J. H. J. Fluitman, "Optical excitation of micro-mechanical resonators," in *Proceedings of MEMS '91: IEEE Micro Electro Mechanical Systems, An Investigation of Micro Structures, Sensors, Actuators, Machines, and Robots*, (Nara, Japan), pp. 160–165, 1991.

[60] S. D. Senturia, *Microsystem Design*. Kluwer Academic Publishers, 2000.

[61] C. Liu, *Foundations of MEMS*. Illinois ECE Series, Upper Saddle River: Pearson/Prentice Hall, 2006.

[62] T. Ono and M. Esashi, "Magnetic force and optical force sensing with ultrathin silicon resonator," *Review of Scientific Instruments*, vol. 74, no. 12, pp. 5141–5146, 2003.

[63] A. C. Stephan, T. Gaulden, A.-D. Brown, M. Smith, L. F. Miller, and T. Thundat, "Microcantilever charged-particle flux detector," *Review of Scientific Instruments*, vol. 73, no. 1, pp. 36–41, 2002.

[64] A. N. Cleland, M. Pophristic, and I. Ferguson, "Single-crystal aluminum nitride nanomechanical resonators," *Applied Physics Letters*, vol. 79, no. 13, pp. 2070–2072, 2001.

[65] H. B. Peng, C. W. Chang, S. Aloni, T. D. Yuzvinsky, and A. Zettl, "Ultrahigh frequency nanotube resonators," *Physical Review Letters*, vol. 97, no. 8, 087203, 2006.

[66] L. Sekaric, J. M. Parpia, H. G. Craighead, T. Feygelson, B. H. Houston, and J. E. Butler, "Nanomechanical resonant structures in nanocrystalline diamond," *Applied Physics Letters*, vol. 81, no. 23, pp. 4455–4457, 2002.

[67] C. T.-C. Nguyen and R. T. Howe, "CMOS micromechanical resonator oscillator," in *Proceedings of the IEEE International Electron Devices Meeting*, (Washington, D. C.), pp. 199–202, 1993.

[68] M. I. Younis and A. H. Nayfeh, "A study of the nonlinear response of a resonant microbeam to an electric actuation," *Nonlinear Dynamics*, vol. 31, no. 1, pp. 91–117, 2003.

[69] E. M. Abdel-Rahman and A. H. Nayfeh, "Secondary resonances of electrically actuated resonant microsensors," *Journal of Micromechanics and Microengineering*, vol. 13, no. 3, pp. 491–501, 2003.

[70] I. Kozinsky, H. W. C. Postma, I. Bargatin, and M. L. Roukes, "Tuning nonlinearity, dynamic range, and frequency of nanomechanical resonators," *Applied Physics Letters*, vol. 88, 253101, 2006.

[71] R. Legtenberg and H. A. C. Tilmans, "Electrostatically driven vaccum-encapsulated polysilicon resonators, Part I: Design and fabrication," *Sensors and Actuators A: Physical*, vol. 45, no. 1, pp. 57–66, 1994.

[72] R. Legtenberg and H. A. C. Tilmans, "Electrostatically driven vacuum-encapsulated polysilicon resonators, Part II: Theory and performance," *Sensors and Actuators A: Physical*, vol. 45, no. 1, pp. 67–84, 1994.

[73] J. D. Zook, D. W. Burns, H. Guckel, J. J. Sniegowski, R. L. Engelstad, and Z. Feng, "Characteristics of polysilicon resonant microbeams," *Sensors and Actuators A: Physical*, vol. 35, no. 1, pp. 51–59, 1992.

[74] S. K. De and N. R. Aluru, "Complex oscillations and chaos in electrostatic microelectromechanical systems under superharmonic excitations," *Physical Review Letters*, vol. 94, 204101, 2005.

[75] V. Kaajakari, T. Mattila, A. Oja, and H. Seppa, "Nonlinear limits for single-crystal silicon microresonators," *Journal of Microelectromechanical Systems*, vol. 13, no. 5, pp. 715–724, 2004.

[76] H. Li, S. Preidikman, B. Balachandran, and C. D. Mote Jr., "Nonlinear free and forced oscillations of piezoelectric microresonators," *Journal of Micromechanics and Microengineering*, vol. 16, no. 2, pp. 356–367, 2006.

[77] S. Zaitsev, R. Almog, O. Shtempluck, and E. Buks, "Nonlinear dynamics in nanomechanical oscillators," in *Proceedings of ICMENS'05: The 2005 International Conference on MEMS, NANO, and Smart Systems*, (Banff, Alberta, Canada), pp. 387–391, 2005.

[78] H. W. C. Postma, I. Kozinsky, A. Husain, and M. L. Roukes, "Dynamic range of nanotube- and nanowire-based electromechanical systems," *Applied Physics Letters*, vol. 86, 223105, 2005.

[79] F. D. Bannon III, J. R. Clark, and C. T.-C. Nguyen, "High-Q HF microelectromechanical filters," *IEEE Journal of Solid-State Circuits*, vol. 35, no. 4, pp. 512–526, 2000.

[80] C. T.-C. Nguyen, "High-Q microelectromechanical oscillators and filters for communications," in *Proceedings of the 1997 IEEE International Symposium on Circuits and Systems*, (Hong Kong), pp. 2825–2828, 1997.

[81] C. T.-C. Nguyen, "Micromechanical resonators for oscillators and filters," in *Proceedings of the 1995 IEEE International Ultrasonics Symposium*, (Seattle, Washington), pp. 489–499, 1995.

[82] K. Wang and C. T.-C. Nguyen, "High-order medium frequency micromechanical electronic filters," *Journal of Microelectromechanical Systems*, vol. 8, no. 4, pp. 534–557, 1999.

[83] D. S. Greywall and P. A. Busch, "Coupled micromechanical drumhead resonators with practical application as electromechanical bandpass filters," *Journal of Micromechanics and Microengineering*, vol. 12, no. 6, pp. 925–938, 2002.

[84] S. Pourkamali, R. Abdolvand, G. K. Ho, and F. Ayazi, "Electrostatically coupled micromechanical beam filters," in *Proceedings of MEMS 2004: The 17th IEEE International Conference on Micro Electro Mechanical Systems*, (Maastricht, The Netherlands), pp. 584–587, 2004.

[85] S. Pourkamali and F. Ayazi, "Electrically coupled MEMS bandpass filters, Part I: With coupling elements," *Sensors and Actuators A: Physical*, vol. 122, no. 2, pp. 307–316, 2005.

[86] S. Pourkamali and F. Ayazi, "Electrically coupled MEMS bandpass filters, Part II: Without coupling elements," *Sensors and Actuators A: Physical*, vol. 122, no. 2, pp. 317–325, 2005.

[87] M. Napoli, W. Zhang, K. Turner, and B. Bamieh, "Characterization of electrostatically coupled microcantilevers," *Journal of Microelectromechanical Systems*, vol. 14, no. 2, pp. 295–304, 2005.

[88] M. Sato, B. E. Hubbard, L. Q. English, A. J. Sievers, B. Ilic, D. A. Czaplewski, and H. G. Craighead, "Study of intrinsic localized vibrational modes in micromechanical oscillator arrays," *Chaos*, vol. 13, no. 2, pp. 702–715, 2003.

[89] M. Sato, B. E. Hubbard, and A. J. Sievers, "Nonlinear energy localization and its manipulation in micromechanical oscillator arrays," *Reviews of Modern Physics*, vol. 78, no. 1, pp. 137–157, 2006.

[90] M. Sato, B. E. Hubbard, A. J. Sievers, B. Ilic, and H. G. Craighead, "Optical manipulation of intrinsic localized vibrational energy in cantilever arrays," *Europhysics Letters*, vol. 66, no. 3, pp. 318–323, 2004.

[91] M. Sato, B. E. Hubbard, A. J. Sievers, B. Ilic, D. A. Czaplewski, and H. G. Craighead, "Observation of locked intrinsic localized vibrational modes in a micromechanical oscillator array," *Physical Review Letters*, vol. 90, no. 4, 044102, 2003.

[92] J. A. Judge, B. H. Houston, D. M. Photiadis, and P. C. Herdic, "Effects of disorder in one- and two-dimensional micromechanical resonator arrays for filtering," *Journal of Sound and Vibration*, vol. 290, no. 3-5, pp. 1119–1140, 2005.

[93] J. A. Judge, J. F. Vignola, B. H. Houston, D. M. Photiadis, and M. H. Marcus, "Vibration localization in near-periodic coupled two-dimensional resonator arrays," in *Proceedings of IDECT/CIE 2005: The ASME 2005 International Design Engineering Technical Conferences & Computers and Information in Engineering Conference*, (Long Beach, California), 2005.

[94] A. J. Dick, B. Balachandran, and C. D. Mote Jr., "Nonlinear vibration modes in micro-resonator arrays," in *Proceedings of SPIE: Smart Structures and Materials 2006 (Modeling, Signal Processing, and Control)* (D. K. Lindner, ed.), vol. 6166, (San Diego, California), 2006.

[95] P. Maniadis and S. Flach, "Mechanism of discrete breather excitation in driven micro-mechanical cantilever arrays," *Europhysics Letters*, vol. 74, no. 3, pp. 452–458, 2006.

[96] M. K. Zalalutdinov, J. W. Baldwin, M. H. Marcus, R. B. Reichenbach, J. M. Parpia, and B. H. Houston, "Two-dimensional array of coupled nanomechanical resonators," *Applied Physics Letters*, vol. 88, 143504, 2006.

[97] M. Spletzer, A. Raman, R. Reifenberger, A. Q. Wu, and X. Xu, "Biochemical mass detection using mode localization in microcantilever arrays," in *Proceedings of IMECE 2005: The 2005 ASME International Mechanical Engineering Congress and Exposition*, (Orlando, Florida), 2005.

[98] M. Spletzer, A. Raman, A. Q. Wu, X. Xu, and R. Reifenberger, "Ultrasensitive mass sensing using mode localization in coupled microcantilevers," *Applied Physics Letters*, vol. 88, 254102, 2006.

[99] M. C. Cross, J. L. Rogers, R. Lifshitz, and A. Zumdieck, "Synchronization by reactive coupling and nonlinear frequency pulling," *Physical Review E*, vol. 73, 036205, 2006.

[100] M. C. Cross, A. Zumdieck, R. Lifshitz, and J. L. Rogers, "Synchronization by nonlinear frequency pulling," *Physical Review Letters*, vol. 93, 224101, 2004.

[101] F. C. Hoppensteadt and E. M. Izhikevich, "Synchronization of MEMS resonators and mechanical neurocomputing," *IEEE Transactions on Circuits and Systems I: Fundamental Theory and Applications*, vol. 48, no. 2, pp. 133–138, 2001.

[102] K. L. Turner, S. A. Miller, P. G. Hartwell, N. C. MacDonald, S. H. Strogatz, and S. G. Adams, "Five parametric resonances in a microelectromechanical system," *Nature*, vol. 396, no. 6707, pp. 149–152, 1998.

[103] R. Baskaran and K. L. Turner, "Mechanical domain coupled mode parametric resonance and amplification in a torsional mode micro electro mechanical oscillator," *Journal of Micromechanics and Microengineering*, vol. 13, no. 5, pp. 701–707, 2003.

[104] M. Napoli, R. Baskaran, K. Turner, and B. Bamieh, "Understanding mechanical domain parametric resonance in microcantilevers," in *Proceedings of MEMS 2003: The IEEE 16th Annual International Conference on Micro Electro Mechanical Systems*, (Kyoto, Japan), pp. 169–172, 2003.

[105] J. F. Rhoads, S. W. Shaw, and K. L. Turner, "The nonlinear response of resonant microbeam systems with purely-parametric electrostatic actuation," *Journal of Micromechanics and Microengineering*, vol. 16, no. 5, pp. 890–899, 2006.

[106] J. F. Rhoads, S. W. Shaw, K. L. Turner, and R. Baskaran, "Tunable microelectromechanical filters that exploit parametric resonance," *Journal of Vibration and Acoustics*, vol. 127, no. 5, pp. 423–430, 2005.

[107] J. F. Rhoads, S. W. Shaw, K. L. Turner, J. Moehlis, B. E. DeMartini, and W. Zhang, "Generalized parametric resonance in electrostatically actuated microelectromechanical oscillators," *Journal of Sound and Vibration*, vol. 296, no. 4-5, pp. 797–829, 2006.

[108] W. Zhang, R. Baskaran, and K. L. Turner, "Tuning the dynamic behavior of parametric resonance in a micromechanical oscillator," *Applied Physics Letters*, vol. 82, no. 1, pp. 130–132, 2003.

[109] W. Zhang, R. Baskaran, and K. L. Turner, "Effect of cubic nonlinearity on auto-parametrically amplified resonant MEMS mass sensor," *Sensors and Actuators A: Physical*, vol. 102, no. 1-2, pp. 139–150, 2002.

[110] W. Zhang and G. Meng, "Nonlinear dynamical system of micro-cantilever under combined parametric and forcing excitations in MEMS," *Sensors and Actuators A: Physical*, vol. 119, no. 2, pp. 291–299, 2005.

[111] W. Zhang and K. L. Turner, "Application of parametric resonance amplification in a single-crystal silicon micro-oscillator based mass sensor," *Sensors and Actuators A: Physical*, vol. 122, no. 1, pp. 23–30, 2005.

[112] W. Zhang and K. L. Turner, "Frequency-tuning for control of parametrically resonant mass sensors," *Journal of Vacuum Science and Technology A*, vol. 23, no. 4, pp. 841–845, 2005.

[113] C. Ataman, O. Kaya, and H. Urey, "Analysis of parametric resonances in comb-driven microscanners," *Proceedings of SPIE: MEMS, MOEMS, and Micromachining*, vol. 5455, pp. 128–136, 2004.

[114] C. Ataman and H. Urey, "Modeling and characterization of comb-actuated resonant microscanners," *Journal of Micromechanics and Microengineering*, vol. 16, no. 1, pp. 9–16, 2006.

[115] B. J. Gallacher, J. S. Burdess, and K. M. Harish, "A control scheme for a MEMS electrostatic resonant gyroscope excited using combined parametric excitation and harmonic forcing," *Journal of Micromechanics and Microengineering*, vol. 16, no. 2, pp. 320–331, 2006.

[116] B. E. DeMartini, J. F. Rhoads, K. L. Turner, S. W. Shaw, and J. Moehlis, "Linear and nonlinear tuning of parametrically excited MEMS oscillators," *Journal of Microelectromechanical Systems*, vol. 16, no. 2, pp. 310–318, 2007.

[117] E. Buks and M. L. Roukes, "Electrically tunable collective response in a coupled micromechanical array," *Journal of Microelectromechanical Systems*, vol. 11, no. 6, pp. 802–807, 2002.

[118] R. Lifshitz and M. C. Cross, "Response of parametrically driven nonlinear coupled oscillators with application to micromechanical and nanomechanical resonator arrays," *Physical Review B*, vol. 67, 134302, 2003.

[119] V. Kaajakari and A. Lal, "Parametric excitation of circular micromachined silicon disks," *Applied Physics Letters*, vol. 85, no. 17, pp. 3923–3925, 2004.

[120] V. Kaajakari and A. Lal, "Micromachined ultrasonic motor based on parametric polycrystalline silicon plate excitation," *Sensors and Actuators A: Physical*, vol. 137, no. 1, pp. 120–128, 2007.

[121] M. Moreno-Moreno, A. Raman, J. Gomez-Herrero, and R. Reifenberger, "Parametric resonance based scanning probe microscopy," *Applied Physics Letters*, vol. 88, 193108, 2006.

[122] W. Zhang and K. Turner, "Frequency dependent fluid damping of micro/nano flexural resonators: Experiment, model and analysis," *Sensors and Actuators A: Physical*, vol. 134, no. 2, pp. 594–599, 2007.

[123] A. H. Nayfeh and D. T. Mook, *Nonlinear Oscillations*. Wiley-Interscience, 1995.

[124] J. F. Rhoads, *Parametrically-Excited Microelectromechanical Oscillators with Filtering Capabilities*. M. S. Thesis, Michigan State University, 2004.

[125] J. J. Stoker, *Nonlinear Vibrations in Mechanical and Electrical Systems*. New York: John Wiley & Sons, 1950.

[126] W. W. Mumford, "Some notes on the history of parametric transducers," *Proceedings of the IRE*, vol. 48, no. 5, pp. 848–853, 1960.

[127] W. H. Louisell, *Coupled Mode and Parametric Electronics*. New York: John Wiley & Sons, 1960.

[128] D. P. Howson and R. B. Smith, *Parametric Amplifiers*. European Electrical and Electron Engineering Series, London: McGraw-Hill, 1970.

[129] D. Rugar and P. Grutter, "Mechanical parametric amplification and thermomechanical noise squeezing," *Physical Review Letters*, vol. 67, no. 6, pp. 699–702, 1991.

[130] D. W. Carr, S. Evoy, L. Sekaric, H. G. Craighead, and J. M. Parpia, "Parametric amplification in a torsional microresonator," *Applied Physics Letters*, vol. 77, no. 10, pp. 1545–1547, 2000.

[131] T. Ouisse, M. Stark, F. Rodrigues-Martins, B. Bercu, S. Huant, and J. Chevrier, "Theory of electric force microscopy in the parametric amplification regime," *Physical Review B*, vol. 71, 205404, 2005.

[132] M. Zalalutdinov, A. Olkhovets, A. Zehnder, B. Ilic, D. Czaplewski, H. G. Craighead, and J. M. Parpia, "Optically pumped parametric amplification for micromechanical oscillators," *Applied Physics Letters*, vol. 78, no. 20, pp. 3142–3144, 2001.

[133] B. J. Gallacher, J. S. Burdess, A. J. Harris, and K. M. Harish, "Active damping control in MEMS using parametric pumping," in *Proceedings of Nanotech 2005: The 2005 NSTI Nanotechnology Conference and Trade Show*, vol. 7, (Anaheim, California), pp. 383–386, 2005.

[134] J.-P. Raskin, A. R. Brown, B. T. Khuri-Yakub, and G. M. Rebeiz, "A novel parametric-effect MEMS amplifier," *Journal of Microelectromechanical Systems*, vol. 9, no. 4, pp. 528–537, 2000.

[135] A. Olkhovets, D. W. Carr, J. M. Parpia, and H. G. Craighead, "Non-degenerate nanomechanical parametric amplifier," in *Proceedings of MEMS 2001: The 14th IEEE International Conference on Micro Electro Mechanical Systems*, (Interlaken, Switzerland), pp. 298–300, 2001.

[136] A. Dana, F. Ho, and Y. Yamamoto, "Mechanical parametric amplification in piezoresistive gallium arsenide microcantilevers," *Applied Physics Letters*, vol. 72, no. 10, pp. 1152–1154, 1998.

[137] M. L. Roukes, K. L. Ekinci, Y. T. Yang, X. M. H. Huang, H. X. Tang, D. A. Harrington, J. Casey, and J. L. Artlett, "An apparatus and method for two-dimensional electron gas actuation and transduction for gas NEMS," World Patent, no. WO/2004/041998 A2, 2004.

[138] T. Ono, H. Wakamatsu, and M. Esashi, "Parametrically amplified thermal resonant sensor with pseudo-cooling effect," *Journal of Micromechanics and Microengineering*, vol. 15, no. 12, pp. 2282–2288, 2005.

[139] R. Karabalin, S. Masmanidis, R. Lifshitz, M. Cross, and M. Roukes, "Novel parametric actuation scheme in piezoelectric NEMS [Abstract]," in *Proceedings of the March Meeting of the Americal Physical Society*, (Denver, Colorado), 2007.

[140] J. F. Rhoads, K. M. Lukes, S. W. Shaw, and K. L. Turner, "Parametric amplification in electromagnetic microtransducers," In Preparation, 2007.

[141] J. F. Rhoads, N. J. Miller, S. W. Shaw, and B. F. Feeny, "Mechanical domain parametric amplification," in *Proceedings of IDETC/CIE 2007: ASME 2007 International Design Engineering Technical Conferences & Computers and Information in Engineering Conference, 6th International Conference on Multibody Systems, Nonlinear Dynamics, and Control (MSNDC)*, (Las Vegas, Nevada), 2007.

[142] T. Thundat, G. Y. Chen, R. J. Warmack, D. P. Allison, and E. A. Wachter, "Vapor detection using resonating microcantilevers," *Analytical Chemistry*, vol. 67, no. 3, pp. 519–521, 1995.

[143] U. Kher, "Beyond the sixth sense," *Time*, vol. 163, pp. 55–56, January 12, 2004.

[144] N. V. Lavrik, M. J. Sepaniak, and P. G. Datskos, "Microsensors, macrosensitivity," *SPIE's OEmagazine*, vol. 5, no. 2, pp. 22–24, 2005.

[145] M. Su, S. Li, and V. P. Dravid, "Microcantilever resonance-based DNA detection with nanoparticle probes," *Applied Physics Letters*, vol. 82, no. 20, pp. 3562–3564, 2003.

[146] F. M. Battiston, J. P. Ramseyer, H. P. Lang, M. K. Baller, C. Gerber, J. K. Gimzewski, E. Meyer, and H. J. Guntherodt, "A chemical sensor based on a microfabricated cantilever array with simultaneous resonance-frequency and bending readout," *Sensors and Actuators B: Chemical*, vol. 77, no. 1-2, pp. 122–131, 2001.

[147] Z. J. Davis, G. Abadal, O. Kuhn, O. Hansen, F. Grey, and A. Boisen, "Fabrication and characterization of nanoresonating devices for mass detection," *Journal of Vacuum Science and Technology B*, vol. 18, no. 2, pp. 612–616, 2000.

[148] K. L. Ekinci, X. M. H. Huang, and M. L. Roukes, "Ultrasensitive nanoelectromechanical mass detection," *Applied Physics Letters*, vol. 84, no. 22, pp. 4469–4471, 2004.

[149] B. Ilic, D. Czaplewski, H. G. Craighead, P. Neuzil, C. Campagnolo, and C. Batt, "Mechanical resonant immunospecific biological detector," *Applied Physics Letters*, vol. 77, no. 3, pp. 450–452, 2000.

[150] L. B. Sharos, A. Raman, S. Crittenden, and R. Reifenberger, "Enhanced mass sensing using torsional and lateral resonances in microcantilevers," *Applied Physics Letters*, vol. 84, no. 23, pp. 4638–4640, 2004.

[151] T. Thundat, E. A. Wachter, S. L. Sharp, and R. J. Warmack, "Detection of mercury vapor using resonating microcantilevers," *Applied Physics Letters*, vol. 66, no. 13, pp. 1695–1697, 1995.

[152] Y. T. Yang, C. Callegari, X. L. Feng, K. L. Ekinci, and M. L. Roukes, "Zeptogram-scale nanomechanical mass sensing," *Nano Letters*, vol. 6, no. 4, pp. 583–586, 2006.

[153] G. Y. Chen, T. Thundat, E. A. Wachter, and R. J. Warmack, "Adsorption-induced surface stress and its effects on resonance frequency of microcantilevers," *Journal of Applied Physics*, vol. 77, no. 6, pp. 3618–3622, 1995.

[154] Q. Ren and Y.-P. Zhao, "Influence of surface stress on frequency of microcantilever-based biosensors," *Microsystem Technologies*, vol. 10, no. 4, pp. 307–314, 2004.

[155] W. Zhang, R. Baskaran, and K. L. Turner, "Nonlinear dynamics analysis of a parametrically resonant MEMS sensor," in *Proceedings of the 2002 SEM Annual Conference and Exposition on Experimental and Applied Mechanics*, (Milwaukee, Wisconsin), 2002.

[156] M. V. Requa and K. L. Turner, "Precise frequency estimation in a microelectromechanical parametric resonator," *Applied Physics Letters*, vol. 90, 173508, 2007.

[157] M. V. Requa and K. L. Turner, "Electromechanically diven and sensed parametric resonance in silicon microcantilevers," *Applied Physics Letters*, vol. 88, 263508, 2006.

[158] E. M. Abdel-Rahman, M. I. Younis, and A. H. Nayfeh, "Characterization of the mechanical behavior of an electrically actuated microbeam," *Journal of Micromechanics and Microengineering*, vol. 12, no. 6, pp. 759–766, 2002.

[159] M. Napoli, B. Bamieh, and K. Turner, "A capacitive microcantilever: Modelling, validation, and estimation using current measurements," *Journal of Dynamic Systems, Measurement, and Control*, vol. 126, no. 2, pp. 319–326, 2004.

[160] M. I. Younis, E. M. Abdel-Rahman, and A. Nayfeh, "A reduced-order model for electrically actuated microbeam-based MEMS," *Journal of Microelectromechanical Systems*, vol. 12, no. 5, pp. 672–680, 2003.

[161] W. Zhang and K. L. Turner, "Noise analysis in parametric resonance based mass sensing," in *Proceedings of IMECE 2004: The ASME International Mechanical Engineering Congress and Exposition*, (Anaheim, California), 2004.

[162] D. S. Greywall, B. Yurke, P. A. Busch, and S. C. Arney, "Low-temperature anomalies in the dissipation of small mechanical resonators," *Europhysics Letters*, vol. 34, no. 1, pp. 37–42, 1996.

[163] D. S. Greywall, B. Yurke, P. A. Busch, A. N. Pargellis, and R. L. Willett, "Evading amplifier noise in nonlinear oscillators," *Physical Review Letters*, vol. 72, no. 19, pp. 2992–2995, 1994.

[164] A. N. Cleland, *Foundations of Nanomechanics: From Solid-State Theory to Device Applications*. Advanced Texts in Physics, Berlin: Springer, 2003.

[165] S. C. Jun, X. M. H. Huang, J. Hone, C. A. Zorman, and M. Mehregany, "Evaluation of 3C-SiC nanomechanical resonators using room temperature magnetomotive transduction," in *Proceedings of IEEE Sensors 2005: The 4th IEEE Conference on Sensors*, (Irvine, California), pp. 1042–1045, 2005.

[166] A. Husain, J. Hone, H. W. C. Postma, X. M. H. Huang, T. Drake, M. Barbic, A. Scherer, and M. L. Roukes, "Nanowire-based very-high-frequency electromechanical resonator," *Applied Physics Letters*, vol. 83, no. 6, pp. 1240–1242, 2003.

[167] A. N. Cleland and M. L. Roukes, "A nanometer-scale mechanical electrometer," *Nature*, vol. 392, no. 6672, pp. 160–162, 1998.

[168] S. J. Martin, M. A. Butler, J. J. Spates, M. A. Mitchell, and W. K. Schubert, "Flexural plate wave resonator excited with Lorentz forces," *Journal of Applied Physics*, vol. 83, no. 9, pp. 4589–4601, 1998.

[169] X. M. H. Huang, X. L. Feng, C. A. Zorman, M. Mehregany, and M. L. Roukes, "VHF, UHF and microwave frequency nanomechanical resonators," *New Journal of Physics*, vol. 7, no. 247, pp. 1–15, 2005.

[170] X. M. H. Huang, M. Manolidis, S. C. Jun, and J. Hone, "Nanomechanical hydrogen sensing," *Applied Physics Letters*, vol. 86, 143104, 2005.

[171] M. V. Requa, *Parametric Resonance in Microcantilevers for Applications in Mass Sensing*. Ph.D. Dissertation, University of California, Santa Barbara, 2006.

[172] B. E. DeMartini, J. F. Rhoads, S. W. Shaw, and K. L. Turner, "A resonant single input - single output mass sensor based on a coupled array of microresonators," *Sensors and Actuators A: Physical*, vol. 137, no. 1, pp. 147–156, 2007.

[173] B. E. DeMartini, J. F. Rhoads, S. W. Shaw, and K. L. Turner, "A resonant SISO sensor based on a coupled array of microelectromechanical oscillators," in *Proceedings of Hilton Head 2006: A Solid-State Sensor, Actuator, and Microsystems Workshop*, (Hilton Head, South Carolina), 2006.

[174] J. F. Rhoads, B. E. DeMartini, S. W. Shaw, and K. L. Turner, "A SISO, multi-analyte sensor based on a coupled microresonator array," in *Proceedings of IMECE 2006: The 2006 ASME International Mechanical Engineering Conference and Exposition*, (Chicago, Illinois), 2006.

[175] G. Maidanik and K. J. Becker, "Noise control of a master harmonic oscillator coupled to a set of satellite harmonic oscillators," *Journal of the Acoustical Society of America*, vol. 104, no. 5, pp. 2628–2637, 1998.

[176] K. Xu and T. Igusa, "Dynamic characteristics of multiple substructures with closely spaced frequencies," *Earthquake Engineering and Structural Dynamics*, vol. 21, no. 12, pp. 1059–1070, 1992.

[177] R. L. Weaver, "Mean and mean-square responses of a prototypical master/fuzzy structure," *Journal of the Acoustical Society of America*, vol. 101, no. 3, pp. 1441–1449, 1997.

[178] L. Meirovitch, *Elements of Vibration Analysis*. New York: McGraw-Hill, 2nd ed., 1986.

[179] C. Pierre and E. H. Dowell, "Localization of vibrations by structural irregularity," *Journal of Sound and Vibration*, vol. 114, no. 3, pp. 549–564, 1987.

[180] W. Zhang, W. Zhang, K. Turner, and P. G. Hartwell, "SCREAM'03: A single mask process for high-Q single crystal silicon MEMS," in *Proceedings of IMECE 2004: The 2004 ASME International Mechanical Engineering Congress and Exposition*, (Anaheim, California), 2004.

[181] K. L. Turner, P. G. Hartwell, and N. C. MacDonald, "Multi-dimensional MEMS motion characterization using laser vibrometry," in *Proceedings of Transducers '99 The 10th International Conference on Solid-state Sensors and Actuators*, (Sendai, Japan), pp. 1144–1147, 1999.

[182] K. L. Ekinci, Y. T. Yang, and M. L. Roukes, "Ultimate limits to inertial mass sensing based upon nanoelectromechanical systems," *Journal of Applied Physics*, vol. 95, no. 5, pp. 2682–2689, 2004.

[183] J. R. Vig and Y. Kim, "Noise in microelectromechanical system resonators," *IEEE Transactions on Ultrasonics, Ferroelectrics, and Frequency Control*, vol. 46, no. 6, pp. 1558–1565, 1999.

[184] P. Mohanty, D. A. Harrington, K. L. Ekinci, Y. T. Yang, M. J. Murphy, and M. L. Roukes, "Intrinsic dissipation in high-frequency micromechanical resonators," *Physical Review B*, vol. 66, 085416, 2002.

[185] J. Tamayo, A. D. L. Humphris, A. M. Malloy, and M. J. Miles, "Chemical sensors and biosensors in liquid environment based on microcantilevers with amplified quality factor," *Ultramicroscopy*, vol. 86, no. 1-2, pp. 167–173, 2001.

[186] H. P. Lang, R. Berger, C. Andreoli, J. Brugger, M. Despont, P. Vettiger, C. Gerber, J. P. Ramseyer, E. Meyer, and H.-J. Guntherodt, "Sequential position readout from arrays of micromechanical cantilever sensors," *Applied Physics Letters*, vol. 72, no. 3, pp. 383–385, 1998.

[187] E. H. Dowell, "Nonlinear oscillations of a fluttering plate," *AIAA Journal*, vol. 4, no. 7, pp. 1267–1275, 1966.

[188] V. V. Bolotin, *Nonconservative Problems in the Theory of Elastic Stability*. Oxford: Pergamon Press, 1963.

[189] M. Ashhab, M. V. Salapaka, M. Dahleh, and I. Mezic, "Melnikov-based dynamical analysis of microcantilevers in scanning probe microscopy," *Nonlinear Dynamics*, vol. 20, no. 3, pp. 197–220, 1999.

[190] M. Ashhab, M. V. Salapaka, M. Dahleh, and I. Mezic, "Dynamic analysis and control of microcantilevers," *Automatica*, vol. 35, no. 10, pp. 1663–1670, 1999.

[191] S. Chowdhury, M. Ahmadi, and W. C. Miller, "A closed-form model for the pull-in voltage of electrostatically actuated cantilever beams," *Journal of Micromechanics and Microengineering*, vol. 15, no. 4, pp. 756–763, 2005.

[192] S. Krylov and R. Maimon, "Pull-in dynamics of an elastic beam actuated by continuously distributed electrostatic force," *Journal of Vibration and Acoustics*, vol. 126, no. 3, pp. 332–342, 2004.

[193] S. Pamidighantam, R. Puers, K. Baert, and H. A. C. Tilmans, "Pull-in voltage analysis of electrostatically actuated beam structures with fixed-fixed and fixed-free end conditions," *Journal of Micromechanics and Microengineering*, vol. 12, no. 4, pp. 458–464, 2002.

[194] S. Krylov, I. Harari, and Y. Cohen, "Stabilization of electrostatically actuated microstructures using parametric excitation," *Journal of Micromechanics and Microengineering*, vol. 15, no. 6, pp. 1188–1204, 2005.

[195] A. H. Nayfeh and D. T. Mook, *Nonlinear Oscillations*. Wiley-Interscience, 1979.

[196] W. Zhang, F. Wang, and M. Yao, "Global bifurcations and chaotic dynamics in nonlinear nonplanar oscillations of a parametrically excited cantilever beam," *Nonlinear Dynamics*, vol. 40, no. 3, pp. 251–279, 2005.

[197] M. R. M. Crespo da Silva and C. C. Glynn, "Nonlinear flexural-flexural-torsional dynamics of inextensional beams. I: Equations of motion," *Journal of Structural Mechanics*, vol. 6, no. 4, pp. 437–448, 1978.

[198] M. R. M. Crespo da Silva and C. C. Glynn, "Nonlinear flexural-flexural-torsional dynamics of inextensional beams. II: Forced motions," *Journal of Structural Mechanics*, vol. 6, no. 4, pp. 449–461, 1978.

[199] P. Malatkar, *Nonlinear Vibrations of Cantilever Beams and Plates*. Ph.D. Dissertation, Virginia Polytechnic Institute and State University, 2003.

[200] J. D. Jackson, *Classical Electrodynamics*. New York: John Wiley & Sons, 1962.

[201] A. Matveyev, *Principles of Electrodynamics*. New York: Reinhold Publishing Company, 1966.

[202] S. H. Strogatz, *Nonlinear Dynamics and Chaos with Applications to Physics, Biology, Chemistry, and Engineering*. Cambridge: Westview, 1994.

[203] H. B. Chan and C. Stambaugh, "Activation barrier scaling and crossover for noise-induced switching in a micromechanical parametric oscillator [Preprint]," arXiv:cond-mat/0609394 v1, 2006.

[204] C. M. Caves, "Quantum limits on noise in linear amplifiers," *Physical Review D*, vol. 26, no. 8, pp. 1817–1839, 1982.